Open-circuit stability and integration of silicon electrodes for solar fuels devices

Thesis by

Harold Jin Fu

In Partial Fulfillment of the Requirements for the

Degree of

Doctor of Philosophy

CALIFORNIA INSTITUTE OF TECHNOLOGY

Pasadena, California

2022

Defended August 3, 2021

Harold J. Fu
ORCID: 0000-0001-9738-209X

ACKNOWLEDGEMENTS

Caltech has always felt familiar to me even before I arrived for orientation as a new graduate student. Throughout high school I took trips to the campus from my hometown in San Diego to see my brother as he was pursuing his degree here. Even so, getting the option to pursue a Ph.D. here was a surreal experience and I remember vividly the moment I opened an email with the subject line “caltech!”. In many ways it felt like I was coming back home after four wonderful years at Cornell.

First and foremost, I would like to thank my advisor Nate Lewis for his guidance throughout my years at Caltech. Nate is one of the smartest people that I have met and his drive to make the world a better, more sustainable place is inspiring. I have learned so much during my time in his research group. Similarly, I want to thank Bruce Brunschwig and Kimberly Papadantonakis for giving me excellent advice throughout my graduate school career and for having done so much towards bringing our group closer together.

I would also like to thank Rick Flagan, Julie Kornfield, and Mikhail Shapiro for being a part of my thesis committee. I am also grateful to Rick and Mikhail for being such great professors to be a teaching assistant for, as they made teaching transport phenomena enriching and enjoyable.

I will always be grateful for the mentors that taught me so much during my time at Caltech. I met Paul Kempler during my visit week, and ever since he has only ever given me good advice. He helped introduce me to the Lewis group, mentored me during one of my rotations, and provided me valuable thoughts and ideas about my research throughout my Ph.D. Annelise Thompson also really helped familiarize me with the Lewis Group as a mentor for my first rotation project and provided me with thoughtful feedback during my

preparation for Ph.D. candidacy. Shane Ardo helped me immensely with the initial direction of my Ph.D. He has been a constant source of enthusiasm and encouragement and I always looked forward to driving to UC Irvine in order to talk to him. Finally, I owe a lot of my success to Ivan Moreno-Hernandez. Whether it was the discussions we had during lunch, bringing me along as a mentor for SEAL, or the encouragement to pursue my work related to silicon passivation, Ivan was always there to talk to me and really helped shape the direction of the latter half of my Ph.D.

I would also like to thank all of my friends and colleagues within the Lewis Group. I want to thank Pai Buabthong for all his knowledge on XPS and for being one of the most interesting person out there. Our trip flying to Death Valley is definitely a highlight of my graduate school years. I would also like to thank Weilai Yu for always being dependable and for helping me take care of the AFMs. I want to thank Zach Ifkovits for being a great lab and office mate, whether that means solving Rubik's cubes in the office, watching soccer in the conference room, or the going to a live showing of a sitcom. I would like to thank Ellen Yan for the mock case interviews and all the helpful feedback given to me. I would like to thank Matthias Richter, Miguel Caban-Acevedo and Stefan Omelchenko for valuable help, discussions, and feedback they have given me on my research. I am also grateful to Paul Nunez for playing video games in the conference room and coming along to local tournaments after work. I want to thank my cohorts Katie Hamann, Michael Mazza, Kathleen Kennedy, and Katie Chen for being great people to work with in our first years in the group. I also want to thank the rest of my G135 officemates, including Kat Rinaldi, Jake Evans, Jackie Dowling, Carlos Read, and Michael Lichterman, for making our office the best office. Of course, I want to thank the rest of the Lewis group, including Sean Byrne,

Alex Ye, Mo Morla, Madeline Meier, Ethan Simonoff, Azhar Carim, Burt Simpson, Renata Balgley, Xinghao Zhou, Jingjing Jiang, Sisir Yalamanchili, Dan Torelli, Ke Sun, Kyra Lee, Jonathan Thompson, Fadl Saadi, Noah Plymale, and Josh Wiensch. I also want to thank Justin Bui and Amar Bhardwaj for their hard work and for making the summers so enjoyable.

From traveling the world together to staying at home during a pandemic, I want to thank Lea Chon for always being there with me. She has been an unwavering source of inspiration and support throughout all the challenges I faced in graduate school and all the successes I celebrated along the way. I will always be grateful for my parents Mingjie Jin and Xiang-Dong Fu for supporting me in every way possible. I would also like to thank Ross Fu, Annie Tigranyan, Bruce Fu, and Arthur Fu for all the times they have rooted for me throughout these years.

ABSTRACT

Two significant challenges that impede the realization of inexpensive, solar-driven water electrolysis involve the corrosion and integration of component materials. For instance, Si is a prominent light absorbing material that readily corrodes in alkaline electrolyte unless subjected to an oxidative potential. Although a protective coating can be applied to mitigate corrosion, the underlying semiconductor remains exposed to electrolyte at pinholes on the protective coating. Illumination slows the dissolution of Si photoanodes further by 2-3 orders of magnitude via oxidation to SiO_x. However, Si is still susceptible to corrosion under nighttime conditions and device stability must be maintained regardless of diurnal patterns of sunlight. This thesis explores two approaches to drive Si passivation in the dark at open circuit. First, a protective electrolyte can be introduced to solution that acts as an oxidizing agent to Si. Secondly, a catalytic thin film like NiO_x on Si can drive the electrode potential positive by catalyzing O_2 in electrolyte. Applying either passivation strategy yielded extended stability of Si photoanodes subjected to simulated day/night cycling. In addition to corrosion, device performance is critically dependent on the integration of component materials. Efficient water splitting requires that at least two semiconductors be connected in series to drive the reaction, while lateral resistance losses in electrolyte preclude large (> cm^2) planar photoelectrode areas. Si can be vertically arranged as high aspect ratio microwires that can be embedded in an ion exchange membrane. This assembly can be laminated to a tandem partner arranged in a similar configuration using an electrically conductive interlayer. This thesis additionally investigates the bulk and interfacial properties of Nafion-PEDOT:PSS composite films as a candidate material for this interlayer. After solvent treatment, the composite film

exhibited percolation of electrically conductive PEDOT domains even at dilute PEDOT concentrations (~ 0.2 wt%). Despite the presence of an insulating Nafion-rich layer on the surface, the composite forms a low resistance contact to CH_3-terminated p-Si, thereby making the composite a viable interlayer for use in a fully integrated, tandem water splitting device.

PUBLISHED CONTENT AND CONTRIBUTIONS

1. **H. J. Fu**, I. A. Moreno-Hernandez, P. Buabthong, K. M. Papadantonakis, B. S. Brunschwig, N. S. Lewis, Enhanced stability of silicon for photoelectrochemical water oxidation through self-healing enabled by an alkaline protective electrolyte, Energy & Environmental Science, 2020, 13, 4132-4141. DOI: 10.1039/D0EE02250K. Adapted for Chapter 2.

   H. J. Fu participated in the conception of the project, collected and analyzed data, and assisted in the writing and editing of the manuscript.

2. **H. J. Fu**, P. Buabthong, Z. P. Ifkovits, W. Yu, B. S. Brunschwig, N. S. Lewis, Catalytic open-circuit passivation by thin metal oxide films of p-Si anodes in aqueous alkaline electrolytes, Energy & Environmental Science, 2021, 15, 334-345. DOI: 10.1039/D1EE03040J. Adapted for Chapter 3.

   H. J. Fu participated in the conception of the project, collected and analyzed data, and assisted in the writing and editing of the manuscript.

3. P. A. Kempler, **H. J. Fu**, Z. P. Ifkovits, K. M. Papadantonakis, N. S. Lewis, Spontaneous Formation of >90% Optically Transmissive, Electrochemically Active CoP Films for Photoelectrochemical Hydrogen Evolution, The Journal of Physical Chemistry Letters, 2019, 11, 14-20. DOI: 10.1021/jpclett.9b02926.

   H. J. Fu participated in the collection of data and editing of the manuscript.

4. I. A. Moreno-Hernandez, S. Yalamanchili, **H. J. Fu**, H. A. Atwater, B. S. Brunschwig, N. S. Lewis, Conformal SnOx heterojunction coatings for stabilized photoelectrochemical water oxidation using arrays of silicon microcones, Journal of Materials Chemistry A, 2020, 8, 9292-9301. DOI: 10.1039/D0TA01144D.

H. J. Fu participated in the collection of data and editing of the manuscript.

5. W. Yu†, **H. J. Fu†**, T. Mueller, B. S. Brunschwig, N. S. Lewis, Atomic force microscopy: Emerging illuminated and operando techniques for solar fuel research, The Journal of Chemical Physics, 2020, 153, 020902. DOI: 10.1063/5.0009858.

   H. J. Fu participated in the conception of the project and assisted in the writing and editing of the manuscript. †Equal contributions.

6. P. Buabthong, J. M. Evans, K. Z. Rinaldi, K. M. Kennedy, **H. J. Fu**, Z. P. Ifkovits, T. J. Kuo, B. S. Brunschwig, N. S. Lewis, GaAs microisland anodes protected by amorphous TiO_2 films mitigate corrosion spreading during water oxidation in alkaline electrolytes, ACS Energy Letters, 2021, 6, 3709-3714. DOI: 10.1021/acsenergylett.1c01174.

   H. J. Fu participated in the collection of data and editing of the manuscript.

7. M. F. Mazza, M. Cabán-Acevedo, **H. J. Fu**, M. C. Meier, A. C. Thompson, N. S. Lewis, Selective-area, water-free atomic layer deposition of metal oxides on graphene defects, ACS Materials Au, 2022, 2, 74-78. DOI: 10.1021/acsmaterialsau.1c00049.

   H. J. Fu participated in the collection of data for the manuscript.

TABLE OF CONTENTS

LIST OF FIGURES, SCHEMES, AND TABLES

Chapter 1

INTRODUCTION

1.1 Solar Fuels as Energy Storage

The rising global mean temperature due to the increase in atmospheric CO_2 concentration necessitates a shift to net-zero carbon emission energy systems.[1] De-carbonization of the electric grid requires generation from renewable energy sources like solar radiation.[2] The supply of energy from the sun is abundant; an hour of incident sunlight on Earth is enough to power the world for a year.[3] However, electricity produced by solar photovoltaics is non-dispatchable and consequently the supply of solar energy is constrained by the intermittent nature of sunlight.[4] Energy demand is also time varying with peak demand often occurring in the evening with low solar irradiance, necessitating for grid-scale energy storage to address the temporal mismatch between renewable energy supply and demand.[5] Direct conversion of solar irradiance to chemical fuels addresses the issue of dispatchability by storing solar energy in chemical bonds, providing on-demand energy via spontaneous chemical or electrochemical reactions.[6] Combustion of carbon-based fuels can be circumvented entirely by using hydrogen fuel generated from sunlight. Photoelectrochemical water splitting using photoactive semiconductors and electrocatalysts enables conversion of sunlight and water into hydrogen and oxygen.[7-9] The product hydrogen can be stored until needed and generate electricity on-demand when recombined with oxygen in a fuel cell.

1.2 Photoelectrochemical Water Splitting

Photoelectrochemistry (PEC) is the utilization of photon energy to drive charge transfer in electrochemical systems. In regards to PEC water splitting, a generated photovoltage must exceed the 1.23 V thermodynamic requirement for the conversion of water to hydrogen (H_2(g)) and oxygen (O_2(g)).[7] The PEC device for water splitting consists of the following key components: a membrane to separate gaseous products while conducting the reactant electrolyte, catalysts to reduce kinetic barriers for water splitting, and photoactive semiconductors to absorb light and separate generated charge carriers.[10]

The electrolysis of water is composed of two half reactions: the hydrogen evolution reaction (HER) at the cathode and the oxygen evolution reaction (OER) at the anode. Resistive losses in the electrolyte can be avoided by performing water electrolysis in either a highly acidic (pH < 1) or alkaline (pH > 13) electrolyte.[11] In acidic electrolyte, protons (H^+) are generated by the OER and must be transported and reacted at the HER site. In alkaline electrolyte, hydroxide (OH^-) ions are produced by the HER and must be transported and reacted at the OER site. Maintaining a steady-state transference number of H^+ or OH^- is necessary to avoid building a concentration gradient of the corresponding ion that would consequently result in large solution resistances.[12] Additionally, the H_2(g) and O_2(g) products formed from water splitting must be separated to avoid undesirable back-reactions both as a safety measure and to maintain product yield. Separating the cathode and anode with an ion exchange membrane fulfills product separation while preventing polarization losses.[13]

Catalysts at the cathode and anode increase reaction rates by reducing the kinetic overpotentials for the HER and OER, respectively. Both catalytic activity and stability

against corrosion are key performance metrics. In commercial electrolyzers, noble metal catalysts like Pt and IrO_x are used to drive the HER and OER, respectively, due to their high activity and stability.[14] However, noble metal catalysts are rare and subsequently are cost prohibitive when considering scaling the production of electrolyzers for grid-scale hydrogen generation. Earth abundant alternatives to Pt like CoP have been demonstrated with comparable activity for the HER while possessing > 1000 h stability under continuous operation in acidic electrolyte.[15] However, CoP is susceptible to corrosion under open-circuit conditions, precluding its use in PEC applications under diurnal patterns of sunlight.[16] For the OER in acidic electrolytes, $MnSbO_x$ exhibits stable activity but its overpotential is > 300 mV higher than state-of-the-art catalysts.[17] Conversely, operating in alkaline electrolyte is desirable due to the availability of stable, active, and earth abundant catalysts. NiMo and NiFeOOH have been shown to exhibit > 100 h stability in alkaline electrolyte and exhibit < 100 mV and ~ 350 mV overpotentials for the HER and OER,[9, 18, 19] respectively.

The underlying principle for charge carrier generation and separation in semiconductor-based PEC devices is similar to that of in photovoltaics. Incident photons can excite an electron across the semiconductor band gap, promoting the electron to the conduction band gap and leaving a positive charge hole behind at the valence band.[20] Photoactivity requires a rectifying junction at a semiconductor interface in order to separate photogenerated electron-hole pairs at the built-in electric field. The rectifying junction is formed at the semiconductor interface with either a metal, the electrolyte, or another semiconductor and results from the equilibrium of the different electrochemical potentials.[7] Minority carriers that move across the junction generate a photovoltage and are collected

either as current in photovoltaic cells or participate in charge-transfer reactions in PEC cells.

In order to drive PEC water splitting at an appreciable current density (> 10 mA cm^{-2}) without external assistance, the generated photovoltage must account for 1.23 V associated with the thermodynamic potential for water splitting, ~ 0.4 V kinetic overpotentials for the HER and OER, and ~ 0.1 V for ion or electron transport losses.[21] Since photovoltage is constrained by the band gap and carrier recombination of the photoactive semiconductor, unassisted water splitting can only occur either with a large band gap (~ 3 eV) semiconductor or with a tandem cell consisting of two or more semiconductors connected in series.[22, 23] $SrTiO_3$ (3.2 eV band gap) is one example of a semiconductor that can drive unassisted water splitting due to its large band gap and favorable band edge positions for water splitting.[7, 24] However, the large band gap precludes efficient utilization of the solar spectrum due to its inability to absorb visible or near infrared light. Conversely, small band gap (< 2 eV) semiconductors are capable of absorbing more of the solar spectrum but as single light absorbers do not meet the requisite photovoltage (~ 1.7 eV) to efficiently split water.[25] Advancements in the semiconductor processing industry has made monocrystalline Si (1.1 eV band gap) both efficient and cost-effective for use as a photoactive material.[26] Si has subsequently been studied extensively as a photocathode or photoanode for assisted water splitting.[27] Pairing a small band gap semiconductor like Si with a large band gap semiconductor in series not only can meet the photovoltage threshold for unassisted water splitting, but can also optimize light absorption between the photoelectrodes by minimizing thermalization losses at the expense of

increased device complexity. The optimal pairing with Si has a band gap of ~ 1.8 eV and correspondingly produces a maximum theoretical solar-to-hydrogen efficiency of > 25%.[28]

1.3 Semiconductor Corrosion and Mitigation

The corrosion of catalysts and semiconductors is a major trade-off for avoiding the polarization losses associated with operating in highly acidic or alkaline electrolytes. In acidic electrolytes, semiconductors like Si and InP exhibit stable performance due to the formation of a passivating surficial oxide.[29, 30] In alkaline electrolytes, NiMo and NiFeOOH present highly active, stable, and earth abundant catalysts that can operate for > 100 h.[18] Unlike in acidic electrolyte, Si does not form a passivating oxide at open circuit in alkaline electrolyte, leading to dissolution as $H_2SiO_4^{2-}$ ions.[31] While Si photoanodes can mitigate rapid corrosion by oxidizing its surface during operation using photogenerated holes, Si photocathodes lack an oxidative pathway towards surface passivation.[32] Although SiO_x etch rate is orders of magnitude lower than that of Si in alkaline electrolyte,[33, 34] SiO_x dissolution leads to gradual corrosion and necessitates continual oxide formation.

Stabilized photoelectrodes in alkaline electrolytes have been realized by employing protection strategies to mitigate semiconductor corrosion in conjunction with active, alkaline-stable earth abundant catalysts.[35] Protection layers function as a physical barrier that prevents the electrolyte from corroding the underlying semiconductor. The layer must be sufficiently optically transmissive to avoid parasitic absorption and electrically conductive to allow charge to move from semiconductor to catalyst or electrolyte. One of the most prominent protection layer materials is TiO_2 for its corrosion resistance and transparency to visible light.[35] For a photoanode protected by amorphous TiO_2,[36] holes

conduct through defect states in between the valence and conduction bands, allowing for charge to transfer at a potential near that of the OER.[37] This protection layer has been demonstrated on a variety of semiconductors in alkaline electrolytes, including Si, GaAs, GaP, CdTe, and $BiVO_4$.[36, 38, 39] Atomic layer deposition of amorphous TiO_2 furthermore enables conformal coatings on high aspect ratio structures like Si microwire arrays.[40] The protection layer can have additional functionalities such as acting as a catalyst layer or creating band bending to form a heterojunction with the semiconductor.[41, 42] For instance, in addition to being transparent and hole-conductive, NiO_x and CoO_x protective coatings are catalytically active and the latter forms a heterojunction with Si generating 570 mV of photovoltage.[43, 44]

Protected photoelectrodes remain susceptible to corrosion at physical defects in the protection layer like pinholes.[32] Over time, photoelectrode failure is accelerated by the undercutting of the protection layers at pinholes because more of the underlying semiconductor becomes exposed to the electrolyte.[45] The scale-up of photoelectrodes for commercial use is consequently impeded by the presence of pinholes. For instance, an amorphous TiO_2-protected III-V semiconductor tandem exhibited stability for > 40 h but was constrained to mm^2-scale electrode areas in order to avoid pinholes formed during TiO_2 deposition.[46] For protected Si photoanodes in alkaline electrolyte actively forming O_2(g), rapid corrosion at pinholes is suppressed by surface oxidation using photogenerated holes (Scheme 1.1a).[30] However, without any energetic inputs during dark, open-circuit conditions, the Si photoanode does not actively form a passivating oxide and remains susceptible to corrosion (Scheme 1.1b).[47] Mitigating Si corrosion in the dark is as important as it is in light because device stability must be maintained regardless of the diurnal

variations of solar insolation. Chapters 2 and 3 of this thesis explore methods to mitigate Si corrosion at open-circuit by passively driving Si oxidation using either a protective electrolyte or catalytic thin films like Ni and NiO_x.

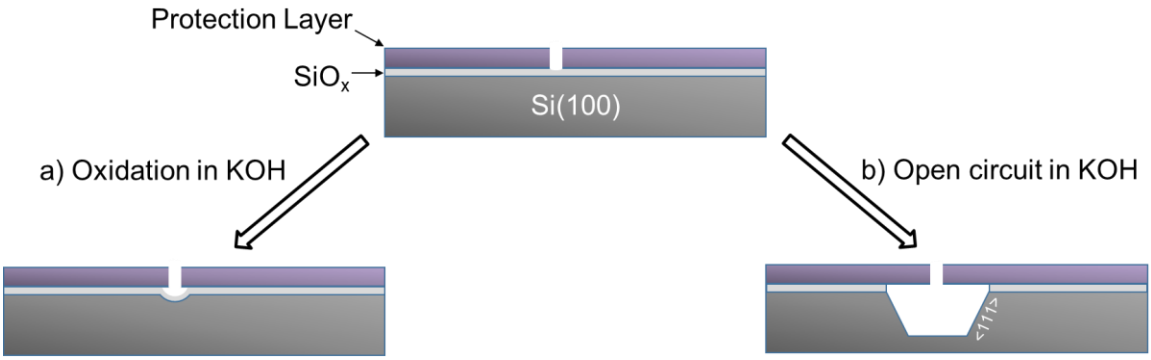

Scheme 1.1. Corrosion behavior of protected Si(100) electrodes at a pinhole in strongly alkaline electrolyte. (a) Passivation of Si via oxidation to SiO_x. SiO_x etches isotropically in KOH and corrodes slowly compared to Si. Illumination, applied positive potential, protective electrolytes, and catalytic thin films can be used to oxidize Si. (b) Corrosion of Si at open circuit. Si(100) etches anisotropically in KOH, exposing the slower etching <111> facet.

1.4 Considerations for Photoelectrode Integration

Steady state operation of a photoelectrode requires the interplay between light absorption, charge separation, electron transport, electrochemistry, and ion transport. Consequently, performance loss in any one of these aspects leads to a bottleneck in overall device efficiency. Minimizing performance trade-offs when integrating light absorbers with catalysts, protective layers, membranes, or other light absorbers remains an active area of research within the solar fuels field.[2, 37, 48, 49] For instance, catalysts can benefit from higher loadings due to increased active surface area at the expense of increased opacity and material costs.[50] Parasitic light absorption of opaque catalysts limit photocurrents generated by the light absorber, requiring either a transparent back contact with back-facing illumination or mitigation of opacity with front-facing illumination. Some strategies to

mitigate opacity include using ultrathin (< 5 nm) catalyst films or depositing thick catalyst islands.[51, 52] Such islands can be electrodeposited as discrete nanoparticles, patterned with photolithography, or formed spontaneously via selective wet etching.[30, 53, 54]

Realizing a fully integrated PEC device at scale requires consideration of membrane placement in order to minimize ion transport length and its associated losses. Calculations have shown that the lateral dimensions of a planar electrode cannot greatly exceed that of the membrane without avoiding significant resistive losses associated with ion transport, consequently constraining the scale-up of planar PEC devices.[21] An alternative device architecture involves the use of high aspect ratio micro- or nanostructured semiconductor arrays embedded in an ion exchange membrane (Scheme 1.2).[49, 55] The membrane scaffold provides both mechanical support and minimal ion transport losses between catalytic sites along the axial direction of the wires. A proof-of-concept demonstration of this device architecture was able to successfully split HI unassisted under illumination using a Nafion-embedded pn^+-Si microwire array decorated with Pt electrocatalysts.[56] Tuning of Si microwire geometry and controlling catalyst placement at the base or side-walls of wires lead to enhanced light absorption and current densities for microwire-based photoelectrodes.[48, 57, 58] Furthermore, corrosion is self-limiting on polymer-embedded microwire photoelectrodes with protective coatings. While rapid corrosion propagates from pinholes on a planar device, corrosion is constrained locally to individual wires with pinholes due to each wire being electrically isolated from others in the array.[59] For instance, amorphous TiO_2-protected III-V nanowires grown on Si

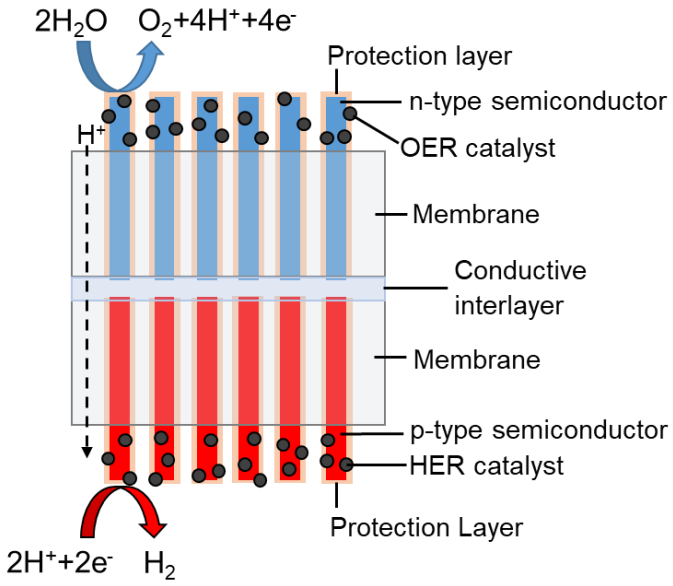

Scheme 1.2. Schematic of proposed photoelectrochemical water splitting assembly, consisting of two light absorbing semiconductor wire arrays each embedded in an ion exchange membrane and electrically connected in series with a conductive interlayer. The oxygen evolving photoanode is depicted on top and the hydrogen evolving photocathode is depicted on the bottom. Each semiconductor wire is coated with a protection layer and decorated with catalyst nanoparticles for the HER and OER on their respective sides.

exhibited > 600 h stability for the OER since corrosion at pinholes on individual wires did not propagate to adjacent wires due to the passivation of the Si substrate during operation.[60]

The demonstration of unassisted water splitting using a freestanding, tandem microwire array device remains an ongoing effort.[56, 61] In principle, two wire array photoelectrodes can be electrically connected in series using an electrical interlayer to make a monolithic tandem structure.[10, 49] In addition to making a low resistance contact to two membrane-embedded microwire arrays, this interlayer must be ion conductive, transmit light to the bottom cell, and mechanically adhere to both the wire arrays and membrane supports.[62] Previous work has been done to electrically connect two freestanding p-Si microwire arrays using a poly(3,4-ethylenedioxythiophene) polystyrene sulfonate (PEDOT:PSS) interlayer.[49] Although PEDOT:PSS forms an ohmic contact to p-

Si,[63] it exhibits poor adhesion in acidic electrolyte and absorbs strongly in wavelength regions relevant to low band gap semicondcutors.[64, 65] Conversely, the sulfonated fluoropolymer Nafion possesses superior ion conductivity, transparency, and adhesion compared to PEDOT:PSS but is electrically insulating. Chapter 4 explores the characterization of Nafion-PEDOT:PSS composites as an ohmic junction to Si electrodes for applications in an integrated, membrane-semiconductor assembly.

1.5 Scope of Thesis

This thesis focuses on the mitigation of Si corrosion when subjected to dark, open-circuit conditions in alkaline electrolyte and on the characterization of a conductive interlayer for tandem photoelectrode integration. Chapter 2 explores the use of protective electrolytes to extend open-circuit stability of Si photoanodes in alkaline electrolytes. The addition of $[Fe(CN)_6]^{3-}$ acts as an oxidizing agent to Si while minimally affecting performance of the photoelectrode to evolve $O_2(g)$. Chapter 3 further explores the concept of open-circuit stabilization of Si in alkaline electrolytes by controlling the surface potential of Si using catalytic thin films to passively drive Si oxidation and subsequently reduce system complexity. Chapter 4 investigates the bulk and interfacial properties of Nafion-PEDOT:PSS composites on Si in an effort towards implementation of a fully integrated water splitting assembly.

1.6 References

1. S. J. Davis, N. S. Lewis, M. Shaner, S. Aggarwal, D. Arent, I. L. Azevedo, S. M. Benson, T. Bradley, J. Brouwer, Y.-M. Chiang, C. T. M. Clack, A. Cohen, S. Doig, J. Edmonds, P. Fennell, C. B. Field, B. Hannegan, B.-M. Hodge, M. I. Hoffert, E. Ingersoll, P. Jaramillo, K. S. Lackner, K. J. Mach, M. Mastrandrea, J. Ogden, P. F. Peterson, D. L. Sanchez, D. Sperling, J. Stagner, J. E. Trancik, C.-J. Yang and K. Caldeira, *Science*, 2018, **360**, eaas9793.
2. N. S. Lewis, *Science*, 2016, **351**, aad1920.
3. B. Parida, S. Iniyan and R. Goic, *Renewable and Sustainable Energy Reviews*, 2011, **15**, 1625-1636.
4. M. R. Shaner, S. J. Davis, N. S. Lewis and K. Caldeira, *Energy & Environmental Science*, 2018, **11**, 914-925.
5. J. A. Dowling, K. Z. Rinaldi, T. H. Ruggles, S. J. Davis, M. Yuan, F. Tong, N. S. Lewis and K. Caldeira, *Joule*, 2020, **4**, 1907-1928.
6. M. G. Walter, E. L. Warren, J. R. McKone, S. W. Boettcher, Q. Mi, E. A. Santori and N. S. Lewis, *Chemical Reviews*, 2010, **110**, 6446-6473.
7. M. X. Tan, P. E. Laibinis, S. T. Nguyen, J. M. Kesselman, C. E. Stanton and N. S. Lewis, in *Progress in Inorganic Chemistry*, 1994, pp. 21-144.
8. J. Zhu, L. Hu, P. Zhao, L. Y. S. Lee and K.-Y. Wong, *Chemical Reviews*, 2020, **120**, 851-918.
9. C. C. L. McCrory, S. Jung, J. C. Peters and T. F. Jaramillo, *Journal of the American Chemical Society*, 2013, **135**, 16977-16987.
10. C. Xiang, A. Z. Weber, S. Ardo, A. Berger, Y. Chen, R. Coridan, K. T. Fountaine, S. Haussener, S. Hu, R. Liu, N. S. Lewis, M. A. Modestino, M. M. Shaner, M. R. Singh, J. C. Stevens, K. Sun and K. Walczak, *Angew Chem Int Ed Engl*, 2016, **55**, 12974-12988.
11. J. Jin, K. Walczak, M. R. Singh, C. Karp, N. S. Lewis and C. Xiang, *Energy & Environmental Science*, 2014, **7**, 3371-3380.
12. M. R. Singh, K. Papadantonakis, C. Xiang and N. S. Lewis, *Energy & Environmental Science*, 2015, **8**, 2760-2767.
13. S. Chabi, K. M. Papadantonakis, N. S. Lewis and M. S. Freund, *Energy & Environmental Science*, 2017, **10**, 1320-1338.
14. P. Shirvanian and F. van Berkel, *Electrochemistry Communications*, 2020, **114**, 106704.
15. L. A. King, M. A. Hubert, C. Capuano, J. Manco, N. Danilovic, E. Valle, T. R. Hellstern, K. Ayers and T. F. Jaramillo, *Nature Nanotechnology*, 2019, **14**, 1071-1074.
16. Z. Wang, Y.-R. Zheng, J. Montoya, D. Hochfilzer, A. Cao, J. Kibsgaard, I. Chorkendorff and J. K. Nørskov, *ACS Energy Letters*, 2021, **6**, 2268-2274.
17. I. A. Moreno-Hernandez, C. A. MacFarland, C. G. Read, K. M. Papadantonakis, B. S. Brunschwig and N. S. Lewis, *Energy & Environmental Science*, 2017, **10**, 2103-2108.
18. M. Gong, D.-Y. Wang, C.-C. Chen, B.-J. Hwang and H. Dai, *Nano Research*, 2016, **9**, 28-46.

19. M. Fang, W. Gao, G. Dong, Z. Xia, S. Yip, Y. Qin, Y. Qu and J. C. Ho, *Nano Energy*, 2016, **27**, 247-254.
20. S. M. Sze and K. K. Ng, in *Physics of Semiconductor Devices*, 2006, DOI: https://doi.org/10.1002/9780470068328.ch13, pp. 663-742.
21. S. Haussener, C. Xiang, J. M. Spurgeon, S. Ardo, N. S. Lewis and A. Z. Weber, *Energy & Environmental Science*, 2012, **5**, 9922-9935.
22. R. H. Coridan, M. Shaner, C. Wiggenhorn, B. S. Brunschwig and N. S. Lewis, *The Journal of Physical Chemistry C*, 2013, **117**, 6949-6957.
23. M. S. Prévot and K. Sivula, *The Journal of Physical Chemistry C*, 2013, **117**, 17879-17893.
24. M. S. Wrighton, P. T. Wolczanski and A. B. Ellis, *Journal of Solid State Chemistry*, 1977, **22**, 17-29.
25. D. Zhang, Y. Cao, S. K. Karuturi, M. Du, M. Liu, C. Xue, R. Chen, P. Wang, J. Zhang, J. Shi and S. F. Liu, *ACS Applied Energy Materials*, 2020, **3**, 4629-4637.
26. M. Gul, Y. Kotak and T. Muneer, *Energy Exploration & Exploitation*, 2016, **34**, 485-526.
27. D. Zhang, J. Shi, W. Zi, P. Wang and S. Liu, *ChemSusChem*, 2017, **10**, 4324-4341.
28. S. Hu, C. Xiang, S. Haussener, A. D. Berger and N. S. Lewis, *Energy & Environmental Science*, 2013, **6**, 2984-2993.
29. T. Wang and J. Gong, *Angewandte Chemie International Edition*, 2015, **54**, 10718-10732.
30. K. Sun, Nicole L. Ritzert, J. John, H. Tan, W. G. Hale, J. Jiang, I. Moreno-Hernandez, K. M. Papadantonakis, T. P. Moffat, B. S. Brunschwig and N. S. Lewis, *Sustainable Energy & Fuels*, 2018, **2**, 983-998.
31. H. Seidel, L. Csepregi, A. Heuberger and H. Baumgartel, *Journal of The Electrochemical Society*, 1990, **137**, 3612.
32. D. Bae, S. Shayestehaminzadeh, E. Thorsteinsson, T. Pedersen, O. Hansen, B. Seger, P. Vesborg, S. Olafsson and I. Chorkendorff, *Solar Energy Materials and Solar Cells*, 2016, **144**, 758–765.
33. W. A. Pliskin and H. S. Lehman, *Journal of The Electrochemical Society*, 1965, **112**, 1013-1019.
34. P. Allongue, V. Costa-Kieling and H. Gerischer, *Journal of The Electrochemical Society*, 1993, **140**, 1018.
35. D. Bae, B. Seger, P. C. Vesborg, O. Hansen and I. Chorkendorff, *Chem Soc Rev*, 2017, **46**, 1933-1954.
36. S. Hu, M. R. Shaner, J. A. Beardslee, M. Lichterman, B. S. Brunschwig and N. S. Lewis, *Science*, 2014, **344**, 1005-1009.
37. P. Nunez, M. H. Richter, B. D. Piercy, C. W. Roske, M. Cabán-Acevedo, M. D. Losego, S. J. Konezny, D. J. Fermin, S. Hu, B. S. Brunschwig and N. S. Lewis, *The Journal of Physical Chemistry C*, 2019, **123**, 20116-20129.
38. M. F. Lichterman, A. I. Carim, M. T. McDowell, S. Hu, H. B. Gray, B. S. Brunschwig and N. S. Lewis, *Energy Environ. Sci.*, 2014, **7**, 3334-3337.
39. Y. Zhang, X. Zhang, D. Wang, F. Wan and Y. Liu, *Applied Surface Science*, 2017, **403**, 389-395.

40. M. R. Shaner, S. Hu, K. Sun and N. S. Lewis, *Energy & Environmental Science*, 2015, **8**, 203-207.
41. K. Sun, F. H. Saadi, M. F. Lichterman, W. G. Hale, H.-P. Wang, X. Zhou, N. T. Plymale, S. T. Omelchenko, J.-H. He, K. M. Papadantonakis, B. S. Brunschwig and N. S. Lewis, *Proceedings of the National Academy of Sciences*, 2015, **112**, 3612-3617.
42. I. A. Moreno-Hernandez, B. S. Brunschwig and N. S. Lewis, *Advanced Energy Materials*, 2018, **8**, 1801155.
43. K. Sun, M. T. McDowell, A. C. Nielander, S. Hu, M. R. Shaner, F. Yang, B. S. Brunschwig and N. S. Lewis, *The Journal of Physical Chemistry Letters*, 2015, **6**, 592-598.
44. X. Zhou, R. Liu, K. Sun, K. M. Papadantonakis, B. S. Brunschwig and N. S. Lewis, *Energy & Environmental Science*, 2016, **9**, 892-897.
45. P. Buabthong, Z. P. Ifkovits, P. A. Kempler, Y. Chen, P. D. Nunez, B. S. Brunschwig, K. M. Papadantonakis and N. S. Lewis, *Energy & Environmental Science*, 2020, **13**, 4269-4279.
46. E. Verlage, S. Hu, R. Liu, R. J. R. Jones, K. Sun, C. Xiang, N. S. Lewis and H. A. Atwater, *Energy & Environmental Science*, 2015, **8**, 3166-3172.
47. K. Oh, C. Mériadec, B. Lassalle-Kaiser, V. Dorcet, B. Fabre, S. Ababou-Girard, L. Joanny, F. Gouttefangeas and G. Loget, *Energy & Environmental Science*, 2018, **11**, 2590-2599.
48. M. R. Shaner, J. R. McKone, H. B. Gray and N. S. Lewis, *Energy & Environmental Science*, 2015, **8**, 2977-2984.
49. J. M. Spurgeon, M. G. Walter, J. Zhou, P. A. Kohl and N. S. Lewis, *Energy & Environmental Science*, 2011, **4**, 1772-1780.
50. J. Kibsgaard and I. Chorkendorff, *Nature Energy*, 2019, **4**, 430-433.
51. M. J. Kenney, M. Gong, Y. Li, J. Z. Wu, J. Feng, M. Lanza and H. Dai, *Science*, 2013, **342**, 836-840.
52. Y. Chen, K. Sun, H. Audesirk, C. Xiang and N. S. Lewis, *Energy & Environmental Science*, 2015, **8**, 1736-1747.
53. S. A. Lee, T. H. Lee, C. Kim, M. G. Lee, M.-J. Choi, H. Park, S. Choi, J. Oh and H. W. Jang, *ACS Catalysis*, 2018, **8**, 7261-7269.
54. P. A. Kempler, H. J. Fu, Z. P. Ifkovits, K. M. Papadantonakis and N. S. Lewis, *The Journal of Physical Chemistry Letters*, 2020, **11**, 14-20.
55. J. M. Spurgeon, S. W. Boettcher, M. D. Kelzenberg, B. S. Brunschwig, H. A. Atwater and N. S. Lewis, *Adv Mater*, 2010, **22**, 3277-3281.
56. S. Ardo, S. H. Park, E. L. Warren and N. S. Lewis, *Energy & Environmental Science*, 2015, **8**, 1484-1492.
57. P. A. Kempler, M. A. Gonzalez, K. M. Papadantonakis and N. S. Lewis, *ACS Energy Letters*, 2018, **3**, 612-617.
58. S. Yalamanchili, H. S. Emmer, K. T. Fountaine, C. T. Chen, N. S. Lewis and H. A. Atwater, *ACS Photonics*, 2016, **3**, 1854-1861.
59. K. M. Kennedy, P. A. Kempler, M. Cabán-Acevedo, K. M. Papadantonakis and N. S. Lewis, *Nano Letters*, 2021, **21**, 1056-1061.
60. X. Shen, M. Yao, K. Sun, T. Zhao, Y. He, C.-Y. Chi, C. Zhou, P. D. Dapkus, N. S. Lewis and S. Hu, *ACS Energy Letters*, 2021, **6**, 193-200.

61. M. R. Shaner, K. T. Fountaine, S. Ardo, R. H. Coridan, H. A. Atwater and N. S. Lewis, *Energy & Environmental Science*, 2014, **7**, 779-790.
62. S. L. McFarlane, B. A. Day, K. McEleney, M. S. Freund and N. S. Lewis, *Energy & Environmental Science*, 2011, **4**.
63. M. G. Walter, X. Liu, L. E. O'Leary, B. S. Brunschwig and N. S. Lewis, *The Journal of Physical Chemistry C*, 2013, **117**, 14485-14492.
64. D. Xu, H. Shen, W. Wang, J. Xie, T. Zhang, H. Yuan, Y. Li, X. Chen, Y. He and Y. Zhang, *ChemPhysChem*, 2019, **20**, 374-382.
65. I. Zozoulenko, A. Singh, S. K. Singh, V. Gueskine, X. Crispin and M. Berggren, *ACS Applied Polymer Materials*, 2019, **1**, 83-94.

Chapter 2

SELF-HEALING SILION PHOTOANODES ENABLED BY AN ALKALINE PROTECTIVE ELECTROLYTE

2.1 Introduction

The solar-driven, photoelectrochemical (PEC) generation of sustainable fuels requires the oxidation of water to O_2 (g) as a half-reaction.[1] Silicon (Si) is a promising semiconductor for PEC water oxidation because the small band gap of Si (1.12 eV) is ideal for tandem devices, and surficial Si oxide passivates electrical defects.[2-7] Operation of PEC devices favors strongly alkaline conditions due to the availability of stable, active, and earth-abundant catalysts for the oxygen-evolution reaction (OER) and hydrogen-evolution reaction (HER) as well as the availability of anion exchange membranes that allow for robust product separation with minimal trans-membrane concentration polarization losses.[8-11] However, Si corrodes in a highly alkaline electrolyte, and requires protection strategies such as metal oxide coatings to stabilize the underlying semiconductor.[12-21] These protection layers allow for an electrical connection between the underlying semiconductor and catalytically active sites while physically blocking the electrolyte from reacting with the semiconductor. For instance, Ti^{3+} defect sites in amorphous TiO_2 allow for hole conductivity while protecting the underlying substrate from corrosion.[12, 22] Structural defects that allow the electrolyte to reach the semiconductor are expected in protective layers formed on devices at scale, and consequently could result in device failure via local corrosion of the semiconductor.[18] Efforts to decrease the pinhole density in TiO_2 layers by depositing more closely packed films have extended the lifetime of photoanodes,

but undercutting of the protective layer via any remaining pinholes inevitably leads to device failure due to pitting corrosion.[23]

Local formation of Si oxide by anodic oxidation or by illumination of the Si surface can produce Si oxide (SiO_x) that enables partial defect-tolerance of the photoelectrode under operation, by forming a passive film at pinholes in the protective layer.[24] This passivating oxide layer etches orders of magnitude more slowly than Si, and subsequently can extend the overall lifetime (> 100 h) of the electrode.[25, 26] The most stable Si photoanodes in alkaline electrolyte have consequently been obtained under continuous illumination conditions, allowing for the formation and maintenance of protective oxide layers wherever the Si directly contacts the alkaline electrolyte.[27-29] In the dark, the electrode would rest at open circuit in alkaline electrolyte, and consequently no anodic driving force is present to oxidize regions of exposed semiconductor.[26, 30] Hence unless a fully pinhole-free protective layer is present, the Si will subsequently etch rapidly by pitting that will eventually undercut the protective coating.

Modification of the electrolyte composition can have significant ramifications on electrode stability. Saturating a borate buffer electrolyte with V^{5+} has been shown to suppress corrosion of $BiVO_4$ photoanodes by inhibiting dissolution of V^{5+} from the photoelectrode.[31] Herein we report a stabilization strategy for Si photoanodes in alkaline media that is inherently distinct from, but complementary to, use of protective metal oxide coatings. Open-circuit corrosion is suppressed by adding ferricyanide ($[Fe(CN)_6]^{3-}$) to the electrolyte, which acts as an oxidizing agent and converts the surface Si in situ into a protective, passivating SiO_x layer. $[Fe(CN)_6]^{3-}$ readily reduces to ferrocyanide ($[Fe(CN)_6]^{4-}$) in a one-electron transfer reaction, and $[Fe(CN)_6]^{3-}$ has been previously shown in the

micromachining field to anodically passivate Si in potassium hydroxide (KOH), preventing the formation of etch pits.[32, 33] Introducing $[Fe(CN)_6]^{3-}$ to the anolyte component of a membrane-separated PEC cell prevents the $[Fe(CN)_6]^{4-}$ from being reduced at the cathode but the $[Fe(CN)_6]^{4-}$ is reoxidized under illumination. This strategy allows for anodic passivation to occur through two different pathways for operation both under illumination and in the dark. An advantage of the protective electrolyte protection scheme is that the electrode simply needs to be in contact with the protective electrolyte to prevent rapid corrosion, therefore acting in synergy with potentially defective protective coatings.

2.2 Materials and Methods

2.2.1 Chemicals

All chemicals were used as received, including potassium hydroxide (KOH, Macron Fine Chemicals, NF/FCC grade), potassium ferricyanide ($K_3Fe(CN)_6$, Fischer Chemical, Certified ACS), potassium ferrocyanide trihydrate ($K_4Fe(CN)_6 \cdot 3H_2O$, Fischer Chemical, Certified ACS), hydrochloric acid (HCl, EMD Millipore Co., 36-38%), hydrogen peroxide (H_2O_2, EMD Millipore Co., 30%), buffered oxide etchant (BOE, 6:1 NH_4F to HF, Transene Company, Inc.), and gallium-indium eutectic (Alfa Aesar, 99.99%). Deionized water (18.2 MΩ cm resistivity) was obtained from a Barnstead Millipore system.

2.2.2 Electrode Preparation

Both n-type (phosphorous doped, 0.1-1.0 Ω cm, (100)-oriented) and p^+-type (boron doped, 0.001-0.005 Ω cm, (100)-oriented) Si wafers were purchased from Addison Engineering. Boron diffusion doping was used to create an np^+ junction on the n-type

wafer. Prior to doping, n-type wafers were cleaned by etching in BOE for 30 s followed by immersion in 6 : 1 : 1 H_2O : HCl : H_2O_2 (by volume) at 75 ˚C for 15 min. The wafers were then rinsed with deionized water and dried under flowing N_2(g).

The tube furnace used for diffusion doping had an O_2 flow at 950 ˚C for 30 min to oxidize boron nitride wafers (Saint-Gobain, BN-975 PDS). The gas supply was switched from O_2 to N_2 and the furnace was cooled to 750 ˚C before inserting cleaned n-type wafers. A p^+-emitter was formed after increasing the temperature back to 950 ˚C under N_2, and the temperature was maintained for 30 min. After diffusion doping, the sample was left to cool to room temperature and then submerged in BOE for 2 min to deglaze B_2O_3 from the surface. Low temperature oxidation at 750 ˚C under O_2 for 20 min was performed to remove surface defects. The sample was then submerged in BOE until the surface was no longer hydrophilic. A sheet resistance of ~ 40-70 Ω/sq was obtained using a four-point probe (Jandel).

An array of Ni catalyst microelectrodes (μNi), with a 3 μm diameter and 7 μm pitch, was patterned onto Si wafers using photolithography. The Si wafer was rinsed with deionized water and MCC primer 80/20 (Microchem Corp.) was deposited onto the surface via spin coating at 3000 rpm for 1 min. Shipley 1813 photoresist was then coated at 3000 rpm for 1 min and then heated for 1 min at 110 ˚C. The pattern was exposed to UV light through a chrome mask to define the array. The exposed regions were washed away using MF-319 developer (Microchem Corp.) for 2 min, and were then rinsed with deionized water. The patterned wafer was baked at 110 ˚C. Prior to Ni deposition, the patterned wafer was etched with BOE for 30 s. The Ni catalyst was deposited using radio-frequency (RF) sputtering with an AJA Orion sputtering system at 100 W for 1 h (Ni target from Kurt J.

Lesker Company). The Ar flow rate during sputtering was maintained at 20 sccm to maintain the plasma while the chamber pressure was 5 mTorr. After sputtering, the photoresist of the patterned wafers was removed by submerging the wafer in acetone and gently sonicating for at least 30 min. Unpatterned p^+-Si wafers for activity and faradaic efficiency measurements had a Ni overlayer similarly deposited using the BOE etch and sputtering steps as described.

Electrodes were fabricated by first cleaving the sample with a carbide scribe to the desired area. Electrodes in contact with $[Fe(CN)_6]^{3-}$ and KOH electrolyte in Fig. 2.1 had areas between 10-15 mm^2, and each run showed similar performance and stability. Wafers that went through either diffusion doping and/or Ni sputtering had their edges cleaved and discarded to prevent shunts during operation. In-Ga eutectic (Ted Pella) was scratched onto the backs of the sample and affixed to a Sn-coated Cu wire using Ag paint (Ted Pella). The wire was threaded through a glass tube and the edges of the sample were sealed to the glass using epoxy (Loctite 9460). The epoxy was cured at 100 ˚C in an oven for at least 2 h prior to use. The exposed electrode area was determined by using an optical scanner (Epson perfection V370) and analyzing the image using ImageJ software.

2.2.3 Cell preparation and (photo)electrochemical testing

All (photo)electrochemical experiments were done in a cell with catholyte and anolyte sides separated by an anion-exchange membrane (AEM), unless otherwise specified. Glass cells were cleaned in aqua regia (4:1 HCl : HNO_3 by volume) and rinsed with deionized water before use. Unless otherwise specified, $[Fe(CN)_6]^{3-}$ and/or KOH were dissolved in deionized water at 10 mM and 1.0 M (pH = 13.6), respectively, and 25 mL of

solution was added to the anolyte side. The anolyte was bubbled with O_2 unless otherwise stated. The catholyte side was filled with 1.0 M KOH(aq) and Ni wire was used as the counter electrode. Fumasep (Fuel Cell Store) was used as the AEM to separate the two compartments and prevent crossover of $[Fe(CN)_6]^{3-}$ from reaching the catholyte. Hg/HgO reference electrodes were used for all three-electrode experiments. The reference electrodes were calibrated relative to a reversible hydrogen electrode (RHE), which involved comparing the potential difference between the Hg/HgO electrode and a Pt disk electrode in H_2-saturated 1.0 M KOH(aq). The potentials of reference electrodes used ranged from 0.904 to 0.918 V vs. RHE. Unless otherwise specified, illumination was provided with an ELH tungsten-halogen lamp through a UV long pass ($\lambda < 400$ nm) filter and was calibrated to 100 mW cm^{-2} using a calibrated Si photodiode (Thorlabs). Electrochemical measurements were performed using an MPG-2 potentiostat (Bio-Logic Science Instruments).

All current measurements were normalized to current density (J) based on the measured electrode area. Ni-coated samples were activated in KOH prior to testing in KOH or KOH and $[Fe(CN)_6]^{3-}$ by 20 cyclic voltammetry (CV) cycles between 0.53 V and 1.83 V vs. RHE at 40 mV s^{-1}. This activation step has been shown to improve catalytic activity by incorporating Fe from the solution into the catalyst and forming NiFeOOH.[9] Photoelectrodes were subjected to 6 h of illumination under potential control followed by 18 h in the dark at open circuit. A Python script was used to automate turning on and off the lamp at these time intervals followed by 30 s of wait time before starting data collection. For Fig. 2.1, four electrodes were tested in KOH(aq) with $[Fe(CN)_6]^{3-}$ while three electrodes were tested in KOH(aq) alone. Unless otherwise stated, electrodes were held at

1.63 V vs RHE when actively performing water oxidation. For np^+-Si photoelectrodes this potential corresponds to the location of the hole quasi Fermi level during O_2 evolution with this electrocatalyst whereas for dark p^+-Si electrodes this potential is sufficient to overcome the catalyst overpotential and evolve O_2(g) at a current density of ~ 20-30 mA cm^{-2}. The actual operating potential in a tandem structure will depend in detail on the overall photovoltage and photocurrent of the system.[2, 34, 35] Extensive precedent exists for testing Si electrodes at or near this potential as a representative potential that is slightly positive of, and thus slightly oxidatively stressful relative to, the maximum power point for the photoanode considering the overpotential for the OER electrocatalyst and fill factor losses in the photoelectrode itself.[13-16, 27-29]

To assess performance of np^+-Si/μNi photoanodes, the fill factor (*FF*) was calculated using the following equation:

$$FF = \frac{V_{MP} J_{MP}}{V_{OC} J_{SC}} \tag{2.1}$$

where (V_{MP}, J_{MP}) is the maximum power point, V_{OC} is the open-circuit voltage, and J_{SC} is the current density evaluated at the Nernstian potential of the redox couple of interest in the cell.

Faradaic efficiency measurements were based on a previously published procedure.[26] Briefly, a p^+-Si sample coated with ~100 nm of Ni was submerged in the anolyte (KOH or KOH and $[Fe(CN)_6]^{3-}$) in a two-electrode experiment with an inverted burette over the sample. The Ni counter electrode in the KOH catholyte was separated from the other compartment by a Fumasep membrane. A galvanostatic current of 40 mA cm^{-2} was applied and the volume of O_2 collected was measured by the inverted burette. 40 mA cm^{-2} represents an achievable current density with Si photoanodes that is just below the

theoretical maximum of Si (43.3 mA cm^{-2}) expected under illumination of a Si photoanode with 100 mW cm^{-2} of the AM 1.5G solar spectrum.[36, 37]

2.2.4 Etch Rate Experiment

A thermal oxide was grown at 950 ˚C on (100)- and (111)-oriented p^+-Si for 6 h and 4.5 h, respectively. Ellipsometry measurements indicated an oxide thicknesses of 170-180 nm. After thermal oxide growth, an array of 10 μm by 100 μm rectangles was patterned by standard photolithography procedures. The patterned wafers were then submerged in BOE for 3 min to ensure that all exposed oxide was etched, leaving behind trenches that went down to bare Si surfaces. The wafers were then sonicated in acetone to remove the photoresist. Samples were introduced to either 1.0 M KOH(aq) or 1.0 M KOH(aq) and 10 mM $[Fe(CN)_6]^{3-}$ electrolytes in the dark at open circuit. After the samples were allowed to etch for a set amount of time, the samples were submerged in BOE for 5 min to remove all oxide. For atomic-force microscopy (AFM) measurements, the samples were affixed to a stainless steel disk using carbon tape.

The resulting height difference between the exposed Si and the Si layer protected by the thermal oxide was quantified with AFM (Bruker Dimension Icon). Peak Force Tapping mode was used to collect the data, which tracked the surface topography by relying on a feedback based on the maximum force between the probe and sample for each tapping cycle. The Peak Force amplitude and frequency were set to 100 nm and 2 kHz, respectively, and a ScanAsyst-Air probe (Bruker) with a nominal tip radius of 2 nm was used.

2.2.5 Materials Characterization

A FEI Nova NanoSEM 450 was used to take scanning electron micrographs (SEMs). The SEMs were measured at a working distance of 5.0 mm and accelerating voltages of 10 kV. Photoelectrodes after testing were prepared by removing the epoxy with a razor blade and cleaving through the center. Each of the two cleaved pieces were affixed to either side of a 45˚ SEM mount with carbon tape, to examine the surface topography as well as the cross section of the sample.

UV-vis spectroscopy was performed on an Agilent 8453 spectrometer. The 10 mM $[Fe(CN)_6]^{3-}$ and 1.0 M KOH(aq) electrolyte was illuminated under nominally the same conditions as the photoelectrode. The electrolyte was diluted 1 : 10 with deionized water before taking measurements. A series of standard solutions with 0.10 M KOH(aq) and either 0.33 mM, 0.5 mM, 0.67 mM, or 1 mM $[Fe(CN)_6]^{3-}$ was also prepared by weighing the amount on a scale and dissolving in deionized water. The concentrations of $[Fe(CN)_6]^{3-}$ and $[Fe(CN)_6]^{4-}$ were also measured by fitting the 420 nm (A_{420}) and 260 nm (A_{260}) absorbance peaks to the following correlation[38]

$$A_{420} = 1.058[Fe(CN)_6^{3-}] - 0.003[Fe(CN)_6^{4-}] \quad (2.2)$$

$$A_{260} = 1.260[Fe(CN)_6^{3-}] + 2.724[Fe(CN)_6^{4-}]. \quad (2.3)$$

X-ray photoelectron spectroscopy (XPS) was performed using a Kratos Axis Ultra system with a base pressure of 1 x 10^{-9} Torr in the analysis chamber. A monochromatic Al Kα source was used to irradiate the sample with X- rays (1486.7eV) at 450 W. A hemispherical analyzer oriented for detection along the sample surface normal was used for maximum depth sensitivity. High-resolution spectra were acquired at a resolution of 25

meV with a pass energy of 10 eV. The data were analyzed using CasaXPS computer software. First, the spectra were calibrated by referencing the C 1s peak position to 284.8 eV. Si 2p, Fe 2p, N 2p, O 1s peaks were then fitted to multiple subspecies each having Gaussian-Lorentz peak shapes. XPS data were obtained ex-situ, i.e., after a short sample transfer through air, which could potentially confound linking the surface composition and oxidation states found in UHV to the ones involved during electrocatalysis.

2.3 Results and Discussion

2.3.1 Photoelectrochemical Behavior of Silicon Photoanodes in a Protective Electrolyte

Figure 2.1a compares the current density vs time behavior for np^+-Si(100) photoanodes partially coated (~ 14% filling fraction) with Ni islands (μNi) in 1.0 M KOH(aq) with, and without, respectively, 10 mM $[Fe(CN)_6]^{3-}$. The photoelectrodes were held at 1.63 V vs the reversible hydrogen electrode (RHE) and were subjected to simulated, UV-filtered sunlight of 100 mW cm^{-2} illumination in 6 h intervals ("day"), followed by 18 h at open circuit in the dark ("night"). The lack of UV illumination from the ELH lamp is appropriate for proof-of-concept of the protective electrolyte approach because, for unassisted water splitting, Si would only be used in a tandem structure and the UV light would be filtered and absorbed by the higher band gap top cell before reaching the Si bottom cell. Representative np^+-Si/μNi photoanodes exhibited 580±20 mV photovoltage (Fig. 2.2 and Table 2.1). The photoanode was stable for at least twelve day/night cycles (288 h) in 10 mM $[Fe(CN)_6]^{3-}$, 1.0 M KOH(aq) but failed at the end of the fifth day/night cycle (120 h) in 1.0 M KOH(aq). Fig. 2.3 shows that the light intensity of the lamp did not

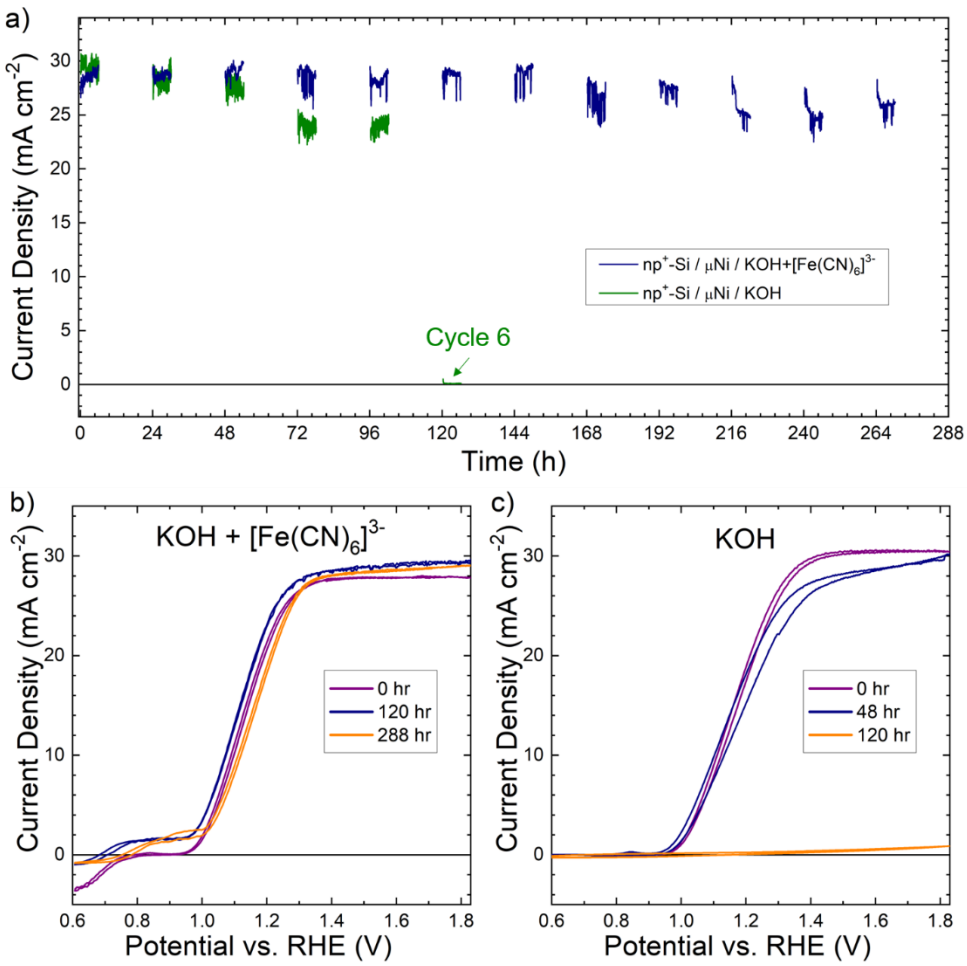

Figure 2.1. Chronoamperometric stability and performance of np^+-Si(100)/μNi electrodes in 1.0 M KOH(aq) with and without, respectively, 10 mM $[Fe(CN)_6]^{3-}$. (a) Stability in KOH(aq) (blue) or in $[Fe(CN)_6]^{3-}$, KOH(aq) (green). Chronoamperometric data were taken for 6 h intervals at 1.63 V vs RHE under 100 mW cm^{-2} illumination provided by an ELH-type W-halogen lamp with a long pass filter, followed by 18 h in the dark at open circuit. Cyclic voltammograms of np^+-Si(100)/μNi electrodes in (b) 1.0 M KOH(aq) and 10 mM $[Fe(CN)_6]^{3-}$ and (c) 1.0 M KOH(aq) collected periodically during the chronoamperometric stability test. The scan rate of the cyclic voltammograms is 100 mV s^{-1}.

vary substantially between each day cycle during stability tests. In 10 mM $[Fe(CN)_6]^{3-}$, 1.0 M KOH(aq) (Fig. 2.1b) the photoanode exhibited a fill factor of 0.40±0.02 and retained this value, within experimental error, for the majority of the stability test (Table 2.1); the photocurrent density increased slightly, by < 2 mA cm^{-2}; and the photovoltage shifted slightly positively by ~ 40 mV between 120 to 288 h of operation. In contrast, in 1.0 M

KOH(aq) under 1 atm O_2 (Fig. 2.1c), after 48 h the photoanode exhibited a notable decrease in fill factor from 0.37±0.04 to 0.27, and the electrode failed completely, with no substantial photocurrent, after 120 h of operation.

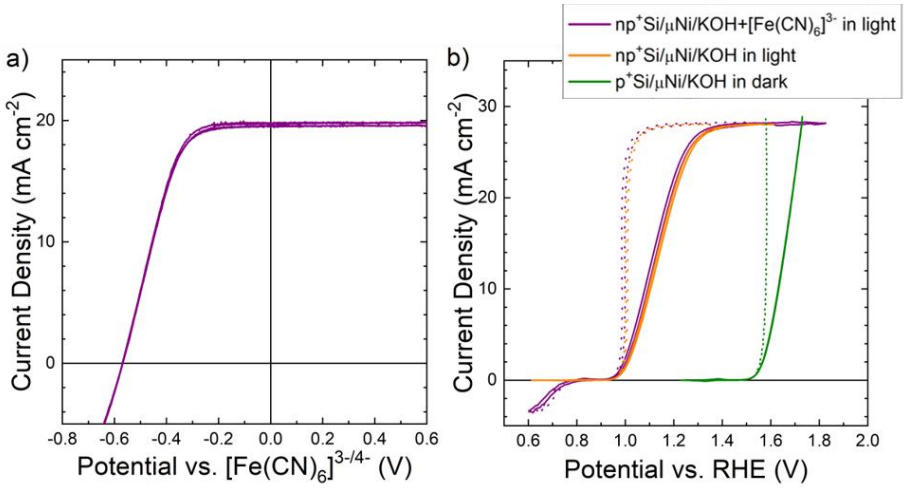

Figure 2.2. Cyclic voltammograms of p^+- or np^+-Si(100)/μNi electrodes in either dark or under 100 mW cm^{-2} illumination, respectively. (a) np^+-Si(100)/μNi in contact with the $[Fe(CN)_6]^{3-/4-}$ redox couple (0.35 M $[Fe(CN)]^{3-}$, 0.050 M $[Fe(CN)_6]^{4-}$, and 0.50 M KCl(aq)). No long-pass filter was used, and the open-circuit voltage is 570 mV. (b) np^+-Si(100)/μNi in contact with 1.0 M KOH(aq) and 10 mM $[Fe(CN)_6]^{3-}$ (purple) or 1.0 M KOH(aq) (orange); p^+-Si(100)/μNi in contact with 1.0 M KOH(aq) (green). Measured data (solid lines) were adjusted by subtracting series resistance (dashed lines) to estimate the photovoltage (580 mV). The scan rate for the cyclic voltammograms was 40 mV s^{-1}.

Table 2.1. Performance of np^+-Si(100)/μNi photoanodes

Figure	Electrolyte[a]	Hours tested (h)	Fill factor[b]	J_{SC}[b] (mA cm^{-2})	V_{OC}[b] (V)
2.1b	$[Fe(CN)_6]^{3-}$, KOH, O_2 sat.	0	0.40±0.02	27±2	0.58±0.02
2.1b	$[Fe(CN)_6]^{3-}$, KOH, O_2 sat.	48	0.38±0.02	27±2	0.59±0.02
2.1b	$[Fe(CN)_6]^{3-}$, KOH, O_2 sat.	120	0.40±0.02	28±1	0.58±0.02
2.1b	$[Fe(CN)_6]^{3-}$, KOH, O_2 sat.	216	0.35±0.05	28±1	0.55±0.04
2.1b	$[Fe(CN)_6]^{3-}$, KOH, O_2 sat.	288	0.34	28	0.55
2.1c	KOH, O_2 sat.	0	0.37±0.04	29±2	0.58±0.02
2.1c	KOH, O_2 sat.	48	0.27	29	0.59
2.1c	KOH, O_2 sat.	120	N/A[c]	N/A[c]	N/A[c]
2.7b	KOH	0	0.35	30	0.57
2.7b	KOH	48	0.18	21	0.52
2.7b	KOH	72	N/A[c]	N/A[c]	N/A[c]

[a]$[Fe(CN)_6]^{3-}$ concentration is 10 mM; KOH concentration is 1.0 M
[b]Error bars indicate multiple samples tested for each time indicated
[c]Electrode experienced complete failure

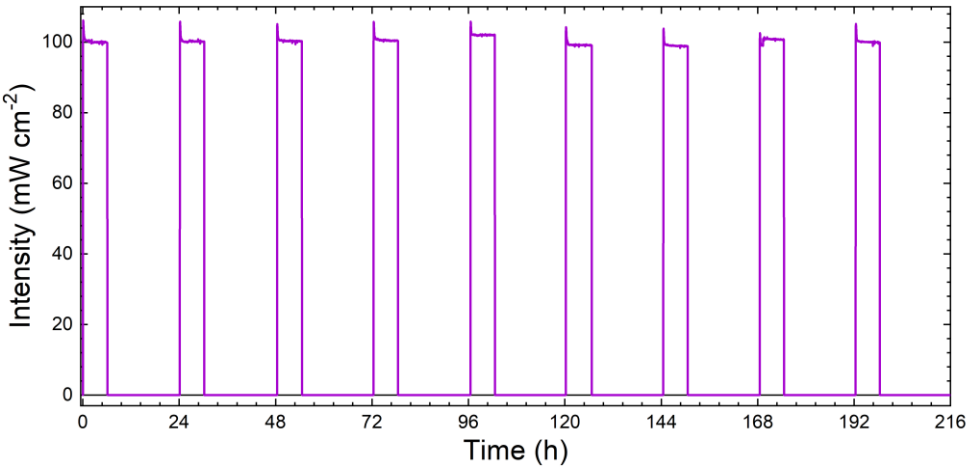

Figure 2.3. Representative light intensity as a function of time used for stability tests with simulated day/night cycles. A calibrated photodiode monitored the illumination from a Xe arc lamp with an AM 1.5 filter.

X-ray photoelectron spectroscopy (XPS) was performed before contact with the electrolyte and after one day/night cycle in both 1.0 M KOH(aq) and in the protective electrolyte (Fig. 2.4). The ratios of the SiO_2/Si peaks for samples prior to operation in 1.0 M KOH(aq), and for samples then immersed in 1.0 M KOH(aq) without and with 10 mM $[Fe(CN)_6]^{3-}$, respectively, were 0.44, 0.31, and 0.54. The presence of $[Fe(CN)_6]^{3-}$ thus increased the amount of SiO_2 on the surface whereas the lack of $[Fe(CN)_6]^{3-}$ led to etching of the initial native oxide layer as well as any subsequent anodic oxide grown during the illumination step. The ratios of the Si_2O/SiO_2 peaks for samples immersed in KOH(aq) without and with 10 mM $[Fe(CN)_6]^{3-}$, respectively, were 2.75 and 1.94. The oxygen content of the SiO_x film immersed in KOH(aq) was thus lower than that for the sample in KOH(aq) and $[Fe(CN)_6]^{3-}$, possibly due to the lack of a viable mechanism for oxide regrowth in KOH(aq) at open circuit.[39] Operation in either electrolyte produced a decrease in the Ni/NiO_x signal, indicating that the Ni pre-electrocatalyst was converted to its NiOOH form

after operation, with or without $[Fe(CN)_6]^{3-}$ in solution.[26] No substantial Fe peaks were detected in 1.0 M KOH(aq) due to the relatively low surface coverage of electrocatalyst, whereas trace amounts of Fe_2O_3 were deposited on the surface when the sample was operated in the protective electrolyte.

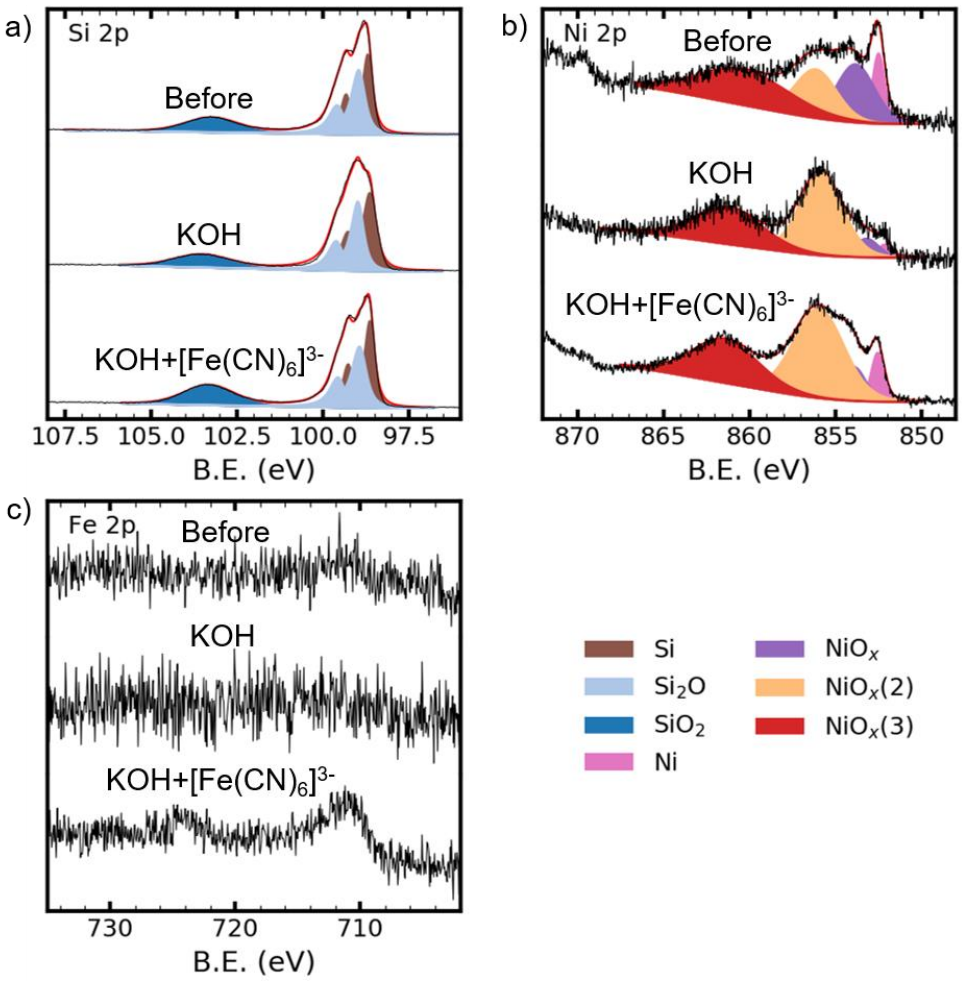

Figure 2.4. High-resolution XPS data of np^+-Si/μNi photoelectrodes in the (a) Si 2p, (b) Ni 2p, (c) Fe 2p regions. For each element, the top spectrum was obtained before simulated day/night cycling of the illumination, whereas the other spectra were obtained after 6 h under illumination at 1.63 V vs RHE, followed by 18 h at open circuit in the dark, in 1.0 M KOH(aq) (middle) and in the protective electrolyte (bottom). The y-axis is in arbitrary units.

Fig. 2.5 depicts scanning-electron micrographs (SEMs) of the photoelectrodes before and after extended photoelectrochemistry under potential control in the protective electrolyte or in 1.0 M KOH(aq). After chronoamperometry in the protective electrolyte for 264 h (Fig. 2.5c-d), etching of the passivating SiO_x was observed at the exposed Si surface. Beneath the μNi the Si was undercut radially, leading to the formation of nanoscale pillar structures. Some delamination of μNi was observed, but most of the μNi remained intact after chronoamperometry, indicating some protection in the direction axial (normal to the surface) to the underlying p^+-emitter. In contrast, Fig. 2.5e-f show the complete failure of the photoelectrode in 1.0 M KOH(aq), with no intact μNi remaining on the surface. Only the pyramid-shaped structures formed from exposed (111) Si facets remained at the center of where the μNi islands were initially located. Partial pyramid formation was observed over the remainder of the surface. The loss of any appreciable photocurrent after 120 h in the corresponding choronoamperogram (Fig. 2.1a) is thus consistently ascribable to complete delamination of the μNi.

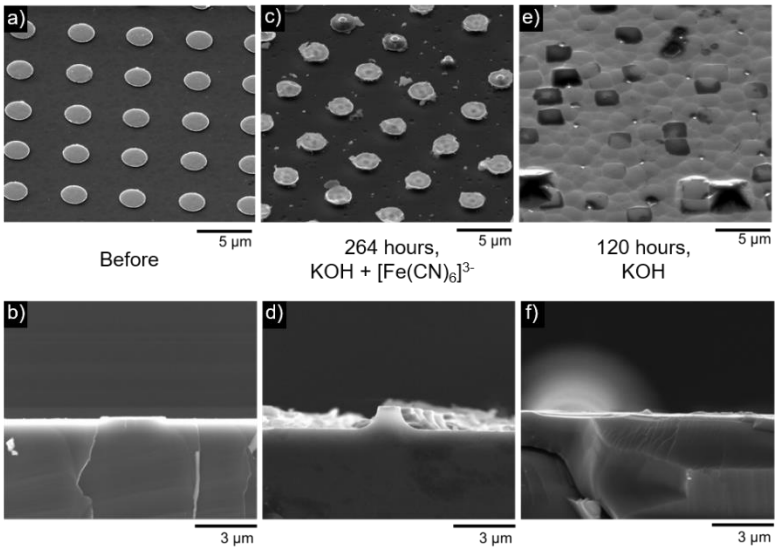

Figure 2.5. Scanning-electron micrographs of np^+-Si(100)/μNi electrodes. (a-b) Top-down (a) and cross section (b) of electrodes before day/night cycling. (c-d) Top-down (c) and cross-section (d) after 264 h in 10 mM $[Fe(CN)_6]^{3-}$, 1.0 M KOH(aq). (e-f) Top-down (e) and cross-section (f) after 133 h in 1.0 M KOH(aq).

A continuous protective layer on Si would likely lead to longer lifetimes due to limiting the exposed Si to only the regions where pinholes were present in the protective layer, but the distribution and area exposed due to possible pinholes is not generally well defined under such conditions.[12, 18] The μm-scale dimensions of the Ni catalysts is sufficient to provide protection to Si directly underneath the Ni, providing insight into possible uses of the protective electrolyte in tandem with protective layers to enhance the stability of Si photoanodes in alkaline electrolytes. In a previous study, the lifetime of Si/μNi photoanodes in 1.0 M KOH(aq) was observed to be ~ 42 h at open-circuit and ~ 240 h under continuous illumination.[26] In this work, addition of an oxidizing agent, $[Fe(CN)_6]^{3-}$, extended the lifetimes at open circuit while not hindering performance during operation, leading to device lifetimes under periodic illumination that were comparable to those exhibited by the electrode under continuous illumination.

The actual electrode lifetime depends on the formation and dissolution of the surface oxide and etching at the device junction and/or catalyst interface. In the np^+-Si/μNi system, the point of failure arises from the corrosion of the p^+-emitter layer exposed to the electrolyte, followed by the undercutting of the μNi catalyst until the p^+-emitter is fully etched and/or the catalyst is delaminated. As shown in Fig. 2.1b, this process of undercutting minimally affects the photocurrent or fill factor of the electrode, whereas a ~ 40 mV increase in overpotential occurs as some catalyst delaminates and lowers the number of active sites for OER. The lifetime of the np^+-Si/μNi structure could be further increased by using a larger radius for the μNi, to retard the undercutting process. The μNi thus constitutes a partial protection layer, offering protection to the underlying Si in the axial direction but no radial protection if the Si is undercut. Larger μNi radii lead to longer

lifetimes before the underlying emitter is etched, at the penalty of producing higher parasitic optical absorption by the opaque μNi precatalyst. A photoelectrode with a 14% catalyst filling fraction would have > 90% of the photocurrent exhibited by a photoanode with a 1% filling fraction, and sufficiently high filling fractions (> 10%) will minimally affect the fill factor of the device compared to photoanodes covered by a continuous metal film.[26, 40]

2.3.2 Influence of Dissolved Oxygen on Photoelectrode Stability in 1.0 M KOH(aq)

The extent to which O_2 passivates Si in alkaline electrolytes is an important parameter in determining the efficacy of $[Fe(CN)_6]^{3-}$ as a passivating agent. Fig. 2.6 compares the surfaces of np^+-Si/μNi photoanodes at open circuit after 24 h in 1.0 M KOH(aq) with and without, respectively, saturating the electrolyte with 1 atm of O_2(g) (~ 0.2 mM dissolved). The solutions were both fully exposed to ambient air (~ 0.2 atm O_2). After 24 h, the Si surface that was in contact with the 1 atm O_2-saturated solution showed no visible facet-dependent etching of the Si surface or μNi delamination, whereas the Si surface that was in contact with the solution in a sealed cell that was not continuously bubbled with O_2 exhibited a roughened surface with no visible μNi. Fig. 2.7 depicts a photoanode in 1.0 M KOH(aq) that had been subjected to day/night cycles without 1 atm O_2 bubbling in solution. During operation in day/night cycles, the solution presumably became saturated with O_2 during periods of illumination, with the resulting O_2 thus partially stabilizing the Si surface during the dark periods. The photoanode that evolved O_2 for more than one cycle (24 h) lasted longer than a photoanode that had been left at open circuit, but a substantial decrease in photocurrent density (> 8 mA cm^{-2}) and fill factor

(from 0.35 to 0.18) occurred at 48 h and complete failure of the electrode occurred at 72 h of day/night operation. Bubbling O_2 in 1.0 M KOH(aq) extended the photoanode lifetime to 120 h, but the eventual catastrophic failure suggests that the kinetics for surface passivation via dissolved O_2 does not fully compete with the kinetics of Si dissolution in base. Chapter 3 further explores the effects of O_2 on Ni-coated Si surfaces.

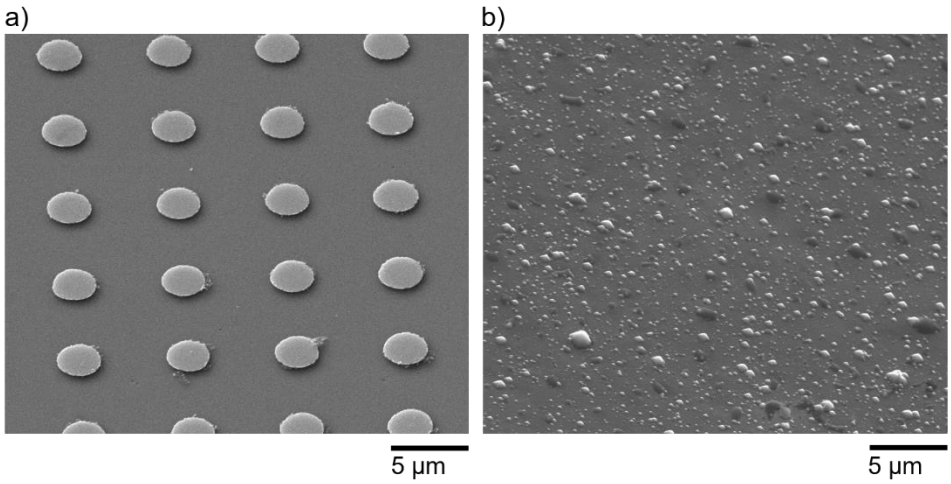

Figure 2.6. Scanning-electron micrographs comparing np^+-Si/μNi etching in a sealed cell containing 1.0 M KOH(aq) with (a) and without (b) bubbling O_2 for 24 h in the dark at open circuit.

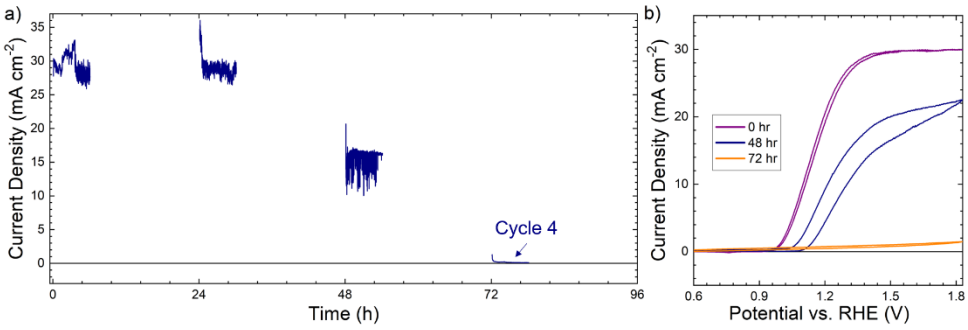

Figure 2.7. Chronoamperometric stability and performance of np^+-Si(100)/μNi electrodes in 1.0 M KOH(aq) without O_2 bubbling. (a) Chronoamperometric data were taken in 6 h intervals at 1.63 V vs RHE under 100 mW cm^{-2} of illumination, followed by 18 h in the dark at open circuit. (b) Current density vs potential behavior in 1.0 M KOH(aq) at a scan rate of 100 mV s^{-1}.

2.3.3 Electrochemical Potentials in a Protective Electrolyte

Fig. 2.8 shows the potentials measured at a Pt electrode for various molar ratios of $[Fe(CN)_6]^{3-}$ to $[Fe(CN)_6]^{4-}$ in either 1.0 M KOH(aq) or deionized water. The measured potentials ranged from ~ 0.3 to ~ 0.6 V vs the normal hydrogen electrode (NHE), comparable to E^0'(O_2/OH^-) = 0.401 V vs NHE at pH 14 and consistent with Nernstian behavior. The potential of $[Fe(CN)_6]^{3-/4-}$ depends on the ionic strength,[41] and as expected exhibited a ~ 100 mV positive shift in 1.0 M KOH(aq) compared to in deionized H_2O. The passivation potential of Si in 1.0 M KOH(aq) is ~ 0.5 vs RHE (~ -0.3 V vs NHE at pH 14),[25, 29] so either holding a Si electrode passively in $[Fe(CN)_6]^{3-/4-}$ or at potentials for water oxidation is expected to produce a sufficiently positive potential to oxidize the Si surface.

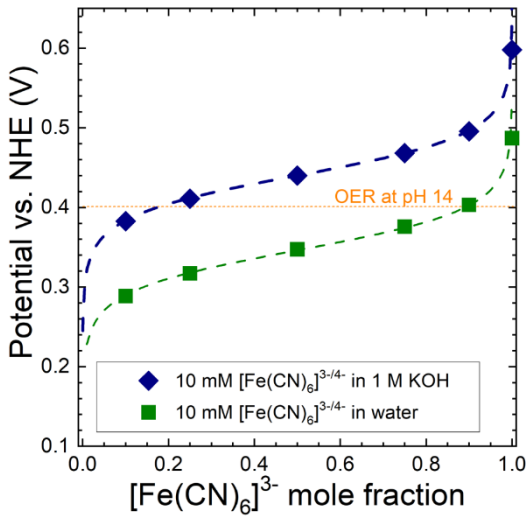

Figure 2.8. Nernst potentials of 10 mM $[Fe(CN)_6]^{3-/4-}$ solutions. The measured data points were based on open-circuit potentials of a Pt working electrode at different mole fractions of $[Fe(CN)_6]^{3-}$ to $[Fe(CN)_6]^{4-}$ in 1.0 M KOH(aq) (blue) or deionized H_2O (green). The dashed blue and green lines were calculated using the Nernst Equation. The dashed orange line represents the potential versus NHE of the OER at pH 14.

The behavior of Si electrodes in the dark was elucidated further by investigating the open-circuit potential (E_{oc}) under various conditions. Fig. 2.9 compares the E_{oc} values measured over 18 h cycles for p^+-Si electrodes with and without μNi, in contact with O_2-saturated 1.0 M KOH(aq) with or without $[Fe(CN)_6]^{3-}$. Each cycle was preceded by 6 h at 1.58 V vs RHE during which time the Si surface passivated and produced SiO_x.[24] In 1.0 M KOH(aq), E_{oc} after each cycle of potential control was -0.07±0.01 V for p^+-Si and was 0.41±0.07 V for p^+-Si/μNi. After ~ 1 h at E_{oc} for p^+-Si in 1.0 M KOH(aq), E_{oc} was ~ 0.1 V before settling at -0.07 V, which corresponds to removal of the surface SiO_x, followed by etching of the underlying Si.[30] Along with relatively steady, positive potentials across all four cycles effected by the equilibration of μNi with electrolyte, the p^+-Si/μNi electrode in 1.0 M KOH(aq) did not exhibit this decrease in E_{oc} to -0.07 V, indicating that Ni remained intact on the Si surface. In 1.0 M KOH(aq) containing $[Fe(CN)_6]^{3-}$, E_{oc} was 0.99±0.02V vs RHE for p^+-Si and was 1.32±0.03 V for p^+-Si/μNi. The potential of 1.43 V vs RHE for p^+-Si/μNi was comparable to that of a Pt electrode in the protective electrolyte, suggesting that the surface potential of the p^+-Si/μNi electrode equilibrated near the Nernstian potential of $[Fe(CN)_6]^{3-/4-}$ at open circuit. The p^+-Si potential was comparatively less positive and complicated by the lack of metallic contact. Regardless of the presence of Ni, compared to in 1.0 M KOH(aq) the protective electrolyte increased E_{oc} to potentials that were well above (> 0.5 V) the passivation potential of Si.

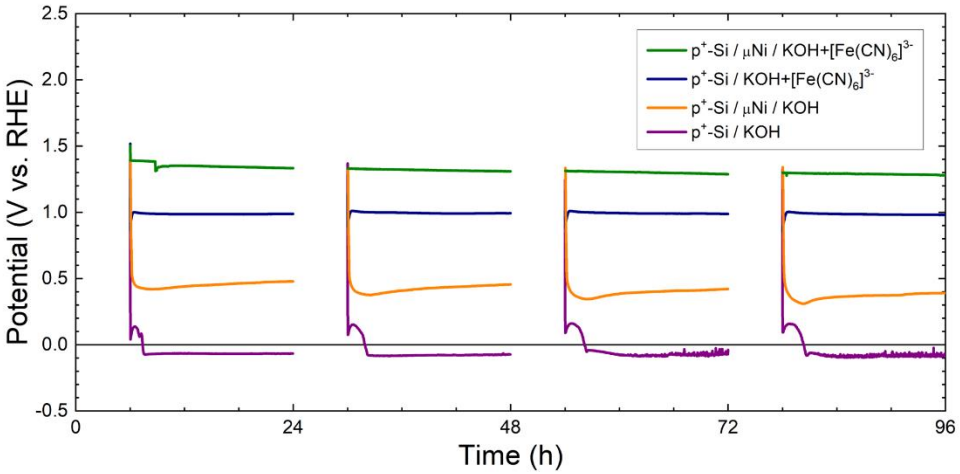

Figure 2.9. Open-circuit potential of p^+-Si electodes and of p^+-Si electrodes coated with μNi, respectively, in contact with 1.0 M KOH(aq) or 1.0 M KOH(aq) with 10 mM $[Fe(CN)_6]^{3-}$. The gaps in collected data indicate intervals during which the electrode was held at 1.579 V vs RHE. The purpose of this experiment was to evaluate the potential at which the surface equilibrated in the dark. Si does not photocorrode under these conditions,[42, 43] so the E_{OC} for the photoactive material is not directly relevant to the issue being addressed experimentally.

2.3.4 Etch Rates of Si/SiO_x

Various descriptions of the Si and SiO_x corrosion process in alkaline electrolyte have been provided.[25, 32, 44-46] Experimental evidence indicates that reduction of $[Fe(CN)_6]^{3-}$ on p-Si anodes in alkaline electrolytes proceeds via surface intermediates,[33] suggesting that the interaction of an oxidant with reaction intermediates plays a key role in determining oxide formation. Scheme 2.1 provides one possible scheme in which the SiO_x growth and dissolution is preceded by hole injection via positive bias or $[Fe(CN)_6]^{3-}$, whereas Si dissolution occurs in the absence of injected holes.[44] The relative rates of Si and SiO_x dissolution are thus critical towards stabilizing Si photoanodes.

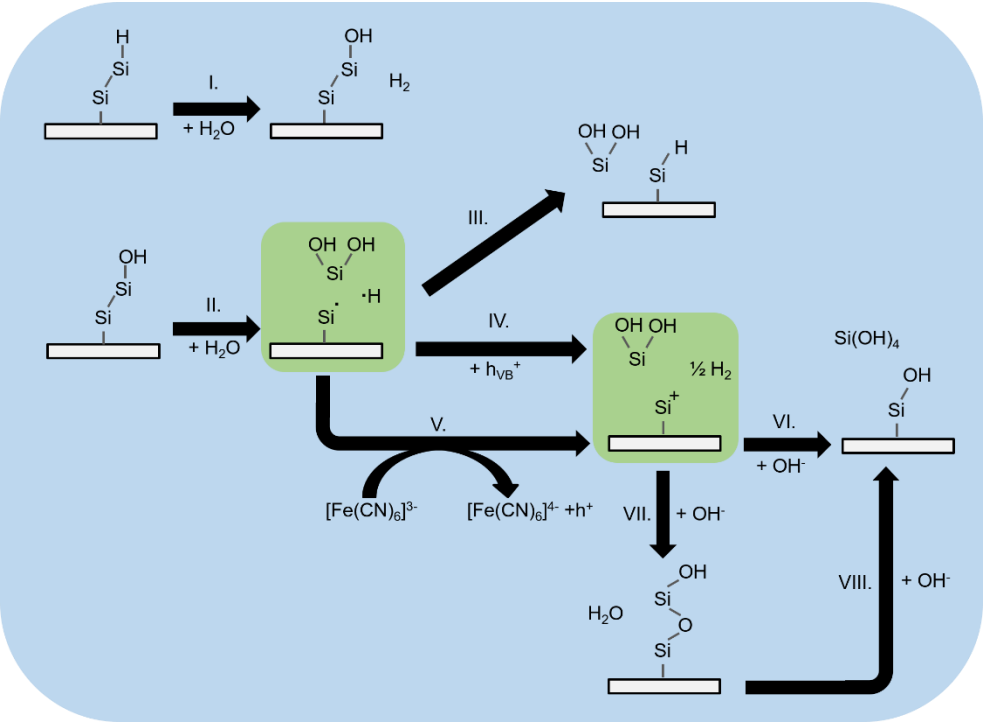

Scheme 2.1. Schematic for possible surface reactions of Si in alkaline electrolyte.[44] The reaction intermediates are found within the green boxes. In the dark at open circuit, the intermediate product from reaction II undergoes either reaction III in KOH or reaction V in KOH and $[Fe(CN)_6]^{3-}$. Under positive bias, this intermediate can undergo reaction IV. Holes from either reactions IV or V contribute to formation of oxide layer via reaction VII. The sample dissolution rate slows if reactions VIII or VI occur instead of reaction III.

Fig. 2.10 shows the etch rate of p^+-Si in 1.0 M KOH(aq) without or with varying concentrations of $[Fe(CN)_6]^{3-}$, as determined by measuring the height differences between a protected Si surface and a Si surface exposed to etching (See Scheme 2.2 for experimental details). During evaluation of the etch rate, the solution was not saturated with O_2. Si(111) is the slowest etching facet of Si, leading to exposed Si(111) facets determining the etch pit morphology of both Si(100) and Si(111) in KOH(aq) (Fig. 2.11).[47] Conversely, Si(100) etched in the protective electrolyte produced flat profiles with no facet dependence, indicating that the etching process was based on SiO_x formation and dissolution rather than

direct Si dissolution. The lack of a facet dependence moreover implies that SiO_x covered the entirety of the Si surface. Si electrode areas in the cm^2-scale (tested up to 0.88 cm^2) yielded < 2% differences in etch depth when sampling 15 random points on an electrode, underscoring the uniformity and scalability of the SiO_x growth and dissolution process. Fig. 2.10 and Table 2.2 compare the etch rates, R_{Si}, of various Si samples. In the protective electrolyte, Si(100) and Si(111) displayed etch rates of 1.8±0.1 and 1.7±0.1 nm h^{-1}, respectively, whereas in 1.0 M KOH(aq), Si(100) and Si(111) etched at 330±20 and 84±6 nm h^{-1}, respectively. Holding the Si at 1.63 V vs RHE in either the protective electrolyte or in 1.0 M KOH(aq) produced etch rates of 2.7±0.1 and 2.9±0.1 nm h^{-1}, respectively. Anodized Si oxide is more porous than thermal Si oxides or bulk silica, leading to more surface area exposed for chemical attack by the alkaline electrolyte.[48] The lower etch rates of Si in protective electrolyte at E_{oc} suggest that the oxide formed by the reduction of $[Fe(CN)_6]^{3-}$ could be comparatively more compact than the oxide in anodized films. The etch rate experiments presented in Fig. 2.10a further support the hypothesis that O_2 is not needed for $[Fe(CN)_6]^{3-}$ to oxidize the surface, because the etch rates were measured in the absence of bubbled O_2(g) and the electrode still displayed consistent and conformal oxidation of Si in the presence of $[Fe(CN)_6]^{3-}$.

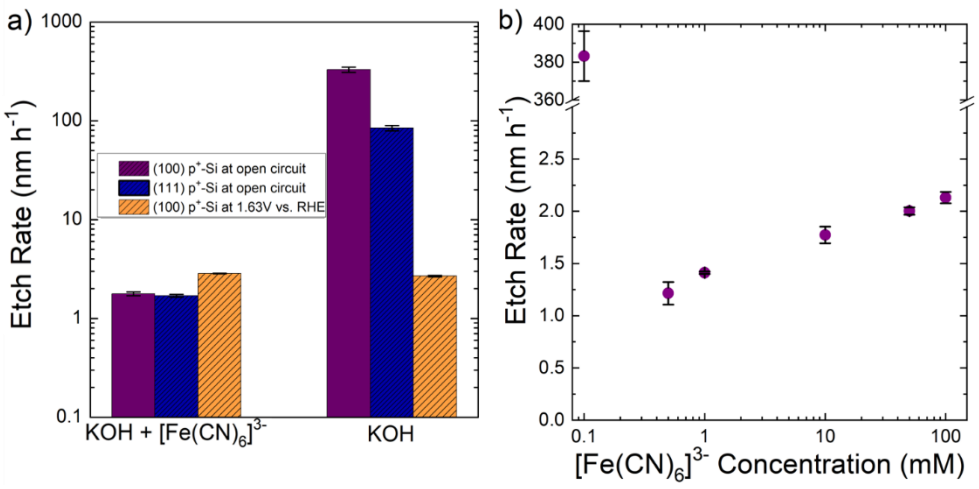

Figure 2.10. Influence of $[Fe(CN)_6]^{3-}$ on the etch rate of p^+-Si in 1.0 M KOH(aq). (a) Comparison of Si(100) at open circuit (purple), Si(111) at open circuit (blue), and Si(100) at 1.63 V vs RHE (orange) in either the protective electrolyte (10 mM $[Fe(CN)_6]^{3-}$, 1.0 M KOH(aq)) or in 1.0 M KOH(aq). (b) Dependence of the Si(100) etch rate on $[Fe(CN)_6]^{3-}$ concentration in 1.0 M KOH(aq) at open circuit.

Table 2.2. Etch rates of Si under various experimental conditions

$[Fe(CN)_6]^{3-}$ concentration (mM)	KOH concentration (M)	p^+-Si orientation	Potential (V vs. RHE)	Etch rate (nm h^{-1})
0	1.0	(100)	E_{oc}	330±20
0	1.0	(111)	E_{oc}	84±6
10	1.0	(100)	E_{oc}	1.8±0.1
10	1.0	(111)	E_{oc}	1.7±0.1
0	1.0	(100)	1.63	2.7±0.1
10	1.0	(100)	1.63	2.9±0.1
100	1.0	(100)	E_{oc}	2.1±0.1
50	1.0	(100)	E_{oc}	1.9±0.1
1	1.0	(100)	E_{oc}	1.4±0.1
0.5	1.0	(100)	E_{oc}	1.2±0.1
0.1	1.0	(100)	E_{oc}	380±20

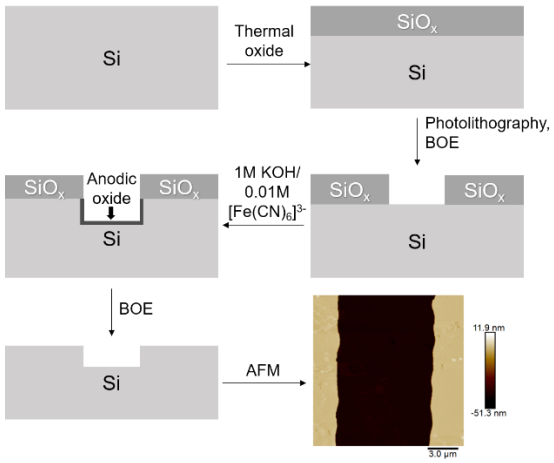

Scheme 2.2. Schematic of the experiment to determine the etch rate of the passivating oxide. The final step depicts a representative AFM image of a p^+-Si(100) surface after etching in 1.0 M KOH(aq) and 10 mM $[Fe(CN)_6]^{3-}$ for 24 h at open circuit.

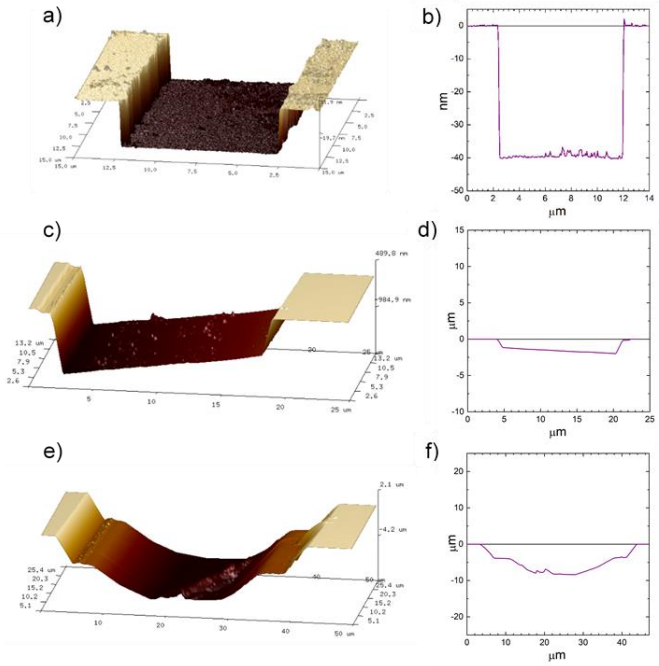

Figure 2.11. Topography of Si trenches after etching. (a-b) 3D profile of a Si(100) trench and corresponding cross sectional height profile after 24 h in 10 mM $[Fe(CN)_6]^{3-}$ and 1.0 M KOH(aq). (c-d) 3D profile of a Si(111) trench and height profile after 24 h in 1.0 M KOH(aq). The base of the etch pit is angled ~ 3˚ off the normal axis, suggesting that Si(111) is exposed when the miscut angle of the wafer is taken into account. (e-f) 3D profile of a Si(100) trench and height profile after 24 h in 1.0 M KOH(aq). The etch pit morphology is dependent on a combination of mask undercutting and exposure of the (111) facet. The top edge of the etch pit is angled at ~ 53˚, close to the expected angle between Si(111) and Si(100).

Fig. 2.10b shows a positive correlation between the etch rate of Si at E_{oc} in 1.0 M KOH(aq) and the concentration of $[Fe(CN)_6]^{3-}$, with 100 mM and 0.5 mM $[Fe(CN)_6]^{3-}$ having etch rates of 2.1±0.1 and 1.2±0.1 nm h^{-1}, respectively. However, mass transfer limitations likely occur at sufficiently low concentrations of $[Fe(CN)_6]^{3-}$ (< 0.5 mM), with Si dissolution outcompeting the $[Fe(CN)_6]^{3-}$ flux to the surface, leading to unhindered etching. Fig. 2.12 shows that p^+-Si(100) subjected to concentrations of $[Fe(CN)_6]^{3-}$ > 0.5 mM in 1.0 M KOH(aq) had surface roughness values (R_a) of ~ 0.2 nm that were essentially independent of the $[Fe(CN)_6]^{3-}$ concentration. p^+-Si(100) exposed to 0.5 mM $[Fe(CN)_6]^{3-}$ in 1.0 M KOH(aq) had R_a = 2.12 nm with no exposed Si(111) facets. The rougher surface morphology at 0.5 mM $[Fe(CN)_6]^{3-}$ concentration compared to higher oxidant concentrations could be a result of locally varying etch rates as a direct consequence of mass transfer limitations. Fig. 2.13 shows the Si 2p XPS data indicating mutually similar oxide compositions and oxidation states at various concentrations of oxidant, with the SiO_2/Si peak ratios being 0.29, 0.23, 0.24, or 0.30 for Si exposed to 1.0 M KOH(aq) and 0.5, 1.0, 10, or 100 mM $[Fe(CN)_6]^{3-}$, respectively. For concentrations between 1-100 mM $[Fe(CN)_6]^{3-}$ the SiO_2 content increased slightly for samples subjected to increasing $[Fe(CN)_6]^{3-}$ concentration, whereas at the 0.5 mM $[Fe(CN)_6]^{3-}$ threshold the SiO_2 content did not follow this trend due to the slightly higher surface area available for oxidation as a result of the rougher surface. Above the 0.5 mM threshold concentration of $[Fe(CN)_6]^{3-}$, the monotonically increasing etch rate with $[Fe(CN)_6]^{3-}$ concentration suggests that $[Fe(CN)]^{3-}$ could facilitate SiO_x dissolution during etching in addition to conformal oxidation of Si to SiO_x. Consequently, the lowest etch rate occurred around 0.5 mM $[Fe(CN)_6]^{3-}$, indicating a trade-off between having sufficient $[Fe(CN)_6]^{3-}$ to react with Si to

SiO_x and the presence of $[Fe(CN)_6]^{3-}$ facilitating dissolution of SiO_x. Although the 10 mM $[Fe(CN)_6]^{3-}$ used in stability tests (Fig. 2.1) was not the optimal concentration in terms of minimizing the SiO_x etch rate, it was sufficient to prevent the concentration from reaching the 0.5 mM threshold due to residual $[Fe(CN)_6]^{3-}$ photodegradation over the > 200 h run. The process by which $[Fe(CN)_6]^{3-}$ facilitates SiO_x dissolution requires further elucidation and does not affect the primary findings herein that a protective electrolyte can be utilized to protect Si photoanodes in KOH at open circuit, because the difference of a factor of < 2 in etch rate between 0.5 mM and 100 mM $[Fe(CN)_6]^{3-}$ is minor when compared to the Si etch rate in 1.0 M KOH(aq) without $[Fe(CN)_6]^{3-}$.

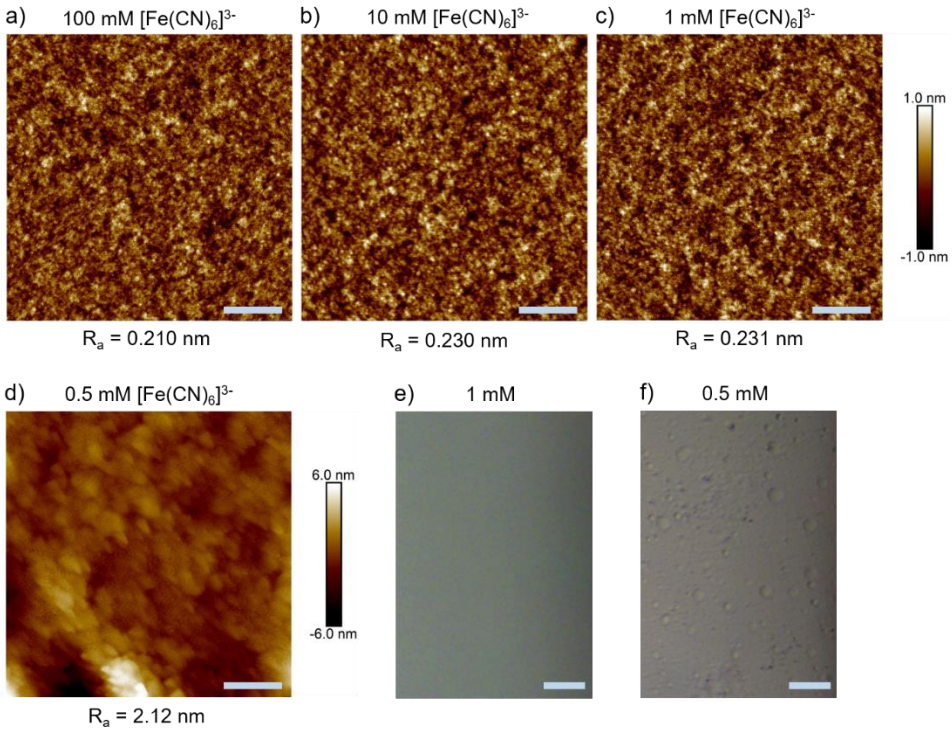

Figure 2.12. Atomic force microscope (a-d) and optical images (e-f) of p^+-Si(100) after 18 h at open circuit in 1.0 M KOH(aq) and (a) 100 mM, (b) 10 mM, (c,e) 1 mM, or (d,f) 0.5 mM $[Fe(CN)_6]^{3-}$. The surface roughness (R_a) was calculated sampling multiple scans at random points on 3 samples for each condition. The scale bar represents 200 nm for (a-d) and 20 μm for (e-f).

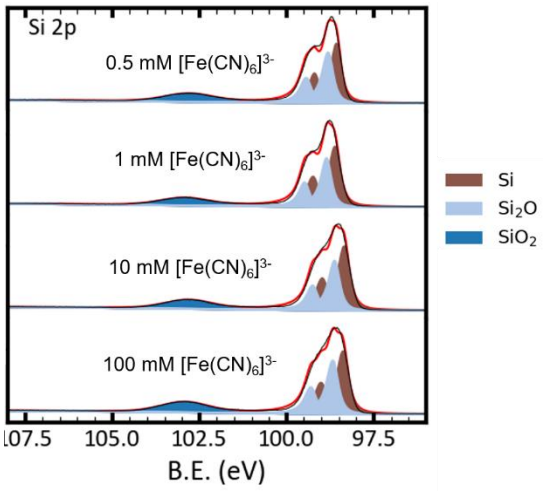

Figure 2.13. High-resolution XPS data in the Si 2p region of p^+-Si(100) after 18 h at open circuit in 1.0 M KOH(aq) and 0.5 mM, 1 mM, 10 mM, or 100 mM $[Fe(CN)_6]^{3-}$. The y-axis is in arbitrary units.

The presence of Ni on the Si surface could also impact the etch rate of SiO_x in the protective electrolyte. Based on the cross-sectional view of an etched np^+-Si/μNi electrode after 264 h (Fig. 2.5d) and assuming that the observed catalyst delamination occurred near the end of testing, the depth etched in the direction normal to the planar surface was 0.86±0.02 μm, corresponding to an etch rate of 3.3±0.1 nm h^{-1}. Similarly, the radial etching that led to undercutting of 2.83±0.05 μm diameter μNi corresponded to 1.03±0.08 μm of Si/SiO_x etched, or R_{Si} = 3.9±0.3 nm h^{-1}. Compared to a value of R_{Si} =1.8±0.1 nm h^{-1} for Si/SiO_x alone, these higher etch rates of Si/SiO_x in close proximity to μNi suggest that the Ni may assist in the Si/SiO_x etching process. The non-zero etch rate of the oxide in alkaline media will ultimately limit the stability of Si photoanodes even in the protective electrolyte, with the failure time depending on the exact thickness of the absorber, emitter layer (if any), and propensity of pitting corrosion to laterally undercut and delaminate the μNi electrocatalyst islands.

2.3.5 Faradaic Efficiency and Catalyst Activity in a Protective Electrolyte

Fig. 2.14 shows faradaic efficiency and OER activity of p^+-Si/(μ)Ni in 1.0 M KOH(aq) with and without $[Fe(CN)_6]^{3-}$. Illuminated Si/Ni photoanodes passivate in KOH at potentials relevant to OER,[42, 49] and consequently exhibit near unity faradaic efficiencies for O_2 production under illumination.[43] Hence the behavior of p^+-Si anodes in the dark was investigated to determine the effects of $[Fe(CN)_6]^{3-}$ on the dark electrode stability of Si and to confirm that the current density associated with oxidation of the trace amounts of $[Fe(CN)_6]^{4-}$ formed by oxidation of the Si to protect the electrode from dissolution in KOH(aq) did not substantially affect the faradaic efficiency for O_2 production. Prior to electrochemistry, electrodes were cycled at positive potentials in 1.0 M KOH(aq) to incorporate Fe impurities into the Ni precatalyst and form NiFeOOH.[9] Based on the amount of O_2(g) evolved and the charge passed at a constant 40 mA cm^{-2} current density, the p^+-Si/Ni film electrode exhibited > 97% faradaic efficiency (Fig. 2.14a) for the duration of the measurement regardless of the presence of $[Fe(CN)_6]^{3-}$ in solution. The p^+-Si/μNi anode similarly had > 96% faradaic efficiency when passing charge and measuring O_2 both after initial contact with the protective electrolyte and after resting for 45 h at open circuit, signifying that the oxidation of exposed Si was a negligible fraction of the overall charge passed. The near unity faradaic efficiency in 1.0 M KOH(aq) and in the protective electrolyte can be understood by the order of magnitude for the current associated with either anodic passivation or $[Fe(CN)_6]^{3-}$. For an etch rate of 2.7 nm h^{-1} of an anodic oxide in protective electrolyte, ~ 1.3 μA cm^{-2} (See Section 2.5 for calculations) is expected from oxidation of Si, comprising ~ 0.003% of the total current passed in this experiment. Oxidation of Si in the dark at open circuit similarly leads to a small rate of reduction of

$[Fe(CN)_6]^{3-}$, of $8.8x10^{-12}$ mol s^{-1} cm^{-2} compared to $7.8x10^{-8}$ mol s^{-1} cm^{-2} of O_2(g) generated assuming 30 mA cm^{-2} of photocurrent. Consequently, the moles of $[Fe(CN)_6]^{4-}$ produced in 88 h in the dark would produce ~ 1% of the moles of O_2(g) generated in 1 h under illumination. The oxidation of $[Fe(CN)_6]^{4-}$ back to $[Fe(CN)_6]^{3-}$ under potential control would thus be negligibly small compared to the current associated with the OER, consistent with the measured faradaic efficiency found in Fig. 2.14a.

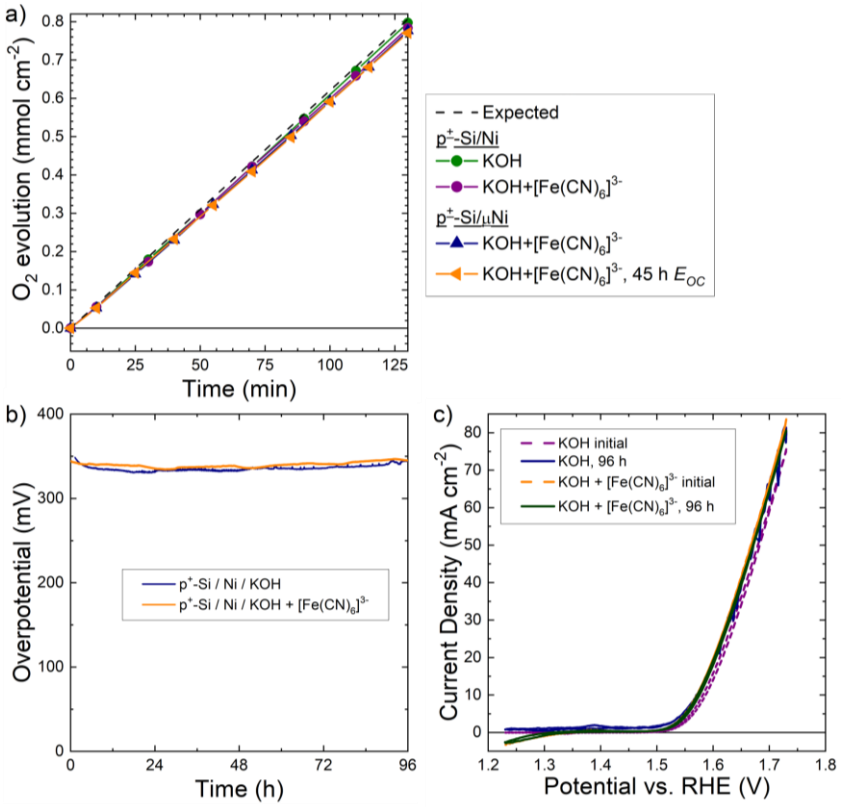

Figure 2.14. Catalytic performance of p^+-Si/(μ)Ni electrodes for the OER in 1.0 M KOH(aq) with or without 10 mM ferricyanide. (a) Faradaic efficiency measurements via an eudiometer for p^+-Si/μNi (triangle) and p^+-Si/Ni film (circle) electrodes held galvanostatically at 40 mA cm^{-2}. Charge passed and O_2 measurement began after the electrodes were in contact with the solution and were repeated for the p^+-Si/μNi electrode after resting at open circuit (E_{OC}) for an additional 45 h. (b) Chronopotentiometry at 10 mA cm^{-2} of a p^+-Si/Ni film electrode in KOH(aq) (blue) or in $[Fe(CN)_6]^{3-}$, KOH(aq) (orange). (c) Cyclic voltammetry at 10 mV s^{-1} before and after chronopotentiometry. The p^+-Si/Ni film electrodes were prepared by depositing 100 nm of Ni onto p^+-Si and activating the electrodes in 1.0 M KOH(aq) with 20 cycles between 0.53 V and 1.83 V vs RHE at 40 mV s^{-1}, to incorporate Fe impurities from the electrolyte and to form NiFeOOH.[9]

In contrast to cycling between light with positive bias and dark at open circuit in Fig. 2.1 and 2.5, the activated p^+-Si/Ni electrode in Fig. 2.14b was galvanostatically held at 10 mA cm^{-2} continuously for 96 h. Under continuous operation, any exposed Si forms an oxide layer due to the applied positive bias.[26] The electrode exhibited stable overpotentials for > 96 h in both 1.0 M KOH(aq) and in the protective electrolyte, with nearly identical average overpotentials of 336±4 and 340±4 mV, respectively (Fig. 2.14b). As expected for a one-electron redox species, $[Fe(CN)_6]^{3-}$ did not catalyze the four-hole oxidation of water to O_2(g), as evidenced by the mutually similar overpotentials of both systems. Cyclic voltammetric measurements (Fig. 2.14c) before and after galvanostatic control, respectively, indicated that the electrodes did not exhibit any appreciable change in resistance. These results suggest that $[Fe(CN)_6]^{3-}$ minimally affected the faradaic efficiency towards OER or the electrocatalytic behavior of the NiFeOOH catalyst.

2.3.6 Stability of $[Fe(CN)_6]^{3-}$ as a protective electrolyte

The concentrations of $[Fe(CN)_6]^{3-}$ and $[Fe(CN)_6]^{4-}$ were monitored using UV-vis spectroscopy through a correlation between the 420 nm and 260 nm absorption peaks.[38] Fig. 2.15 shows the spectra for solutions of 1 mM $[Fe(CN)_6]^{3-}$ and 0.1 M KOH(aq) in the dark (Fig. 2.15a) or under illumination with either a red (627 nm) LED (Fig. 2.15b) or an ELH-type W-halogen lamp with a 400 nm long pass filter (Fig. 2.15c). $[Fe(CN)_6]^{3-}$ decomposes under UV-light,[50] so a UV long pass filter was used to minimize this decomposition process. Nevertheless, the solution absorbs strongly below 480 nm, lowering the $[Fe(CN)_6]^{3-}$ concentration from 1.0 mM to 0.09 mM over 120 h when subjected to visible light (Fig. 2.15d). This decrease in concentration can be accounted for

by the light-driven decomposition to Fe_2O_3 as well as reduction to $[Fe(CN)_6]^{4-}$, whose concentration increased from ~ 0 mM to 0.66 mM within the same timeframe.[51] Fe_2O_3 was observed as a red-orange colored precipitate that was verified to be Fe_2O_3 by XPS (Fig. 2.16). Under dark conditions or red LED illumination, the $[Fe(CN)_6]^{3-}$ remained stable in KOH(aq) > 120 h without any notable decrease in the absorption peaks corresponding to $[Fe(CN)_6]^{3-}$, and no precipitate was observed after the solution was centrifuged.

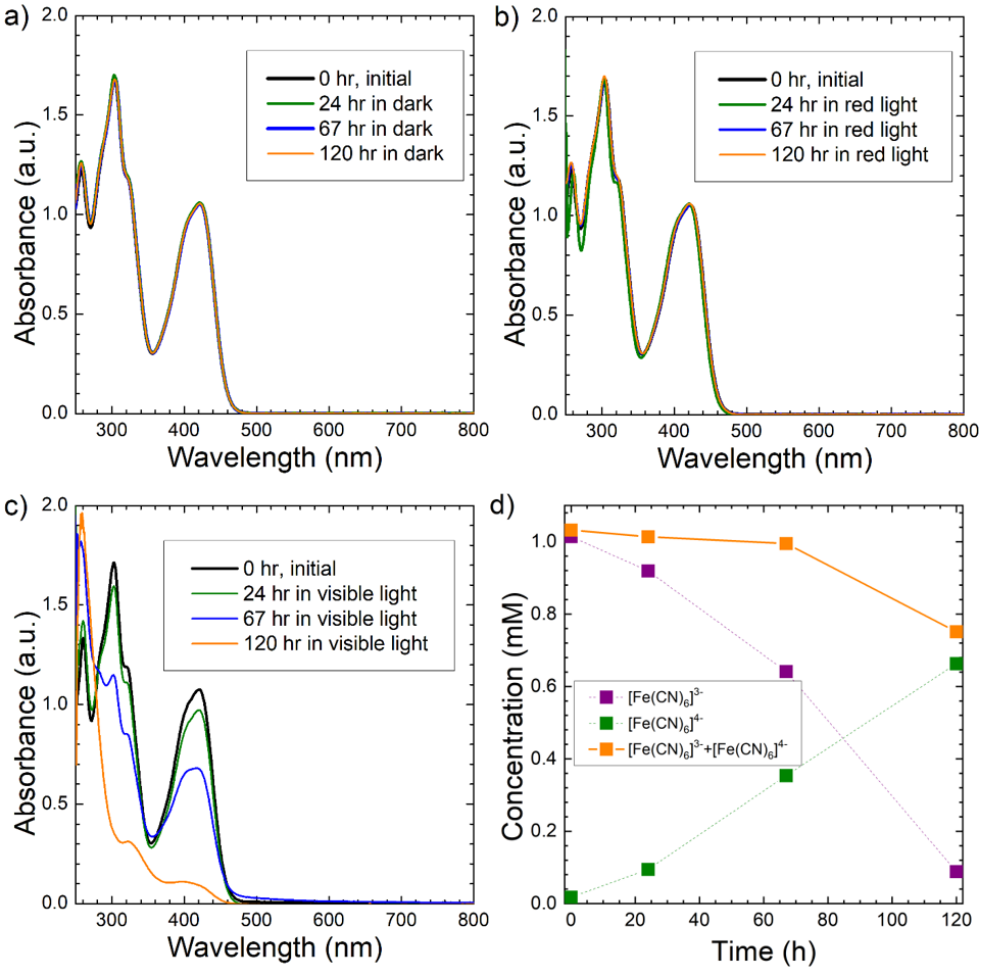

Figure 2.15. [$Fe(CN)_6]^{3-/4-}$ UV-vis spectra and concentrations under different illumination conditions. UV-vis spectra of 1 mM $[Fe(CN)_6]^{3-}$ in 0.1 M KOH(aq) at 0, 24, 67, and 120 h under (a) dark, (b) 627 nm LED, and (c) ELH lamp illumination with a 400 nm long pass filter. (d) $[Fe(CN)_6]^{3-/4-}$ concentrations under visible light obtained from fitting the 420 nm and 260 nm peaks in (c).

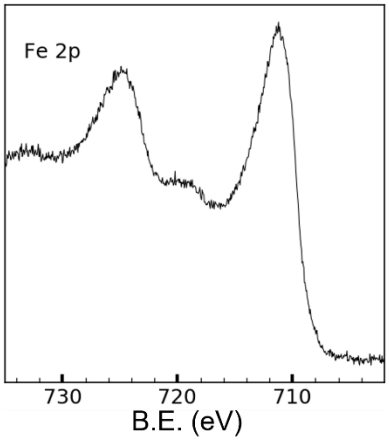

Figure 2.16. High-resolution XPS data in the Fe 2p region of the precipitate produced by shining visible light on 10 mM $[Fe(CN)_6]^{3-}$ in 1.0 M KOH(aq). The y-axis is in arbitrary units.

Fig. 2.17a shows a chronoamperometric stability run for an np^+-Si(100)/μNi electrode in 1.0 M KOH(aq) and 10 mM $[Fe(CN)_6]^{3-}$ that was subjected to 100 mW cm^{-2} illumination from a Xe arc lamp with an AM 1.5 filter during the day cycles. In contrast to Fig. 2.1a, no UV filter was placed between the electrode and light source, leading to accelerated decomposition of $[Fe(CN)_6]^{3-}$. At the end of each 24 h day/night cycle, the electrolyte was replaced with fresh electrolyte to ensure the presence of sufficient $[Fe(CN)_6]^{3-}$ to oxidize Si at open circuit. The temporary drops in photocurrent each day was consistently attributed to parasitic absorption by the Fe_2O_3 precipitate that formed and was dispersed within the solution, whereas later erratic behavior is likely due to adsorption and desorption of precipitate on the electrode surface. Fig. 2.17b shows that although the light limiting current was mostly stable after the electrolyte was replaced and a majority of the Fe_2O_3 was removed (but not all) after each day, more pronounced changes to the onset potential (~ +100 mV) and fill factor (from 0.37 to 0.16) were observed relative to an electrochemical cell that was not subjected to UV light (Fig. 2.1b). The negligible dark

current in Fig. 2.17b suggests that the bare Si was not corroding rapidly throughout the stability test. Fig. 2.18 shows that the increasing electrode resistance can be attributed to accelerated delamination of μNi throughout most of the electrode compared to Fig. 2.5c. The μNi located near the edges of the electrode remained mostly intact (Fig. 2.18b). The electrode behavior could thus be attributed to the accumulation of dispersed Fe_2O_3 precipitate, which acted as an abrasive that facilitated mechanical delamination of μNi of the exposed electrode surface. In contrast, μNi near the electrode edges was protected by the surrounding epoxy that protruded over the surface. Since the eventual failure that the electrode experienced is mechanical, rather than photochemical, there is no evidence of wavelength-dependent corrosion due to hot holes at the current density tested for Si in alkaline media. Other reports have also used solar simulators with AM 1.5 filters and have shown that n-Si/Ni nanoparticle photoanodes are stable and do not exhibit Si photocorrosion under these conditions.[42, 43]

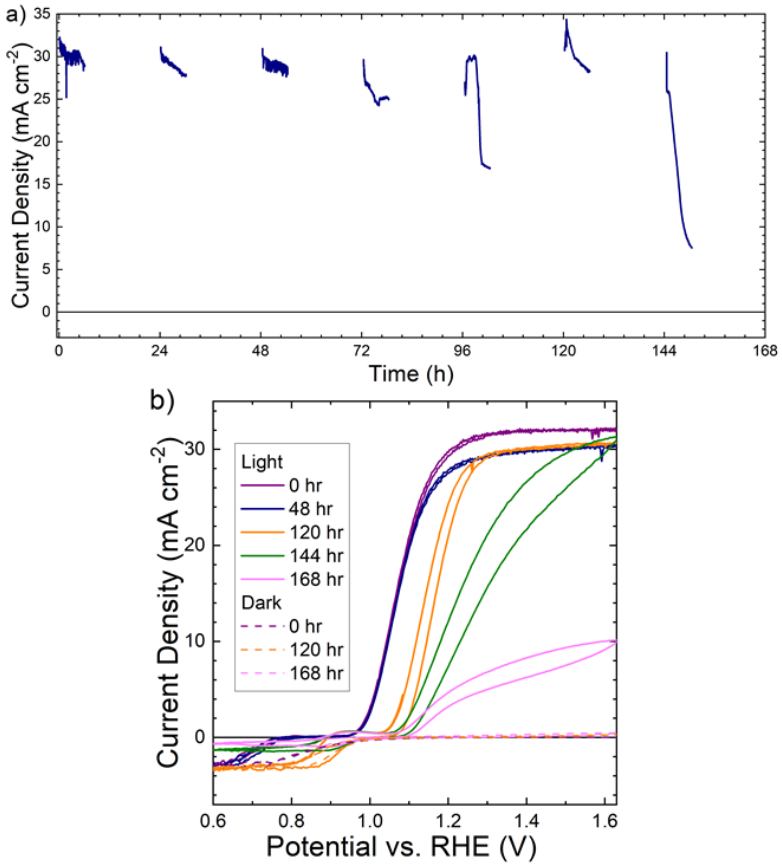

Figure 2.17. Stability and performance of an np^+-Si(100)/µNi electrode in 1.0 M KOH(aq) and 10 mM $[Fe(CN)_6]^{3-}$ with 100 mW cm^{-2} of illumination provided by a Xe arc lamp with an AM 1.5 filter. (a) Chronoamperometric data were taken in 6 h intervals at 1.63 V vs RHE under illumination, followed by 18 h in the dark at open circuit. The electrolyte was replaced and O_2(g) was bubbled for ~ 5 min at the end of each 24 h period. (b) Current density vs potential behavior at a scan rate of 40 mV s^{-1} under illumination (solid lines) and in the dark (dashed lines).

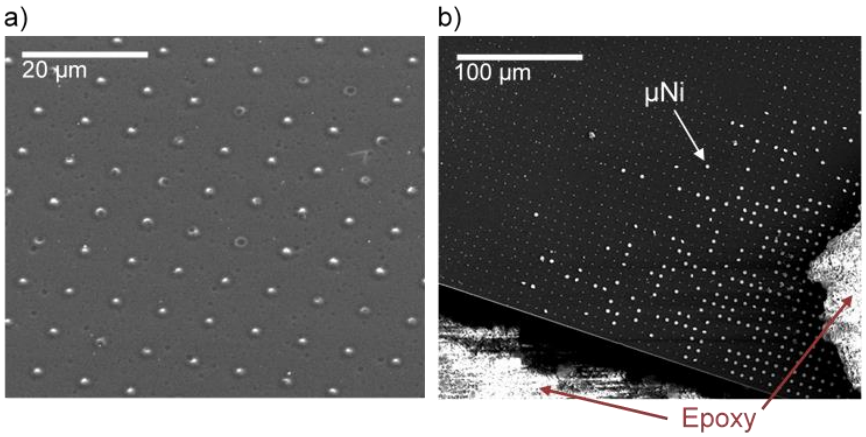

Figure 2.18. Scanning-electron micrographs of np^+-Si(100)/µNi electrodes after testing for 169 h. (a) Center of the electrode where µNi was predominantly delaminated. (b) The corner of the electrode surrounded by epoxy, where µNi was mostly intact.

$[Fe(CN)_6]^{3-}$ is stable under red light and absorbs light only under ~ 480 nm, so managing the wavelength range of light entering the anolyte compartment serves to both stabilize the $[Fe(CN)_6]^{3-}$ and minimize its parasitic absorption when under illumination. Although filtering all light absorbed by $[Fe(CN)_6]^{3-}$ is one way to stabilize this species, such an approach is undesirable in practice because large portions of the solar spectrum would not be utilized, hindering the amount of photocurrent that could be obtained. Achieving stable operation with $[Fe(CN)_6]^{3-}$ in sunlight is realizable in a tandem cell configuration with incident light going through the catholyte followed sequentially by light going through the anolyte. The small band gap of Si precludes the semiconductor alone from achieving the ~ 1.7 V necessary to spontaneously split water,[52] so integrated tandem devices with a wide band gap semiconductor as the top cell and Si as the bottom cell have been proposed.[2, 3, 35] In an optimally configured tandem cell, each half-cell absorbs half of incoming photons with higher energy photons being more readily absorbed by the top, wider band gap semiconductor. One proposed device architecture that satisfies this configuration uses semiconductor nano- and microwire arrays embedded in a membrane, which maximizes high-energy photons collected by the top cell and minimizes the path length of low energy photons in the anolyte.[53, 54] Lower energy photons that pass through the catholyte can be harvested by the Si bottom cell, subsequently minimizing any parasitic absorption caused by the $[Fe(CN)_6]^{3-}$.

2.4 Conclusions

The studies conducted herein emphasize the importance of active redox species at the semiconductor/electrolyte interface for the development of stable photoelectrodes. The

prevailing strategy for stabilizing electrodes in corrosive electrolytes has involved coatings that are impermeable to electrolytes but allow light and photogenerated charge to be transmitted. This strategy has resulted in a substantial improvement in photoelectrode stability, particularly for Si photoanodes. However, protected photoanodes often contain defects on the metal oxide film (pinholes) that allow the electrolyte to react with the photoelectrode, leading to eventual device failure.[18, 29, 55] The work presented herein demonstrates that a protective electrolyte is conceptually different than a protective film, and allows the photoelectrode to be protected when exposed to a corrosive electrolyte. Protective electrolytes can be utilized in conjunction with protective coatings and subsequently allow for increased tolerance to physical defects in protective films, constituting an attractive property for device systems that need to be scalable.

The protective electrolyte self-healing strategy can be generalized to other oxidizing agents that have a potential that allows for spontaneous reaction with the photoelectrode to form a passivating layer. The oxidizing agents must be stable in the electrolyte, should have minimal parasitic light absorption, and must have fast kinetics for both oxidation and reduction. For Si photoanodes, oxidizing agents like MnO_4^- and CrO_4^{2-} may be considered, however they have been shown to adsorb onto SiO_x and hinder oxide growth, leading to higher oxide dissolution rates.[44] Furthermore, MnO_4^- absorbs strongly in the visible range whereas CrO_4^{2-} is a carcinogen, posing a potential health risk when considering scaled-up systems.[44, 56] Although O_2 is colorless, non-toxic, and abundant from both ambient air and as an evolved product of water splitting, the slow kinetics for O_2 reduction prevent it from being an adequate redox species for a protective electrolyte.

In summary, addition of $[Fe(CN)_6]^{3-}$ to 1.0 M KOH(aq) extends the lifetime of Si photoanodes patterned with Ni catalyst islands to ≥ 288 h under simulated day/night cycles, equivalent to 12 days of operation. The Si surface was oxidized by a SiO_x layer formed via either by anodic current supplied from photogenerated holes or by $[Fe(CN)_6]^{3-}$. The presence of $[Fe(CN)_6]^{3-}$ did not hinder the catalytic activity of NiFeOOH or the faradaic efficiency for the OER. In the protective electrolyte, the Si(100) etch rate was > 180 times slower, and independent of the facet, compared to the behavior in 1.0 M KOH(aq) alone. These findings show that the spontaneous passivation of exposed Si that allows for long (> 100 h) device lifetimes under conditions for OER can also be achieved in the dark at open circuit, marking an important step towards operation of Si photoanodes under realistic varying insolation conditions. Protective electrolytes like $[Fe(CN)_6]^{3-}$ that enable self-healing of photoelectrodes could be utilized in conjunction with protective layers to further extend device lifetimes.

2.5 Supplemental Calculations

We additionally evaluated the behavior in the dark to directly compare water oxidation to oxidation of residual $[Fe(CN)_6]^{4-}$. The amount of charge passed over time (in C h^{-1}) was estimated as follows. We assumed that the electrode area was 0.62 cm^2, that SiO_x equates to SiO_2 (ρ = 2.65 g cm^{-3}) for this estimate, and that the rate of charge passed was proportional to the etching of an anodic oxide in 1.0 M KOH(aq) and 10 mM $[Fe(CN)_6]^{3-}$ (2.7×10^{-7} cm h^{-1}).

$$Current = \left(\left(2.7 * 10^{-7} \frac{cm}{h}\right) * \left(3600 \frac{sec}{h}\right) \left(\frac{2.65 \frac{g\ SiO_2}{cm^3}}{60.08 \frac{g\ SiO_2}{mol}} * 6.022 * 10^{23}\ mol^{-1} \right) \right.$$

$$\left. * \left(4e^- * 1.602 * 10^{-19} \frac{C}{e^-}\right) \right) = \mathbf{1.3 * 10^{-6}} \frac{\boldsymbol{A}}{\boldsymbol{cm^2}}$$

Analogously, for an etch rate of $1.8*10^{-7}$ cm h^{-1}, the current density is 0.85 µA cm^{-2} and the rate of $[Fe(CN)_6]^{3-}$ consumed in the dark was estimated as follows:

$$[Fe(CN)_6]^{3-}\ consumed = \left(\frac{0.85 * 10^{-6} \frac{C}{s\ cm^2}}{1.602 * 10^{-19} \frac{C}{e^-}} \right) * \left(\frac{1\ [Fe(CN)_6]^{3-}}{1\ e^-} \right) * \left(\frac{1\ mol\ [Fe(CN)_6]^{3-}}{6.022 * 10^{23}\ [Fe(CN)_6]^{3-}} \right)$$

$$= \mathbf{8.8 * 10^{-12}} \frac{\boldsymbol{mol}}{\boldsymbol{s\ cm^2}}$$

Assuming that the ~30 mA cm^{-2} of photocurrent density observed in Fig. 2.1 contributes solely to O_2 evolution, the rate of O_2 generated was estimated as follows:

$$O_2(g)\ generated = \left(\frac{0.030 \frac{C}{s\ cm^2}}{1.602 * 10^{-19} \frac{C}{e^-}} \right) * \left(\frac{1\ O_2}{4\ e^-} \right) * \left(\frac{1\ mol\ O_2}{6.022 * 10^{23}\ O_2} \right) = \mathbf{7.8 * 10^{-8}} \frac{\boldsymbol{mol}}{\boldsymbol{s\ cm^2}}$$

$$O_2 : [Fe(CN)_6]^{4-} ratio = \left(\frac{7.8 * 10^{-8} \frac{mol\ O_2}{s\ cm^2}}{8.8 * 10^{-12}\ \frac{mol\ [Fe(CN)_6]^{3-}}{s\ cm^2}} \right) * \left(\frac{1\ mol\ [Fe(CN)_6]^{3-} consumed}{1\ mol\ [Fe(CN)_6]^{4-} generated} \right)$$

$$= \mathbf{8.8 * 10^{3}}$$

To assess the impact of $[Fe(CN)_6]^{4-}$ oxidation on Faradaic efficiency, the ratio of $[Fe(CN)_6]^{4-}$ generated in the dark and O_2 produced under illumination is described as follows:

Thus 88 h of $[Fe(CN)_6]^{4-}$ generation in the dark would be required to produce 1% of the amount of O_2(g) generated in 1 h under illumination. Assuming no other substantial source of $[Fe(CN)_6]^{4-}$, the impact of $[Fe(CN)_6]^{4-}$ is therefore expected to minimally impact

the efficiency. This estimate supports the observed Faradaic efficiency displayed in Fig. 2.14b.

2.6 References

1. N. S. Lewis, *Science*, 2016, **351**, aad1920.
2. S. Hu, C. Xiang, S. Haussener, A. D. Berger and N. S. Lewis, *Energy & Environmental Science*, 2013, **6**, 2984-2993.
3. M. R. Shaner, K. T. Fountaine, S. Ardo, R. H. Coridan, H. A. Atwater and N. S. Lewis, *Energy & Environmental Science*, 2014, **7**, 779-790.
4. A. G. Aberle, S. Glunz and W. Warta, *Journal of Applied Physics*, 1992, **71**, 4422-4431.
5. K. Sun, X. Pang, S. Shen, X. Qian, J. S. Cheung and D. Wang, *Nano Letters*, 2013, **13**, 2064-2072.
6. M. J. Kenney, M. Gong, Y. Li, J. Z. Wu, J. Feng, M. Lanza and H. Dai, *Science*, 2013, **342**, 836-840.
7. P. Xu, J. Feng, T. Fang, X. Zhao, Z. Li and Z. Zou, *RSC Advances*, 2016, **6**, 9905-9910.
8. C. C. L. McCrory, S. Jung, J. C. Peters and T. F. Jaramillo, *Journal of the American Chemical Society*, 2013, **135**, 16977-16987.
9. L. Trotochaud, S. L. Young, J. K. Ranney and S. W. Boettcher, *Journal of the American Chemical Society*, 2014, **136**, 6744-6753.
10. B. S. Yeo and A. T. Bell, *Journal of the American Chemical Society*, 2011, **133**, 5587-5593.
11. D. A. Corrigan and R. M. Bendert, *Journal of The Electrochemical Society*, 1989, **136**, 723-728.
12. S. Hu, M. R. Shaner, J. A. Beardslee, M. Lichterman, B. S. Brunschwig and N. S. Lewis, *Science*, 2014, **344**, 1005-1009.
13. I. A. Moreno-Hernandez, B. S. Brunschwig and N. S. Lewis, *Advanced Energy Materials*, 2018, **8**, 1801155.
14. K. Sun, F. H. Saadi, M. F. Lichterman, W. G. Hale, H. P. Wang, X. Zhou, N. T. Plymale, S. T. Omelchenko, J. H. He, K. M. Papadantonakis, B. S. Brunschwig and N. S. Lewis, *Proc Natl Acad Sci U S A*, 2015, **112**, 3612-3617.
15. X. Zhou, R. Liu, K. Sun, K. M. Papadantonakis, B. S. Brunschwig and N. S. Lewis, *Energy & Environmental Science*, 2016, **9**, 892-897.
16. Y. W. Chen, J. D. Prange, S. Dühnen, Y. Park, M. Gunji, C. E. D. Chidsey and P. C. McIntyre, *Nature Materials*, 2011, **10**, 539.
17. N. C. Strandwitz, D. J. Comstock, R. L. Grimm, A. C. Nichols-Nielander, J. Elam and N. S. Lewis, *The Journal of Physical Chemistry C*, 2013, **117**, 4931-4936.
18. D. Bae, B. Seger, P. C. Vesborg, O. Hansen and I. Chorkendorff, *Chem Soc Rev*, 2017, **46**, 1933-1954.

19. B. Mei, A. A. Permyakova, R. Frydendal, D. Bae, T. Pedersen, P. Malacrida, O. Hansen, I. E. L. Stephens, P. C. K. Vesborg, B. Seger and I. Chorkendorff, *The Journal of Physical Chemistry Letters*, 2014, **5**, 3456-3461.
20. D. Bae, B. Mei, R. Frydendal, T. Pedersen, B. Seger, O. Hansen, P. C. K. Vesborg and I. Chorkendorff, *ChemElectroChem*, 2016, **3**, 1546-1552.
21. R. Liu, Z. Zheng, J. Spurgeon and X. Yang, *Energy & Environmental Science*, 2014, **7**, 2504-2517.
22. P. Nunez, M. H. Richter, B. D. Piercy, C. W. Roske, M. Cabán-Acevedo, M. D. Losego, S. J. Konezny, D. J. Fermin, S. Hu, B. S. Brunschwig and N. S. Lewis, *The Journal of Physical Chemistry C*, 2019, **123**, 20116-20129.
23. D. Bae, S. Shayestehaminzadeh, E. Thorsteinsson, T. Pedersen, O. Hansen, B. Seger, P. Vesborg, S. Olafsson and I. Chorkendorff, *Solar Energy Materials and Solar Cells*, 2016, **144**, 758–765.
24. R. L. Smith, B. Kloeck and S. D. Collins, *Journal of The Electrochemical Society*, 1988, **135**, 2001-2008.
25. E. D. Palik, J. W. Faust, H. F. Gray and R. F. Greene, *Journal of The Electrochemical Society*, 1982, **129**, 2051-2059.
26. K. Sun, Nicole L. Ritzert, J. John, H. Tan, W. G. Hale, J. Jiang, I. Moreno-Hernandez, K. M. Papadantonakis, T. P. Moffat, B. S. Brunschwig and N. S. Lewis, *Sustainable Energy & Fuels*, 2018, **2**, 983-998.
27. M. R. Shaner, S. Hu, K. Sun and N. S. Lewis, *Energy & Environmental Science*, 2015, **8**, 203-207.
28. X. Zhou, R. Liu, K. Sun, D. Friedrich, M. T. McDowell, F. Yang, S. T. Omelchenko, F. H. Saadi, A. C. Nielander, S. Yalamanchili, K. M. Papadantonakis, B. S. Brunschwig and N. S. Lewis, *Energy & Environmental Science*, 2015, **8**, 2644-2649.
29. K. Sun, M. T. McDowell, A. C. Nielander, S. Hu, M. R. Shaner, F. Yang, B. S. Brunschwig and N. S. Lewis, *The Journal of Physical Chemistry Letters*, 2015, **6**, 592-598.
30. K. Oh, C. Mériadec, B. Lassalle-Kaiser, V. Dorcet, B. Fabre, S. Ababou-Girard, L. Joanny, F. Gouttefangeas and G. Loget, *Energy & Environmental Science*, 2018, **11**, 2590-2599.
31. D. K. Lee and K.-S. Choi, *Nature Energy*, 2017, **3**, 53-60.
32. P. M. M. C. Bressers, J. J. Kelly, J. G. E. Gardeniers and M. Elwenspoek, *Journal of The Electrochemical Society*, 1996, **143**, 1744-1750.
33. P. M. M. C. Bressers, S. A. S. P. Pagano and J. J. Kelly, *Journal of Electroanalytical Chemistry*, 1995, **391**, 159-168.
34. M. G. Walter, E. L. Warren, J. R. McKone, S. W. Boettcher, Q. Mi, E. A. Santori and N. S. Lewis, *Chemical Reviews*, 2010, **110**, 6446-6473.
35. Y. Chen, S. Hu, C. Xiang and N. S. Lewis, *Energy & Environmental Science*, 2015, **8**, 876-886.
36. P. K. Nayak, J. Bisquert and D. Cahen, *Advanced Materials*, 2011, **23**, 2870-2876.
37. I. A. Moreno-Hernandez, S. Yalamanchili, H. J. Fu, H. A. Atwater, B. S. Brunschwig and N. S. Lewis, *Journal of Materials Chemistry A*, 2020, **8**, 9292-9301.

38. M. Chakrabarti and E. Roberts, *Journal of the Chemical Society of Pakistan*, 2008, **30**, 817-823.
39. R. Alfonsetti, L. Lozzi, M. Passacantando, P. Picozzi and S. Santucci, *Applied Surface Science*, 1993, **70-71**, 222-225.
40. Y. Chen, K. Sun, H. Audesirk, C. Xiang and N. S. Lewis, *Energy & Environmental Science*, 2015, **8**, 1736-1747.
41. J. Lin and W. G. Breck, *Canadian Journal of Chemistry*, 1965, **43**, 766-771.
42. G. Loget, B. Fabre, S. Fryars, C. Mériadec and S. Ababou-Girard, *ACS Energy Letters*, 2017, **2**, 569-573.
43. S. A. Lee, T. H. Lee, C. Kim, M. G. Lee, M.-J. Choi, H. Park, S. Choi, J. Oh and H. W. Jang, *ACS Catalysis*, 2018, **8**, 7261-7269.
44. X. H. Xia and J. J. Kelly, *Electrochimica Acta*, 2000, **45**, 4645-4653.
45. P. Allongue, V. Costa-Kieling and H. Gerischer, *Journal of The Electrochemical Society*, 1993, **140**, 1018.
46. H. Seidel, L. Csepregi, A. Heuberger and H. Baumgartel, *Journal of The Electrochemical Society*, 1990, **137**, 3612.
47. K. Sato, M. Shikida, Y. Matsushima, T. Yamashiro, K. Asaumi, Y. Iriye and M. Yamamoto, *Sensors and Actuators A: Physical*, 1998, **64**, 87-93.
48. W. A. Pliskin and H. S. Lehman, *Journal of The Electrochemical Society*, 1965, **112**, 1013-1019.
49. G. Xu, Z. Xu, Z. Shi, L. Pei, S. Yan, Z. Gu and Z. Zou, *ChemSusChem*, 2017, **10**, 2897-2903.
50. S. Ašpergěr, *Transactions of the Faraday Society*, 1952, **48**, 617-624.
51. C. A. P. Arellano and S. S. Martínez, *Solar Energy Materials and Solar Cells*, 2010, **94**, 327-332.
52. S. Haussener, C. Xiang, J. M. Spurgeon, S. Ardo, N. S. Lewis and A. Z. Weber, *Energy & Environmental Science*, 2012, **5**, 9922-9935.
53. E. L. Warren, H. A. Atwater and N. S. Lewis, *The Journal of Physical Chemistry C*, 2013, **118**, 747-759.
54. J. M. Spurgeon, M. G. Walter, J. Zhou, P. A. Kohl and N. S. Lewis, *Energy & Environmental Science*, 2011, **4**, 1772-1780.
55. E. Verlage, S. Hu, R. Liu, R. J. R. Jones, K. Sun, C. Xiang, N. S. Lewis and H. A. Atwater, *Energy & Environmental Science*, 2015, **8**, 3166-3172.
56. M. Costa and C. B. Klein, *Critical Reviews in Toxicology*, 2006, **36**, 155-163.

Chapter 3

CATALYTIC, OPEN-CIRCUIT SILICON PASSIVATION BY THIN METAL OXIDE FILMS IN AQUEOUS ALKALINE ELECTROLYTES

3.1 Introduction

Small band gap photoanodes used for water oxidation under illumination are thermodynamically unstable in strongly alkaline or acidic solution.[1, 2] However, protective coatings such as amorphous TiO_2, Ni, NiO_x, and CoO_x have extended the operational lifetime of a variety of such photoanodes including Si, GaAs, GaP, CdTe, and $BiVO_4$ for the light-driven oxygen-evolution reaction (OER) in strongly alkaline electrolytes.[3-8] Nonetheless, pinholes and other defects in the protective films can facilitate corrosion of exposed regions of the semiconductor and lead to eventual device failure.[9, 10] Common failure modes of unprotected regions are the formation of an insulating interfacial layer, generally an oxide, or corrosion that leads to pit formation that can spread through the entire photoelectrode material.

During O_2 evolution, bare Si photoanodes grow an oxide (SiO_x) passivation layer that resists corrosion and are thus resilient to pinholes in the protection layer.[11, 12] In the dark at open circuit, however, when the electrode is poised at the rest potential, the SiO_x slowly dissolves in alkaline media, in which Si itself rapidly etches. This process can lead to electrode failure under day/night cycling conditions.[6, 13, 14]

The etch rate of SiO_x is orders of magnitude slower than that of Si in alkaline solution, so the dissolution of Si in the absence of illumination can in principle be inhibited if the oxide layer can be maintained on the Si surface.[15, 16] Kinetic passivation of the Si

thus occurs when the growth rate of SiO_x exceeds its rate of dissolution. The addition of $[Fe(CN)_6]^{3-}$ to a strongly alkaline solution has been shown to limit the degradation of a Si photoanode decorated with an array of Ni islands.[17] The $[Fe(CN)_6]^{3-}$ (E^0 ~ 0.36 V vs the normal hydrogen electrode, NHE, for $[Fe(CN)_6]^{3-/4-}$)[18] sets the surface potential of the Si to be ~ 1.4 V vs the reversible hydrogen electrode (RHE) in 1 M KOH(aq), driving the formation of oxide on exposed regions of the Si surface. Consequently, regions of the Si that are exposed to the electrolyte between the Ni islands, or even under a porous Ni oxy-hydroxy film, are inhibited from corrosion and dissolution due to the formation of the protective, passivating oxide (Scheme 3.1a). The durability of such interfaces is then limited by the rate of dissolution of the Si oxide in the electrolyte of interest.

np^+- and p^+-Si electrodes decorated with arrays of 3-6 μm diameter Ni islands have been reported to exhibit extended stability (> 24 h) in dark, open-circuit conditions and in the absence of protective electrolytes, even when > 80% of the Si surface is exposed to the alkaline electrolyte.[13, 17] An understanding of the chemical and spatial details of the failure processes of Si photoanodes and of the fundamental reasons why unprotected Si photoanodes do not readily fail by corrosion could provide a basis for strategies to extend the operational lifetimes of photoanodes.

Herein we have investigated the mechanism by which Si can exhibit extended operation for water oxidation under day/night cycling in alkaline electrolytes as well as under other conditions where Si would be expected to rapidly etch and undergo pit corrosion. A hypothesis is that the presence of O_2, along with an oxygen catalyst or a protective layer that can react with O_2, produces a surface potential that drives formation of Si oxide. This process (Scheme 3.1b) is analogous to that of a protective one-electron

redox-active oxidant in the electrolyte. We demonstrate that metal or metal oxide thin films such as Ni or NiO_x, in the presence of O_2, catalyze the dark, passive oxidation of Si in alkaline electrolytes. Such films can additionally induce local oxidation of exposed Si at pinholes or other film defects and thus lead to inherent defect tolerance of such interfaces. The catalyzed passivation of Si using Ni or NiO_x thin films is thus compatible with previous investigations of Si/Ni-based photoanodes that were only evaluated under constant illumination. This behavior provides a strategy for extending the stability of photoelectrodes at exposed regions during periods when the surfaces would otherwise be subject to etching and/or associated corrosion at pinholes in protection layers.[4, 5]

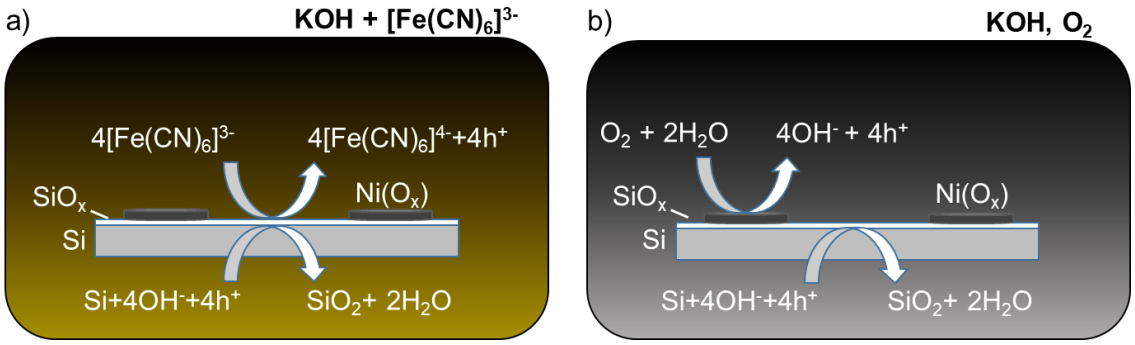

Scheme 3.1. Schematic of two Si passivation mechanisms for a Si anode decorated with $Ni(O_x)$ islands in alkaline electrolyte at open circuit in the dark. (a) $[Fe(CN)_6]^{3-}$ is introduced as a protective electrolyte and acts as an oxidizing agent for Si.[17] (b) $Ni(O_x)$ uptakes O_2 and catalyzes Si passivation. The electrode potential shifts positive, permitting holes from the Si valence band to react with the electrolyte and oxidize Si to SiO_2.

3.2 Materials and Methods

3.2.1 Chemicals and Materials

Unless otherwise stated, all chemicals listed were used as received, including potassium hydroxide (KOH, Macron Fine Chemicals, AR grade ≥ 85%), boric acid (H_3BO_3, Sigma-Aldrich, ≥ 99.5%), ammonium hydroxide (NH_4OH, EMD Millipore Co.,

28.0-30.0%), hydrochloric acid (HCl, EMD Millipore Co., 36.5-38%), hydrogen peroxide (H_2O_2, EMD Millipore Co., 30%), buffered oxide etchant (BOE, 6:1 NH_4F to HF, Transene Company, Inc.), boron nitride wafers (Saint-Gobain, BN-975 PDS), and Fumasep (Fuel Cell Store). Boron-doped, (100)-oriented p^+-Si (0.001-0.005 Ω cm resistivity) and phosphorous doped, (100)-oriented n-Si (0.1-1.0 Ω cm resistivity) wafers were purchased from Addison Engineering, Inc. Ni, Co, and Pt sputtering targets were obtained from the Kurt J. Lesker Company. Tetrakis(dimethylamido)-titanium (TDMAT, Strem Chemicals) was used for atomic layer deposition (ALD). Photoresist (Shipley 1813), MCC primer 80/20 (Microchem Corp.), and MF-319 developer (Microchem Corp.) were used for photolithography. Ag paint (Ted Pella, Inc.), gallium-indium eutectic (Alfa Aesar, 99.99%), and epoxy (Loctite 9460) were used for preparation of electrodes. Deionized water with a resistivity ρ > 18.2 MΩ cm was obtained from a Barnstead Millipore purification system.

3.2.2 Electrode Preparation

np^+-Si(100) photoelectrodes were fabricated via boron diffusion doping. Prior to doping, n-type Si wafers were cleaned by immersing in 5:1:1 H_2O:NH_4OH:H_2O_2 (by volume) at 75 ˚C for 15 min, followed by a 30 s etch in BOE to remove the oxide, immersing in 6:1:1 H_2O:HCl:H_2O_2 (by volume) at 75 ˚C for 15 min, and etching once more in BOE for 30 s. After each step the wafers were rinsed with deionized water and dried under flowing N_2(g). While the wafers were being cleaned, a tube furnace used for diffusion doping was heated to 950 ˚C for 30 min under a 5 L min^{-1} flow of O_2 to oxidize the boron nitride wafers. The gas supply was switched from O_2 to N_2 for 30 min followed

by cooling to 750 ˚C. The cleaned wafers were transferred to a tube furnace and placed a few mm from the oxidized boron nitride wafers. A p^+-emitter was formed on the wafers after increasing the temperature to 950 ˚C under a 2 L min^{-1} flow of N_2. To deglaze B_2O_3 from the surface, the sample was taken out and cooled before submerging in BOE for 2 min. Low-temperature oxidation was performed at 750 ˚C under 5 L min^{-1} for 30 min, followed by etching in BOE for 5 min to remove surface defects. The final sheet resistance was ~ 70-80 Ω sq^{-1} as measured by a four-point probe (Jandel).

Ni, NiO_x, Pt, and Co films were deposited onto np^+-Si or p^+-Si wafers using radio-frequency (RF) sputtering (AJA Orion sputterer). Prior to deposition, the p^+-Si electrodes were cleaned and etched in BOE by the same process described above for n-type wafers. For deposition of Ni, Co, and Pt, 100 W was applied to the metal target under 20 sccm of Ar flow at a 5 mTorr chamber pressure until the desired thickness of material was obtained. NiO_x films were deposited applying 120 W to the Ni target under 20 sccm Ar and 1 sccm O_2 at 300 ˚C at a chamber pressure of 5 mTorr. The deposition rate was calibrated via profilometry (Bruker DektakXT Stylus profilometer) of the film that had been deposited onto a glass slide. Unless otherwise stated, the thickness of Ni, Co, and Pt were 5 nm whereas NiO_x and Ni islands had thicknesses of 60 nm.

The p^+-Si/Ni islands (μNi) electrode was fabricated using photolithography and Ni sputtering as described in Chapter 2. Briefly, the Si wafer was RCA2 cleaned and dried before applying primer and Shipley 1813 positive photoresist via spin coater. The wafer was cured on a hot plate at 110 ˚C for 1 min and then exposed to UV light under a mask aligner. The chrome mask used produced an array of 3 μm diameter holes in the photoresist with 7 μm pitch. The pattern was developed in MF-319 for 2 min and baked at 110 ˚C for

1 min. 60 nm of Ni was sputter deposited. The photoresist was removed by sonicating the sample in acetone.

Amorphous TiO_2 films were deposited on cleaned Si via ALD (Cambridge Nanotech S200). For each ALD cycle, a 0.10 s exposure to TDMAT was followed by a 15 s, 20 sccm N_2 purge, a 0.015 s exposure to H_2O, and another N_2 purge. The deposition chamber was held at 150 ˚C and the TDMAT precursor was held at 75 ˚C throughout the deposition. A 1500 cycle was prepared leading to a 70 nm film as measured by spectroscopic ellipsometry (J.A. Woollam Co., alpha-SE).

A carbide scribe was used to cleave off edges of samples from the wafers, to prevent shunting during electrochemical operation. In-Ga eutectic was scratched onto the back of each sample and attached to Sn-coated Cu wire using Ag paint. The wire was threaded through a glass rod and the edges of the sample were sealed to the glass using epoxy. The epoxy was cured overnight before testing the electrode the following day. Electrode areas were determined using ImageJ software in conjunction with an optical image of the electrode surface.

3.2.3 Electrochemical Characterization

Electrodes were electrochemically tested in a three-electrode setup. A two-compartment cell separated by a Fumasep anion-exchange membrane was used for electrochemistry in KOH solution, whereas a two-compartment cell with the catholyte separated from the anolyte by a fritted glass tube was used for electrochemistry in 0.5 M K-borate buffer (K-Bi). Nominally 1 M KOH solutions were prepared by dissolving 56.0

g of hydrated KOH pellets into a total final volume of 1 L of deionized water, with the resulting pH measured as ~13.6.[19] K-Bi was prepared by mixing 1.0 M H_3BO_3(aq) and 0.5 M KOH(aq). The anolyte side of the cell was filled with 25 mL of electrolyte and the catholyte was filled to match the liquid height in the anolyte. Either O_2 or N_2 gas was bubbled into the anolyte as appropriate. A Hg/HgO reference electrode was used in KOH(aq) and a saturated calomel electrode (SCE) was used in K-Bi(aq). Reference electrodes were calibrated relative to the RHE using a Pt disk electrode in the respective electrolyte that was continually saturated with H_2. The Hg/HgO and SCE electrodes had potentials in the range of 0.908 - 0.920 V vs RHE and 0.772 - 0.785 vs RHE, respectively, in 1 M KOH(aq) and 0.5 M K-Bi(aq), respectively. Ni wire was used as the counter electrode and was in contact with the catholyte. A MPG-2 potentiostat (Bio-Logic Science Instruments) was used for electrochemical measurements. For working electrodes using Ni as an OER catalyst, the film was initially activated via cyclic voltammetry by cycling 20 times between 0.63 and 1.63 V vs RHE in KOH solution at 40 mV s^{-1} to incorporate Fe from solution and form NiFeOOH.

For long-term photoelectrochemical stability experiments, the working electrode was placed < 1 cm from the liquid surface and the electrolyte was replenished as necessary to maintain the liquid level. Illumination was provided with an ELH-type tungsten-halogen lamp and was calibrated to an equivalent power density of 100 mW cm^{-2} using a calibrated Si photodiode (Thorlabs). Photoelectrochemical stability was evaluated by cycling the electrode between day and night intervals within a 24 h period. Day cycles involved 6 h of continuous water oxidation under 100 mW cm^{-2} of simulated solar illumination at either 1.63 V vs RHE in KOH or at 1.73 V vs RHE in K-Bi, to ensure that the light-limited

photocurrent density was reached in each case. Prior to each day cycle, the photoelectrodes were cycled between 0.63 V and either 1.63 V or 1.73 V vs RHE in KOH(aq) and K-Bi(aq), respectively, at 40 mV s^{-1}. Night cycles involved holding the photoelectrode at open circuit in the dark for 18 h.

3.2.4 Material Characterization

Scanning electron microscopy (SEM) was performed using a FEI Nova NanoSEM 450 with accelerating voltages of 10 kV and a working distance of 5.0 mm. Energy-dispersive X-ray spectroscopy (EDS) was performed at accelerating voltages of 15 kV. Atomic force microscopy (AFM) was performed using a ScanAsyst-Air probe (Bruker) with a nominal tip radius of 2 nm in a Bruker Dimension Icon AFM using Peak Force Tapping mode. The Peak Force amplitude and frequency were set to 100 nm and 2 kHz, respectively. The image was measured using the software Nanoscope v9.7 and was analyzed using Nanoscope Analysis v1.9.

X-ray photoelectron spectroscopy (XPS) was performed using a Kratos Axis Ultra system at a base pressure of 1 x 10^{-9} Torr. Samples were irradiated with a monochromatic Al Kα source using X-rays (1486.7 eV) at 450 W. A hemispherical analyzer oriented normal to the sample surface was used to maximize the depth sensitivity. High-resolution spectra were acquired at a resolution of 25 meV with a pass energy of 10 eV. CasaXPS computer software was used to analyze the XPS data. The spectra were first calibrated by referencing the C 1s peak position to 284.8 eV, followed by peak fitting for Ni $2p_{3/2}$ to Ni subspecies.[20, 21] For simplicity, satellite and Ni $2p_{1/2}$ peaks of each subspecies were not used in peak fitting.[6] The same peak width was used in all samples for a particular species.

The XPS data were measured ex-situ, which could potentially confound surface composition and oxidation states relative to those in the electrochemical measurements.

Inductively coupled plasma mass spectrometry (ICP-MS) data were collected using an Agilent 8800 Triple Quadrupole ICP-MS system to measure the extent of Si dissolution in 0.5 M K-Bi either at open circuit or at 1.63 V vs RHE. To ensure that Si dissolution did not result from the borosilicate glass in the electrochemical cell, reference electrode, or working electrode, polypropylene and Teflon were used instead of glass. ICP-MS samples were collected periodically by removing 1 mL of solution at set time intervals. Before analysis, samples were diluted by a factor of 10 with 2% nitric acid. ICP-MS concentration standards were made by serial dilutions of a known concentration standard (Sigma-Aldrich) with 2% nitric acid. ICP-MS measurements were conducted using hydrogen as a reaction gas to eliminate interference due to atmospheric nitrogen in the measurement of Si. The total amount of dissolved Si from the electrodes was then calculated and normalized to the geometric electrode area.

The procedure for determining Si etch rate in KOH (Fig. 3.2) is also described in Chapter 2. Briefly, a Si wafer was subjected to 950 ˚C for 6 h in air to grow a thermal oxide. A 10 μm by 100 μm array of rectangles was patterned using the same photolithography procedures as above. The patterned wafers were etched in BOE for 3 min to create trenches and the photoresist was removed with acetone. The samples were cleaved and made into electrodes. The electrodes were tested in a standard 3-electrode cell with 1 M KOH(aq) and a potential was applied. After 20 h, the sample was removed from the electrode and submerged in BOE for 5 min to remove the thermal oxide. AFM was used to

quantify height differences between the not etched Si surface (previously underneath the thermal oxide) and the exposed trenches.

3.3 Results

3.3.1 Passivation and Etching Behavior of Si in KOH solution

Fig. 3.1 shows the voltammetric behavior of p^+-Si(100) electrodes between -0.1 and 1.3 V vs RHE in nominally 1 M KOH(aq) that had been saturated with 1 atm of either O_2(g) or N_2(g). The peaks of the anodic current at 0.17 V and 0.25 V vs RHE for O_2-saturated and N_2-saturated Si samples, respectively, correspond to the passivation potential, E_{PP}. The decrease in current at potentials positive of E_{PP} indicates the formation of a passivating surficial Si oxide.[22]

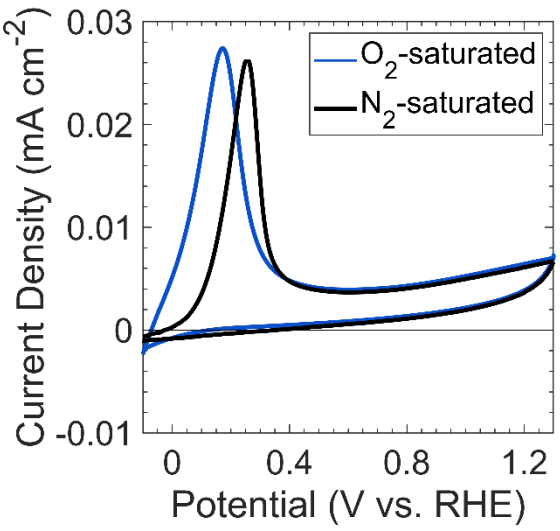

Figure 3.1. Cyclic voltammograms of p^+-Si in O_2- (blue) and N_2- (black) saturated, 1 M KOH(aq) at a 1 mV s^{-1} scan rate in the dark.

The dissolution rate, r_D, of p^+-Si(100) in 1 M KOH(aq) at open circuit (~ -0.1 V vs RHE) was $r_D > 10^2$ nm h^{-1} at room temperature.[17] Fig. 3.2 shows r_D as a function of the electrode potential. r_D at a given potential was determined by etching exposed Si on an electrode patterned with a thermal oxide mask in 1 M KOH(aq), followed by removing the mask using buffered oxide etch, and measuring the resulting trench height using atomic force microscopy (Fig. 3.2c). The rate decreased to 71.6 nm h^{-1} at 0.2 V vs RHE and decreased further to a minimum of 1.7 nm h^{-1} at 0.5 V vs RHE, consistent with the formation of a slowly dissolving SiO_x layer at these potentials.[23] The dissolution rate increased monotonically as the potential was increased to > 0.5 V vs RHE. Over the entire potential range, $r_D(E)$ correlated closely with the current density at the potential, E, of interest (Fig. 3.2b). At low (< 2 V) applied voltages, the Si dissolution behavior is consistent with expectations for a surface covered by a potential-dependent, steady-state thickness of Si oxide.[24]

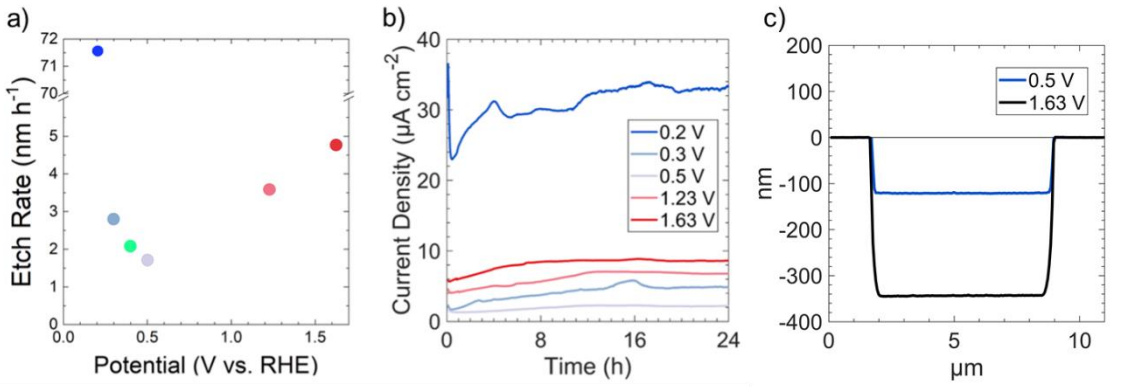

Figure 3.2. (a) Dissolution rate of p^+-Si(100) in 1 M KOH(aq) in the dark at various potentials and (b) the corresponding chronoamperogram over a 24 h period. (c) Cross-section of p^+-Si(100) representative etch pits under 0.5 V (blue) and 1.63 V (black) vs RHE in 1 M KOH(aq) for 72 h.

3.3.2 Catalyzed Passivation of p^+-Si by Ni in O_2-saturated 1 M KOH(aq)

The morphology of etched Si(100) in KOH solution was used to provide information on the mechanism of the potential-dependent Si etching in the presence of various catalysts and surface layers.[25] In 1 M KOH(aq), the Si(100) facets etch more rapidly than the Si(111) facets, leading to the formation of inverted pyramid-shaped pits on the Si(100) surface.[10, 22, 26] Conversely, the SiO_x passivation layer etches isotropically but at a rate < 0.1 times that of Si, leading to facet-independent circular etch pits on oxide-covered Si surfaces.[15, 17]

Fig. 3.3 displays the open-circuit etching behavior of p^+-Si(100), of p^+-Si(100) with a thin film of 5 nm Ni (p^+-Si(100)/Ni), and of p^+-Si(100) with 60 nm of NiO_x (p^+-Si(100)/NiO_x) in strongly alkaline 1 M KOH(aq) saturated with 1 atm of either O_2(g) or N_2(g). Electrodes tested in N_2-saturated solution were used as a control during which O_2 was purged from the cell. Unless otherwise stated, all of the films on Si were deposited as continuous thin films. Bare p^+-Si(100) electrodes, in O_2- or N_2-saturated solutions, had open-circuit potentials, E_{oc}, < E_{PP} with average potentials of E_{oc} = -0.07 and -0.11 V vs RHE, respectively (i.e. more than 0.2 V negative of E_{PP}). This low E_{oc} implies the direct dissolution of Si at open circuit regardless of whether O_2 is present in the solution. In N_2-saturated solution, p^+-Si(100)/Ni or p^+-Si(100)/NiO_x surfaces initially exhibited E_{oc} ~ 0.6 vs RHE and E_{oc} ~ 1.0 V vs RHE, respectively; however, within a few hours the E_{oc} of both surfaces decreased to < 0 V vs RHE (Fig. 3.3b). In contrast, in O_2-saturated solution, p^+-Si(100)/Ni or p^+-Si(100)/NiO_x surfaces exhibited E_{oc} > 0.60 and > 0.85 V vs RHE, respectively, throughout the duration of the experiment (Fig. 3.3a).

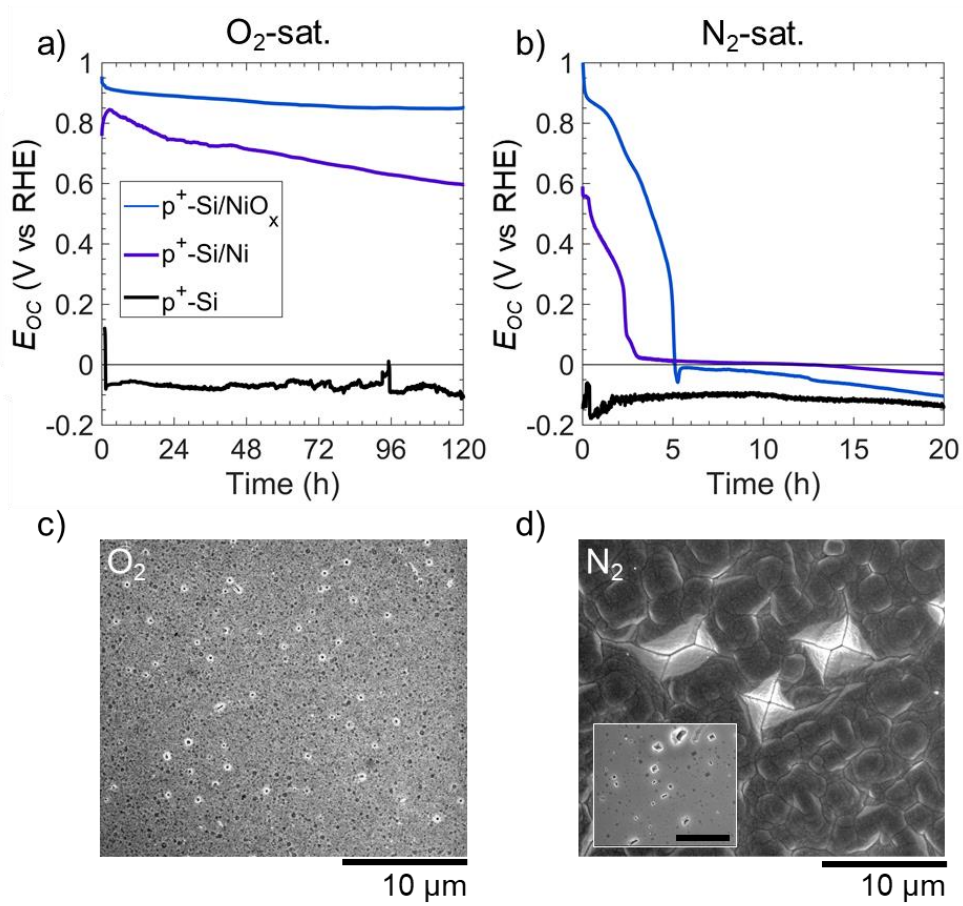

Figure 3.3. (a-b) Open-circuit potential vs time of p^+-Si(100) (black), p^+-Si(100)/Ni (purple), and p^+-Si(100)/NiO_x (blue) electrodes in contact with (a) O_2- and (b) N_2-saturated 1 M KOH(aq). (c-d) Scanning-electron micrographs of p^+-Si(100)/Ni electrodes after immersion for 120 h in (c) O_2-saturated and (d) N_2-saturated 1 M KOH(aq). Energy-dispersive X-ray spectroscopy confirmed that Ni was no longer on the surface on (d). Inset in (d) shows p^+-Si/Ni after immersion in N_2-saturated KOH for 20 h, with the scale bar at 5 µm.

The resulting etched electrode surfaces were characterized using scanning electron microscopy (SEM). After 120 h at open circuit in the O_2-saturated electrolyte, SEM images of the p^+-Si(100)/Ni surface showed circular etch pits (Fig. 3.3c). In contrast, after only 20 h at open-circuit in the N_2-saturated electrolyte (Fig. 3.3d, inset) p^+-Si(100)/Ni surfaces displayed inverted pyramids that visibly undercut the Ni film. Further, after 120 h continued undercutting led to a merging of the Si etch pits with the complete delamination

of the Ni film on p^+-Si(100)/Ni surfaces under N_2, as confirmed by energy-dispersive X-ray spectroscopy (EDS, Fig. 3.4). Qualitatively similar open-circuit etching behavior was also observed for p^+-Si(100)/NiO_x electrodes in either O_2- or N_2-saturated solutions (Fig. 3.5). The cross section of the sample saturated in O_2 showed that the underlying Si remained intact (Fig. 3.5c).

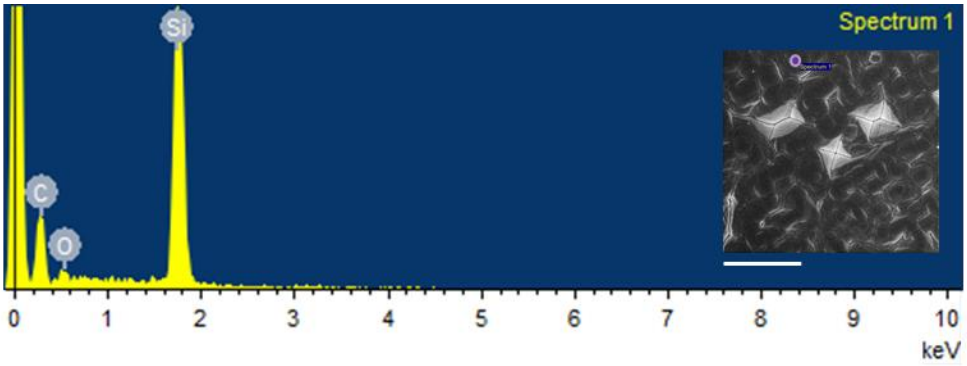

Figure 3.4. Energy dispersive X-ray spectrum of p^+-Si/Ni (5 nm) after 120 h in N_2-saturated 1 M KOH(aq). Inset shows corresponding scanning electron micrograph; the purple dot indicates location of scan. Scale bar is 10 μm.

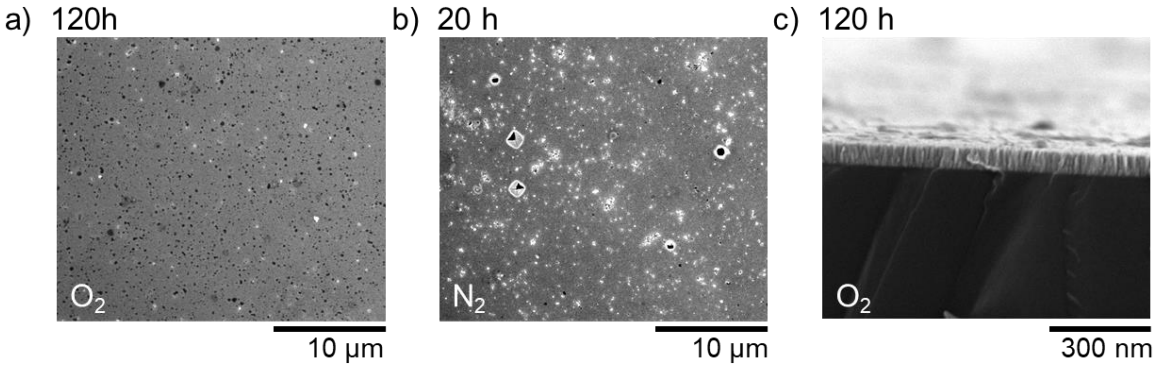

Figure 3.5. (a-b) Top-down scanning electron micrographs of p^+-Si(100)/NiO_x electrodes in 1 M KOH(aq) at open circuit saturated with (a) O_2 for 120 h and (b) N_2 for 20 h. (c) Cross section of sample in (a) showing the NiO_x coating on the Si substrate.

To further investigate the potential-dependent behavior of the etching of Si electrodes, a p^+-Si(100)/Ni electrode was held at E = -0.1 V vs RHE in O_2-saturated 1 M KOH(aq). After 20 h, SEM images showed inverted pyramids undercutting the Ni film (Fig. 3.6), similar to the behavior of a p^+-Si(100)/Ni sample in a N_2-saturated solution.

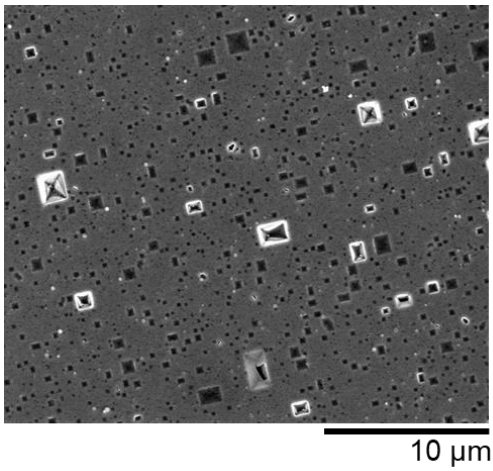

Figure 3.6. Scanning electron micrograph of p^+-Si(100)/Ni (5 nm) after being potentiostatically held at -0.1 V vs RHE for 20 h in O_2-saturated 1 M KOH(aq).

Fig. 3.7 shows E_{oc} as a function of the thickness of the Ni film on p^+-Si(100)/Ni electrodes in O_2- and N_2-saturated 1 M KOH(aq). In O_2-saturated solutions, all electrodes showed initial values of E_{oc} between 0.7 and 0.8 V vs RHE. E_{oc} remained in this range for the first hour, but after 120 h, E_{oc} was 0.29, 0.60, 0.64, and 0.73 V vs RHE for 3 nm, 5 nm, 30 nm, and 60 nm thick Ni films on p^+-Si(100), respectively. Fig. 3.8 shows SEM images of these electrodes after 120 h at open circuit in O_2-saturated 1 M KOH(aq). Pronounced and spatially dense pinholes were produced on the p^+-Si(100)/Ni electrode that had 3 nm of Ni, whereas the pinhole density decreased with increasing Ni thickness. The p^+-Si(100)/Ni electrode with 60 nm of Ni exhibited much less undercutting of Ni. Regardless of the Ni film thickness, in N_2-saturated 1 M KOH(aq), E_{oc} for the p^+-Si/Ni electrodes

decreased to < E_{PP} within a few h of immersion, with 3 nm, 5 nm, and 30 nm thick Ni films requiring 1.6 h, 2.3 h, and 3.3 h, respectively, to produce E_{oc} < 0.2 V vs RHE (Fig. 3.7b).

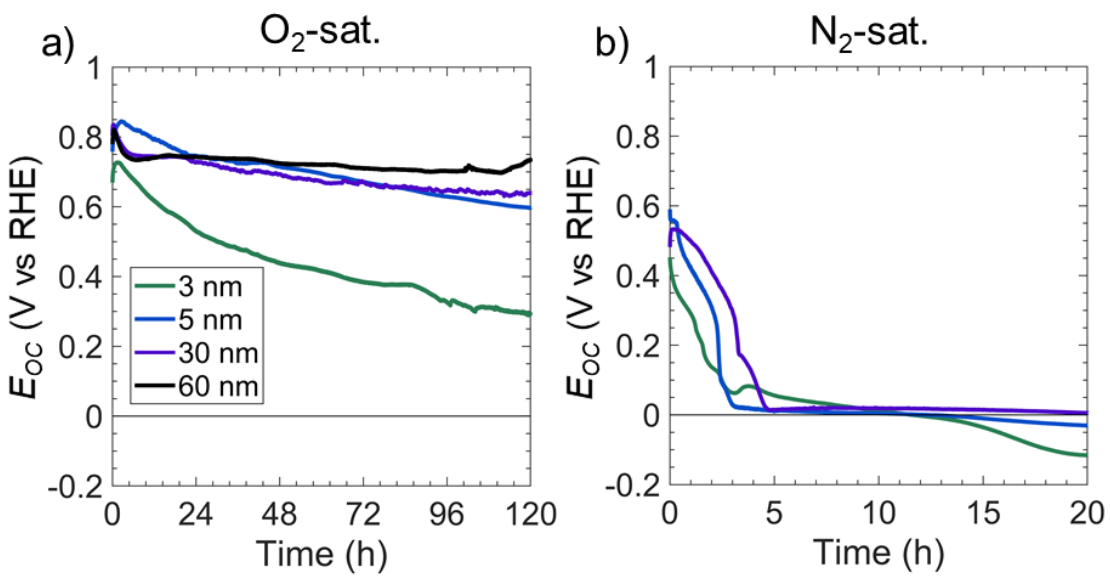

Figure 3.7. Comparison of open-circuit potential vs time for p^+-Si/Ni electrode with Ni film thicknesses at 3 nm (green), 5 nm (blue), 30 nm (purple), and 60 nm (black, (a) only) in (a) O_2- and (b) N_2-saturated 1 M KOH(aq) solution.

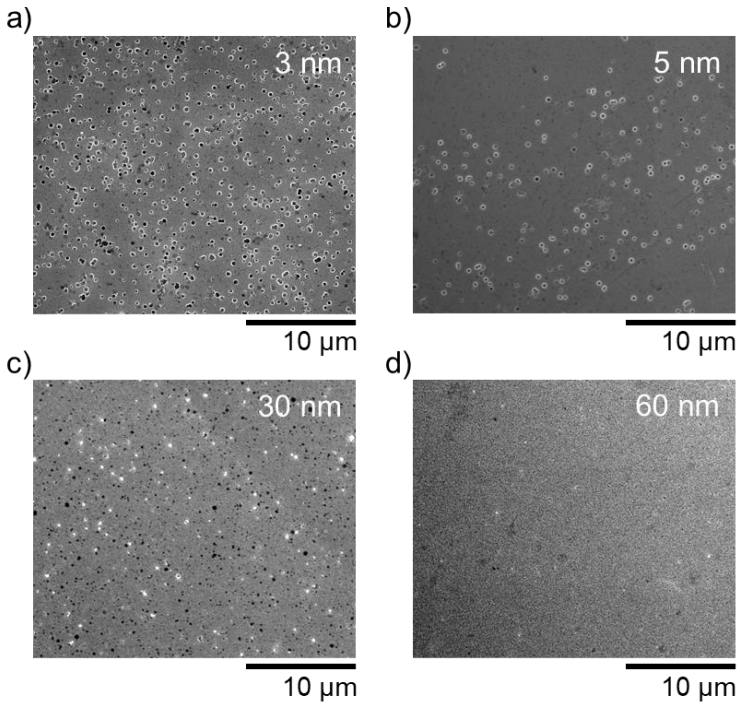

Figure 3.8. Scanning electron micrographs of p^+-Si deposited with Ni film thicknesses at (a) 3 nm, (b) 5 nm, (c) 30 nm, and (d) 60 nm after 120 h at open circuit in O_2-saturated 1 M KOH(aq).

Fig. 3.9 shows the behavior in O_2-saturated 1 M KOH(aq) of p^+-Si(100) electrodes coated with discrete, patterned Ni islands (μNi). A p^+-Si electrode was patterned with an array of 60 nm thick, 3 μm diameter Ni islands (μNi) with a 7 μm pitch, p^+-Si(100)/(μNi). This electrode exhibited a relatively steady potential of E_{oc} = 0.6 V vs RHE for ~ 120 h. Despite ~ 86% of the Si surface being exposed to the electrolyte, the electrode did not exhibit characteristics of direct Si etching in the absence of illumination. In fact, SEM images showed no signs of inverted pyramid formation after the 120 h experiment, and the μNi array remained intact with minor radial undercutting (~ 300 nm) of the μNi islands. The etching of the exposed Si surface was similar to the behavior exhibited by a Si/μNi electrode in KOH(aq) that contained a passivating electrolyte.[17]

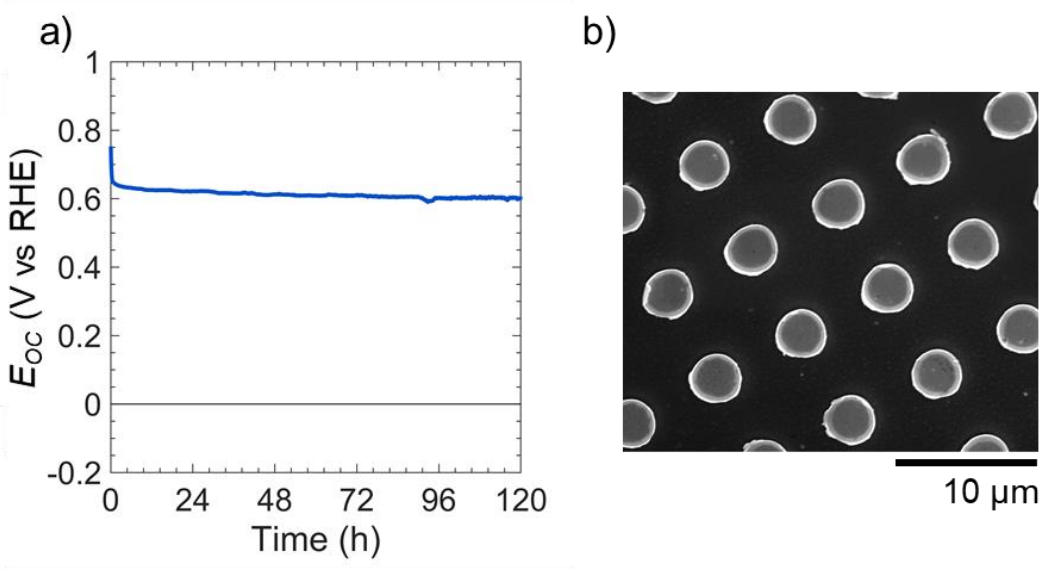

Figure 3.9. Catalyzed passivation of exposed Si using Ni islands (μNi) in 1 M KOH. (a) Open-circuit potential vs time of p^+-Si decorated with 60 nm thick μNi in O_2-saturated, 1 M KOH(aq). (b) Scanning electron micrograph of p^+-Si/μNi after testing for 120 h. An array of 3 μm diameter μNi covered ~ 14% of the Si surface.

Fig. 3.10 compares the electrochemical behavior of p^+-Si/NiO_x electrodes in O_2- or N_2-saturated 1 M KOH(aq). The E_{oc} of electrodes was measured for 6 h in 1 M KOH(aq), followed by chronoamperometry (CA) at 0.3 V vs RHE for 1 h, after which cyclic voltammetry (CV) was performed from E_{oc} to +0.4 to -0.4 V vs E_{oc} at 10 mV s^{-1}. This cycle was repeated three times. At a potential that is positive of E_{PP}, 0.3 V vs RHE, reductive current was observed in both O_2-saturated and N_2-saturated solutions (Fig. 3.10b).

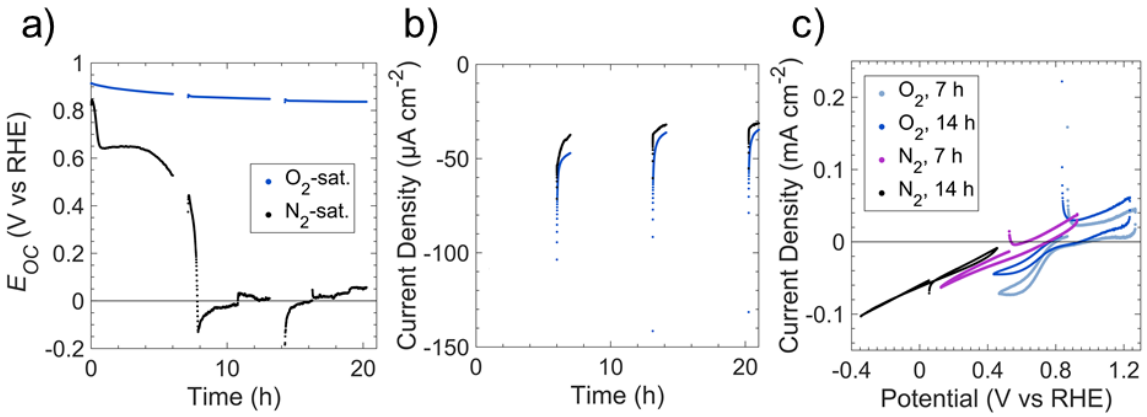

Figure 3.10. Electrochemical data of p^+-Si/NiO_x (60 nm) electrodes in 1 M KOH(aq) in the dark. (a) Open-circuit potential (E_{oc}) vs time over 6 h intervals in O_2-saturated (blue) or N_2-saturated (black) solutions. (b) Chronoamperogram at 0.3 V vs RHE for 1 h taken at 6, 13, and 20 h after the E_{oc} measurements in (a). (c) Cyclic voltammograms in O_2- (light blue and blue) or N_2-saturated (purple and black) solutions taken after 7 and 14 h cycles, respectively. The scans were cycled from E_{oc} to +0.4 V to -0.4 V vs E_{oc} at 10 mV s^{-1}.

As-deposited Ni films exhibit a relatively high overpotential for the OER in 1 M KOH(aq), in contrast to Fe-doped, Ni oxy-hydroxy (NiFeOOH) films.[27] Fig. 3.11 compares the open-circuit potentials in 1 M KOH(aq) for p^+-Si(100) electrodes coated with either Ni or NiFeOOH films. Ni was converted to NiFeOOH by cycling the electrode potential between 0.3 and 1.63 V vs RHE at 40 mV s^{-1} in 1 M KOH(aq) to oxidize the Ni and incorporate residual Fe from the solution.[28] In both O_2- and N_2-saturated 1 M KOH(aq),

p^+-Si(100)/NiFeOOH electrodes initially displayed E_{oc} = 0.96 V vs NHE, but E_{oc} decreased within < 2 h of operation and converged towards E_{oc} values characteristic of as-deposited Ni films in both O_2- and N_2-saturated solutions. For the O_2-saturated solution, E_{oc} = 0.65 V vs RHE after 83 h, whereas for the N_2-saturated solution, E_{oc} = 0.07 V vs RHE after 4.3 h. The shift in E_{oc} of the Ni film in O_2- or N_2-saturated solution can be ascribed to changes in the relative amounts of oxidized Ni on the surface. The Ni oxy-hydroxy film readily converts to Ni oxide on the electrode surface at E_{oc},[29] because the potential for converting Ni^{II} into Ni^{III} is positive of E_{oc}, lying in a potential region of ~1.3 V vs RHE.[30]

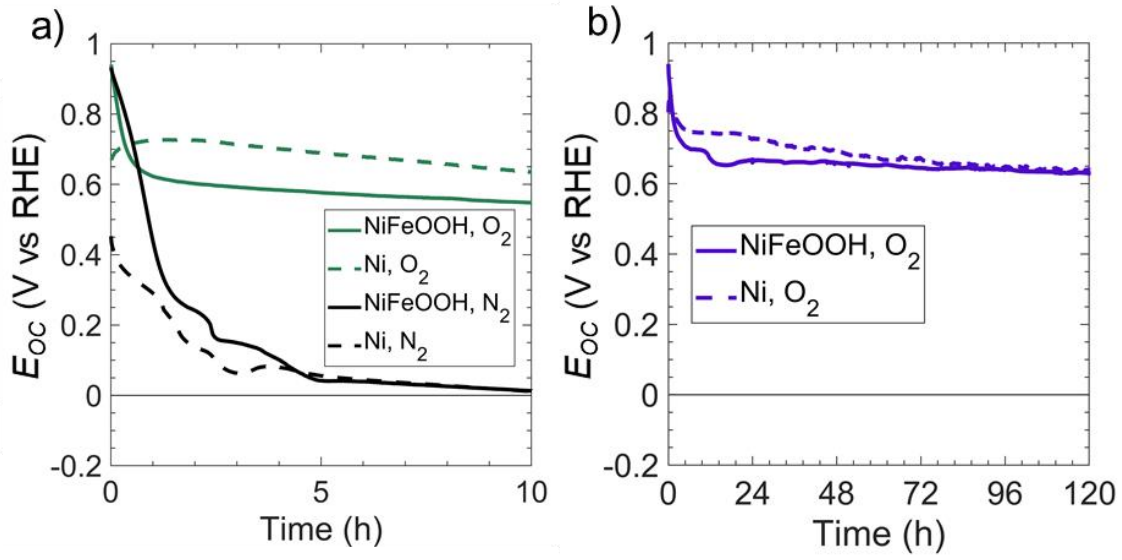

Figure 3.11. Comparison of the dark E_{oc} vs time behavior of p^+-Si/Ni electrodes in 1 M KOH(aq) with and without initial cycling of the catalyst. (a) Open-circuit potential of 3 nm thick Ni films with (solid line) and without (dashed line) cycling in O_2 (green) or N_2 (black) saturated solution over a short time period. (b) Open-circuit potential of 30 nm thick Ni films over an extended time period. Cycled films had a potential applied over 20 cycles between 0.63 and 1.63 V vs. RHE at 40 mV s^{-1} to convert Ni to NiFeOOH.

3.3.3 Si Passivation using Other Catalysts

The open-circuit potential of p^+-Si(100) electrodes coated with either Pt, Co, or TiO_2 was also evaluated in O_2-saturated KOH solution (Fig. 3.12). Amorphous TiO_2 was investigated due to its ability to provide a protective layer on Si,[3, 11, 31] whereas Pt and Co were chosen due to their electrocatalytic activity for the ORR.[32-34] p^+-Si(100)/Pt electrodes displayed $E_{oc} > 0.8$ V vs RHE for 120 h, with minimal undercutting of the film (Fig. 3.12b). In contrast, within a day of immersion of p^+-Si(100)/Co or p^+-Si(100)/TiO_2 surfaces, E_{oc} decreased from initial values of $E_{oc} = 0.74$ and $E_{oc} = 0.49$ V vs. RHE, respectively, to < 0.25 V vs RHE. After immersion, both types of electrodes exhibited inverted pyramid etch

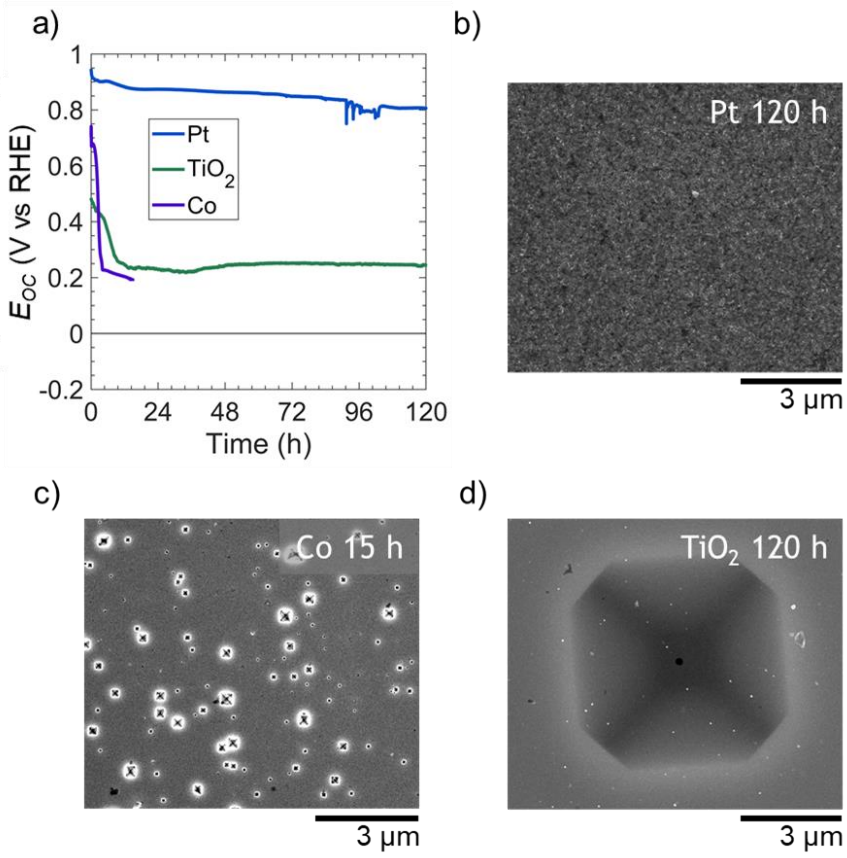

Figure 3.12. (a) Open-circuit potential vs time for p^+-Si coated with Pt (blue), amorphous TiO_2 (green), or Co (purple) thin films in O_2-saturated 1 M KOH(aq). (b-d) Scanning electron micrographs of p^+-Si coated with (b) Pt, (c) Co, or (d) TiO_2 imaged after submerging in KOH for 120 h, 15 h, and 120 h, respectively.

pits (Fig. 3.12c-d), indicating that despite E_{oc} being slightly (< 0.1 V) more positive than E_{PP}, the rate of Si dissolution at open-circuit was greater than the rate of Si oxidation. No apparent correlation was observed between the catalytic activity of Pt, Co, Ni, and NiO_x films for the ORR and the catalyzed passivation of Si (Fig. 3.13).

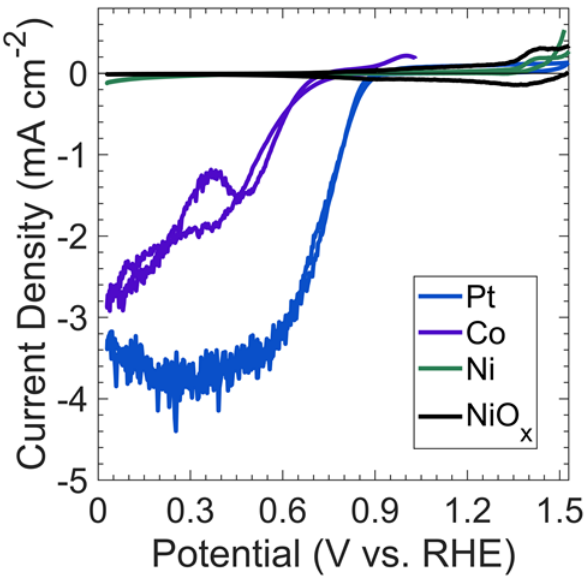

Figure 3.13. Cyclic voltammograms for the oxygen reduction reaction for Pt (blue), Co (purple), Ni (green), and NiO_x (black) thin films on n^+-Si in 1 M KOH(aq) under O_2-saturation and vigorous stirring.

3.3.4 Photoelectrochemical Characterization of Catalytically Passivated Si Photoanodes Subjected to Simulated Day/night Cycling

Fig. 3.14 depicts the photoelectrochemical performance and stability of np^+-Si(100)/NiO_x photoanodes in 1 M KOH(aq) while undergoing cycling between 18 h intervals at open-circuit conditions in the dark ("night") and 6 h intervals of 100 mW cm^{-2} illumination at E = 1.63 V vs RHE ("day"). The photoelectrochemical cell was open to ambient air (~ 0.2 atm O_2) but was not continuously purged with O_2. Throughout the duration of the experiment, the photoelectrode exhibited a light-limited current density of

31.0 ± 1.5 mA cm^{-2} during the day cycle (Fig. 3.14a), with small variations of photocurrent within individual day cycles consistently attributable to differing amounts of electrochromic darkening.[35] Cyclic voltammograms collected at the beginning of each day cycle (Fig. 3.14b) were also essentially unchanged throughout the experiment. From 0 h to

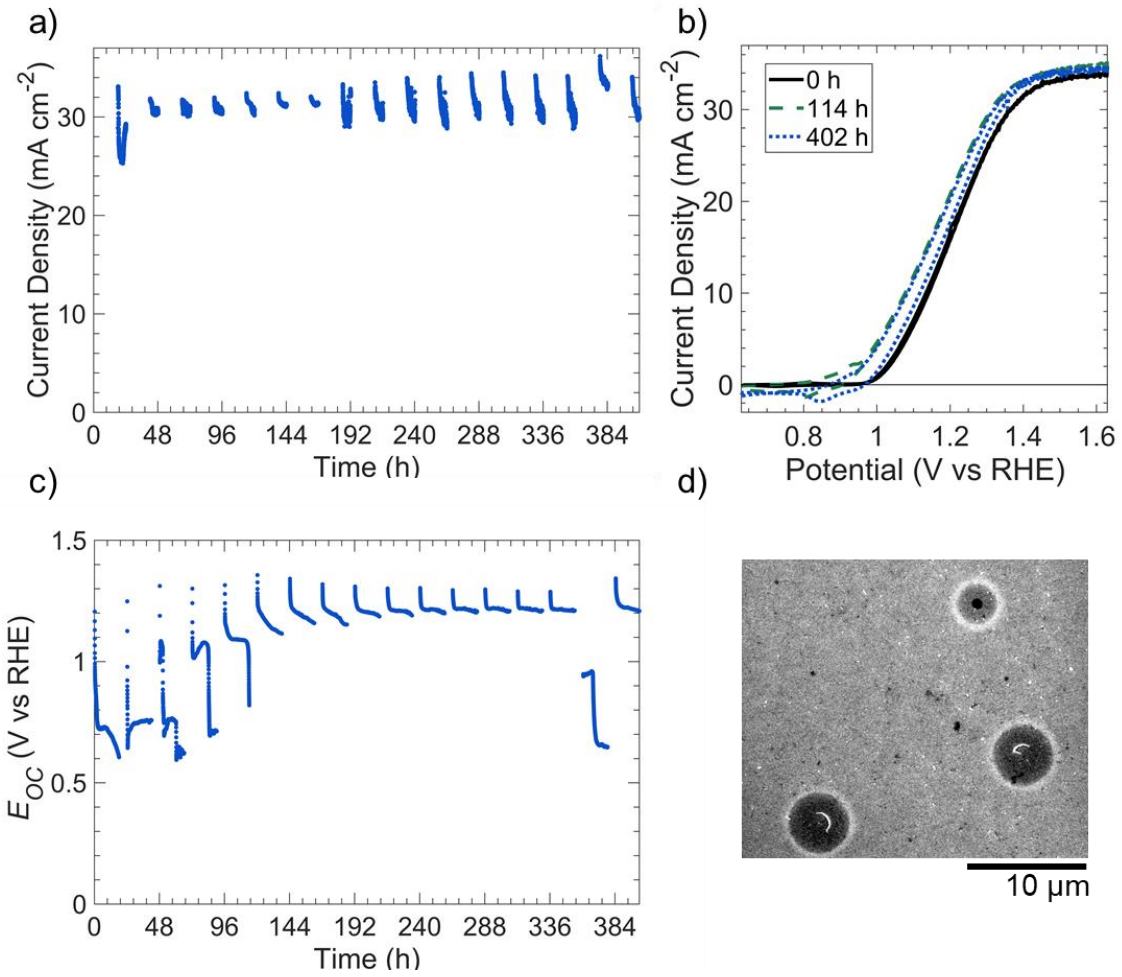

Figure 3.14. Stability and performance of np^{+}-Si(100)/NiO_x photoelectrodes subjected to cycling between simulated day and night conditions in 1 M KOH(aq). The deposited thickness of NiO_x was 60 nm. (a) Chronoamperometric stability in 1 M KOH(aq) at 1.63 V vs RHE. (b) Cyclic voltammetry of electrode under simulated 1 sun illumination at 0 h (black, solid line), 114 h (green, dashed line), and 402 h of testing (blue, dotted line). The voltammetric scan rate was 40 mV s^{-1}. For (a-b), photoelectrodes were measured for 6 h intervals under simulated 100 mW cm^{-2} of illumination provided by an ELH-type W-halogen lamp. (c) Open-circuit potentials of the photoelectrode in the dark for 18 h intervals. The electrolyte was replenished at 168 h and 378 h to account for evaporation. (d) Scanning electron micrographs of photoelectrodes after the stability test.

114 h, the shift in potential (0.13 V shift negative at a current density of 1 mA cm^{-2}) and the increase in current density for the Ni^{III}/Ni^{II} redox peaks were consistent with an increase in catalytically active sites exposed to the electrolyte.[6] Throughout every simulated night cycle, E_{oc} was > 0.6 V vs RHE (Fig. 3.14c), indicating that the Si was coated with a passivating oxide layer and confirming that the O_2 concentration in the electrolyte was sufficient to maintain the passivating oxide. At the beginning of each simulated night cycle, E_{oc} started at ~ 1.3 V vs RHE and decreased to either ~ 0.6 – 0.8 V vs RHE in the first five night cycles or ~ 1.2 vs RHE during subsequent night cycles. The change in E_{oc} during each night cycle suggests that the catalytically active Ni^{III} oxy-hydroxy film generated during the day likely converted to a Ni^{II}-based oxide during the night.

After day/night cycling, SEM images revealed isotropically etched Si at pinholes in the photoelectrode (Fig. 3.14d). The images revealed that the NiO_x film remained intact on the Si surface with some undercutting around the pinholes, as expected for Si/Ni electrodes in alkaline media.[6] In the Si 2p X-ray photoelectron spectrum (XPS) of the photoelectrode surface that was subjected to day/night cycling, a weak SiO_2 signal (102.6 eV binding energy), but no Si peak (~ 99 eV), was present.[36] This behavior confirms that the exposed regions of the surface were small areas of oxidized Si under pinholes, with the majority of the unoxidized Si being obscured by the NiO_x film (Fig. 3.15).

Under similar day/night cycling conditions, an np^+-Si/TiO_2/Ni photoanode in 1 M KOH(aq) did not exhibit catalyzed passivation despite the presence of a conformal layer of Ni on the TiO_2 film (Fig. 3.16). Instead, the electrode exhibited similar open-circuit behavior to that of p^+-Si/TiO_2 electrodes in the dark (Fig. 3.12). Although the photoanode maintained performance for the first 216 h of the run, from 216 h to 312 h the photocurrent

density decreased by ~ 17%. Further, the bias sufficient to produce 10 mA cm^{-2} of photocurrent density under simulated 100 mW cm^{-2} illumination increased by 90 mV (Fig. 3.16c), indicating substantial corrosion of the underlying np^{+}-Si junction. Large (> 20 μm) inverted pyramid etch pits that undercut the TiO_2/Ni film were observed by SEM after 312 h of day/night cycling (Fig. 3.16d).

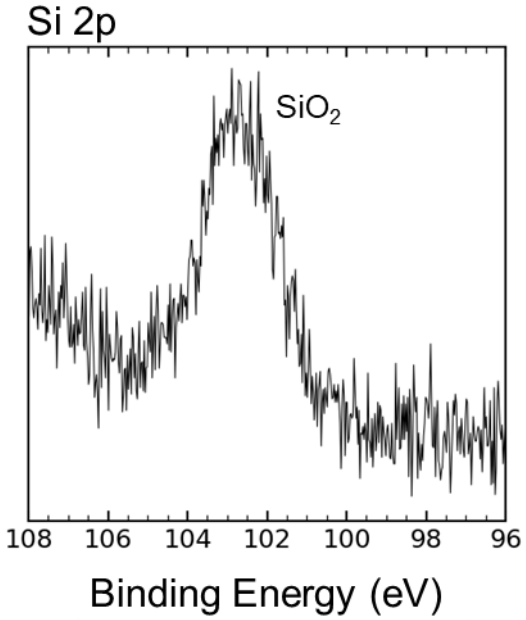

Figure 3.15. X-ray photoelectron spectrum in the Si 2p region of an np^{+}-Si/NiO_x photoelectrode after extended stability testing under day/night cycling. The y-axis is in arbitrary units.

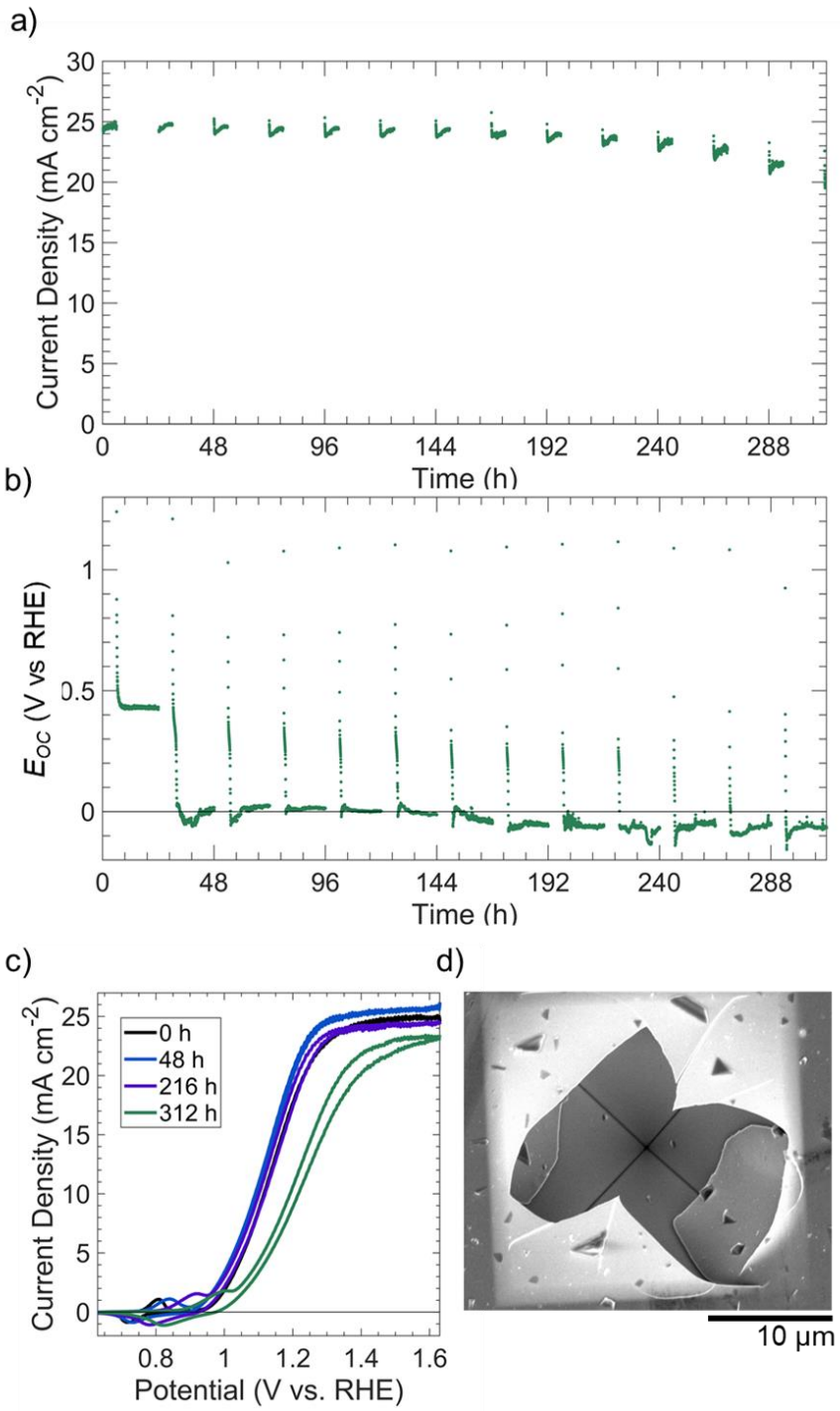

Figure 3.16. Stability and performance of np^{+}-Si/TiO_2/Ni photoanode under day/night cycling in O_2-saturated 1 M KOH(aq). (a) Chronoamperogram under 100 mW cm^{-2} illumination and 1.63 V vs RHE for 6 h intervals. (b) Open-circuit potential vs time in the dark for 18 h intervals. (c) Cyclic voltammograms under 1 sun simulated illumination after 0 h (black), 48 h (blue), 216 h (purple), and 312 h (green) of testing (d) Scanning electron micrograph of photoanode after testing depicting a Si etch pit undercutting the TiO_2/Ni layers.

3.3.5 Surface Characterization of Catalytically Passivated p^+-Si/Ni and np^+-Si/NiO_x

Fig. 3.17 compares the XPS data in the Ni $2p_{3/2}$ region for as-deposited p^+-Si/Ni electrodes to p^+-Si/Ni electrodes that had been immersed for 20 h in N_2-saturated 1 M KOH(aq), as well as to p^+-Si/Ni electrodes that had been immersed for 20 h in O_2-saturated 1 M KOH(aq). The XPS emission at a binding energy of 852.4±0.1 eV is associated with metallic Ni, whereas the emissions at binding energies of 853.5±0.2 and 855.8±0.2 eV are associated with phases of NiO and $Ni(OH)_2$.[20, 37] The presence of NiO_x peaks indicated that the oxidation of Ni proceeded at open circuit in 1 M KOH(aq) when O_2 was present in solution, as suggested by the increase in the high-energy peak shaded in light blue (Fig. 3.17). Alternatively, after 20 h in N_2-saturated 1 M KOH(aq), the composition of the Si surface was similar to that of the as-deposited electrode. After 120 h at open circuit in O_2-

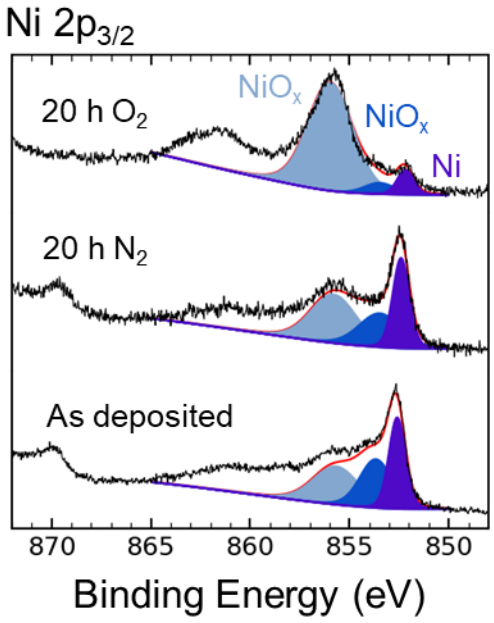

Figure 3.17. X-ray photoelectron spectroscopic data in the Ni $2p_{3/2}$ region of p^+-Si/Ni (5 nm thick) electrodes. Electrodes were measured as deposited and after 20 h at open circuit in either N_2- or O_2-saturated 1 M KOH(aq). Ni $2p_{3/2}$ emission was fitted with three peaks. The lowest energy peak at 852.4 eV (purple) is ascribable to Ni metal, and the higher energy peaks (blue and light blue) are assigned to NiO and $Ni(OH)_2$. The y-axis is in arbitrary units.

saturated 1 M KOH(aq), atomic force microscopy (AFM) showed that the Ni surface morphology exhibited an increase in average surface roughness (R_a), from 0.2 to 1.8 nm, as a result of immersion in KOH(aq), and grain boundaries subsequently formed on the Ni surface (Fig. 3.18). Cross-sections of the AFM illustrate the etch pit morphology caused by SiO_x dissolution (Fig. 3.18c).

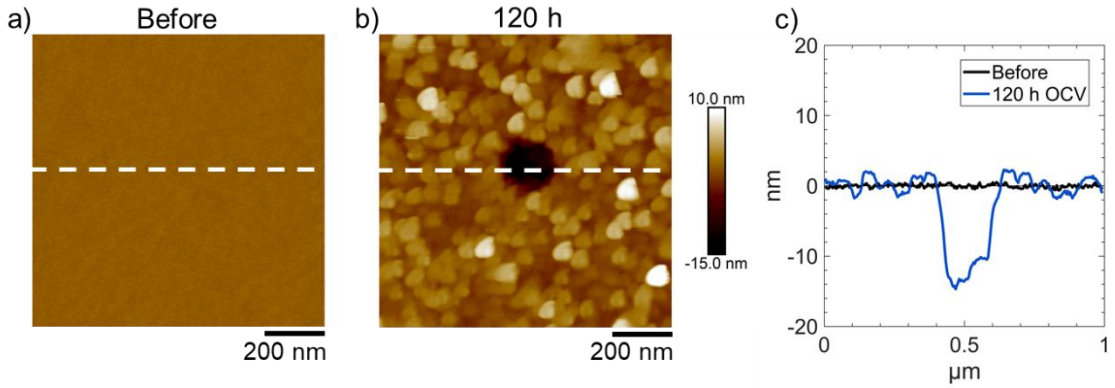

Figure 3.18. Atomic force microscope images of p^+-Si/Ni topography (a) before and (b) after 120 h submerging in 1 M KOH(aq) at open circuit. (c) Cross-section of electrode before (black) and after submerging in KOH (blue) at the indicated white dashed line in (a-b).

Fig. 3.19 shows the Ni $2p_{3/2}$ XPS data for as-deposited, np^+-Si/NiO_x photoelectrodes relative to np^+-Si/NiO_x photoelectrodes after 20 h in O_2-saturated 1 M KOH(aq) at open circuit, as well as after extended day/night stability cycling (Fig. 3.14). Prior to XPS measurements, the open-circuit potentials for the latter two photoelectrodes were E_{oc} ~ 0.6 V vs RHE and E_{oc} ~ 1.2 V vs RHE, respectively. The XPS emissions at binding energies of 854.0±0.2 and 855.8±0.2 eV can be attributed to NiO, $Ni(OH)_2$, and NiO(OH).[20, 21, 37] The photoelectrode held at open circuit displayed a similar Ni $2p_{3/2}$ spectrum to that of the as-deposited NiO_x film, indicating that a mix of nickel oxides was present on both surfaces. In contrast, the XPS data for the photoelectrode after extended day/night cycling revealed an emission at 855.8 eV but no lower energy emission (854.0

eV), indicating an increase in higher oxidation states after cycling.

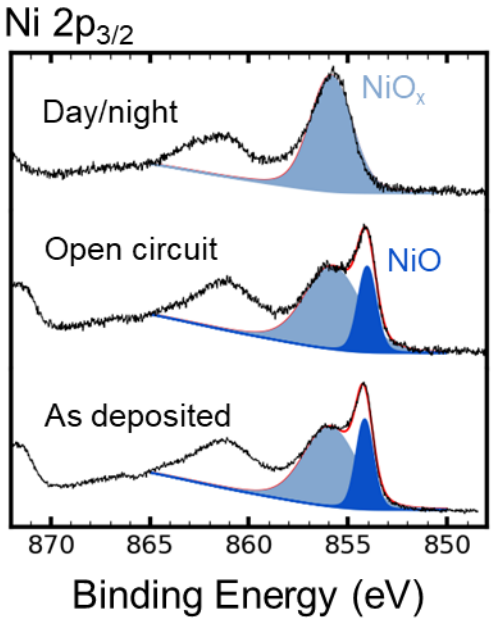

Figure 3.19. X-ray photoelectron spectroscopic data in the Ni $2p_{3/2}$ region of np^+-Si/NiO_x electrodes. Electrodes were measured as deposited, after 20 h in O_2-saturated 1 M KOH(aq) at open circuit, and after 410 h in 1 M KOH(aq) under simulated day/night cycling as described in Fig. 3.14. The Ni $2p_{3/2}$ emission was fitted to two peaks. The dominant phase of the light blue peak is likely a mix of NiO. $Ni(OH)_2$, and NiO(OH) while that of the low energy peak (darker blue) is likely NiO. The y-axis is in arbitrary units.

3.3.6 Operation at Near-neutral pH to Inhibit the Rate of SiO_x Dissolution

Fig. 3.20 displays the dissolution behavior of p^+-Si(100) in O_2-saturated, 0.5 M potassium borate buffer (K-Bi, pH 9.5), with the native oxide of p^+-Si electrodes removed using buffered oxide etch prior to immersing the electrode in K-Bi. Analysis of the electrolyte by inductively coupled plasma mass spectrometry (ICP-MS) showed a negligible rate of Si dissolution for electrodes held either at open circuit or at 1.63 V vs RHE (Fig. 3.20a). A p^+-Si(100) electrode that had been cycled immediately after immersion in K-Bi exhibited an anodic peak indicative of E_{PP} at 0.31 V vs RHE (Fig.

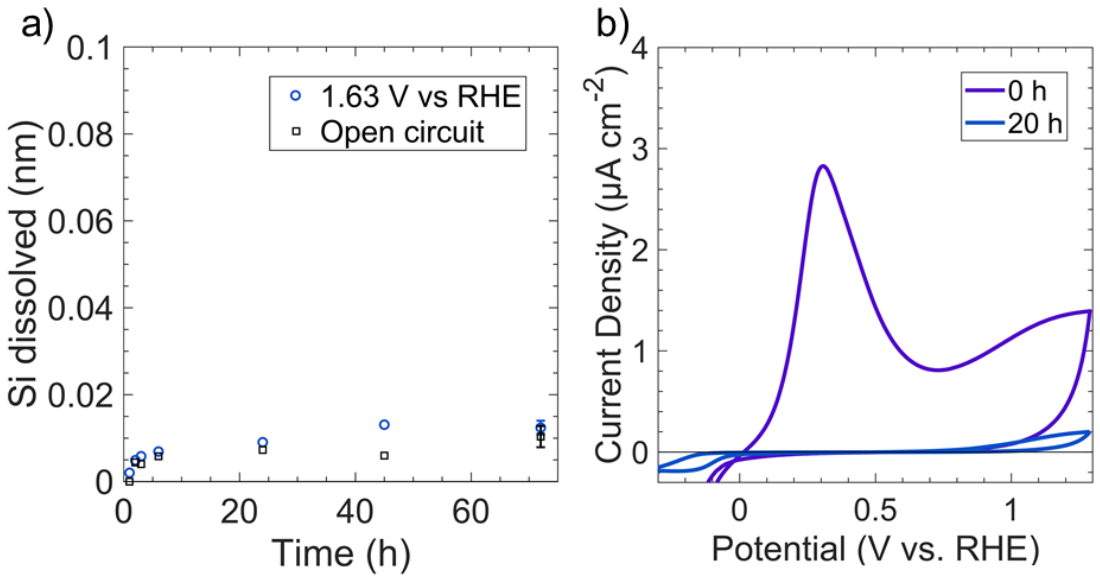

Figure 3.20. Stability of SiO_x in O_2-saturated 0.5 M K-borate buffer (pH 9.5). (a) Si dissolved over time in solution from p^+-Si electrodes at open circuit (black square) and at 1.63 V vs RHE (blue circle) as determined by inductively coupled plasma mass spectrometry. (b) Cyclic voltammograms of p^+-Si electrodes measured either immediately after immersion (purple) or after 20 h at open circuit (blue). The voltammetric scan rate was 1 mV s^{-1}. To remove any native oxide, the electrodes were immersed in buffer oxide etch for 30 s prior to electrochemistry.

3.20b). In contrast, a p^+-Si electrode that was first held for 20 h at open-circuit in K-Bi did not exhibit an anodic peak, suggesting that a self-limited oxide had formed during immersion into the electrolyte (Fig. 3.20b). XPS data confirmed the presence of SiO_x after immersion of p^+-Si in KBi at open circuit for 20 h (Fig. 3.21). A p^+-Si electrode that was similarly immersed in O_2-saturated 1 M KOH(aq) for 20 h did not however exhibit a SiO_2 peak in the Si 2p XPS region, indicating that Si dissolution dominated SiO_x formation in KOH solution, but a relatively stable SiO_x layer instead spontaneously formed at pH 9.5.

Fig. 3.22 compares the performance of an np^+-Si(100)/Ni photoanode under simulated day/night cycling in ambient (~ 0.2 atm O_2) conditions in 0.5 M K-Bi to the behavior under conditions analogous to those used for the KOH solutions. The steady light-

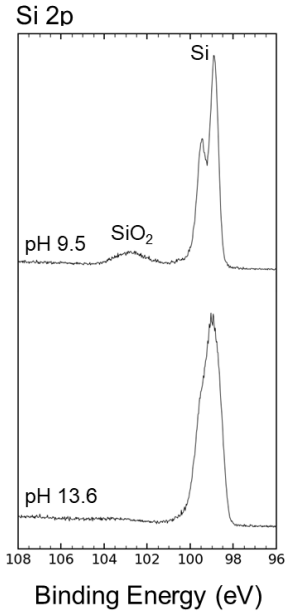

Figure 3.21. XPS data in the Si 2p region of p^+-Si electrodes. Electrodes were measured after 20 h in 1 M KOH(aq) at open circuit in either 1 M KOH(aq) (bottom) or 0.5 M K-borate buffer (top). The electrode was submerged in buffer oxide etch for 30 s to remove any native oxide prior to testing. The y-axis is in arbitrary units.

limited photocurrent density was > 24 mA cm^{-2} throughout the duration of each 120 h experiment. In 1 M KOH(aq), the photoanode exhibited qualitatively similar E_{oc} vs time behavior to that of the np^+-Si/NiO_x photoanode shown in Fig. 3.14, as expected due to the oxidation of surficial Ni to NiO_x. In contrast, in K-Bi, E_{oc} decreased from ~ 1.4 V to ~ 1.0 V vs RHE, followed by a comparatively gradual decline to E_{oc} ~ 0.7 - 0.8 V vs RHE, possibly due to a gradual conversion of Ni(Fe)OOH to NiO/$Ni(OH)_2$. The photoanode exhibited a higher fill factor in 1 M KOH(aq) than in 1.0 M K-Bi(aq), with a ~140 mV negative shift in initial onset potential and a reduction in series resistance from 15 Ω to 7 Ω as the pH was increased. These differences in performance were consistent with the increased overpotentials associated with the OER as the pH was decreased from highly alkaline conditions to near-neutral pH values.[4, 38] In both solutions, the photoanodes

exhibited relatively unchanged voltammetric behavior throughout the 120 h experiment, but substantial changes to the surface morphology were nevertheless evident. Specifically, after cycling in 1 M KOH(aq), the photoanode surface was covered with circular etch pits, whereas no etch pits were observed on the photoanode that had been cycled in 1.0 M K-Bi(aq).

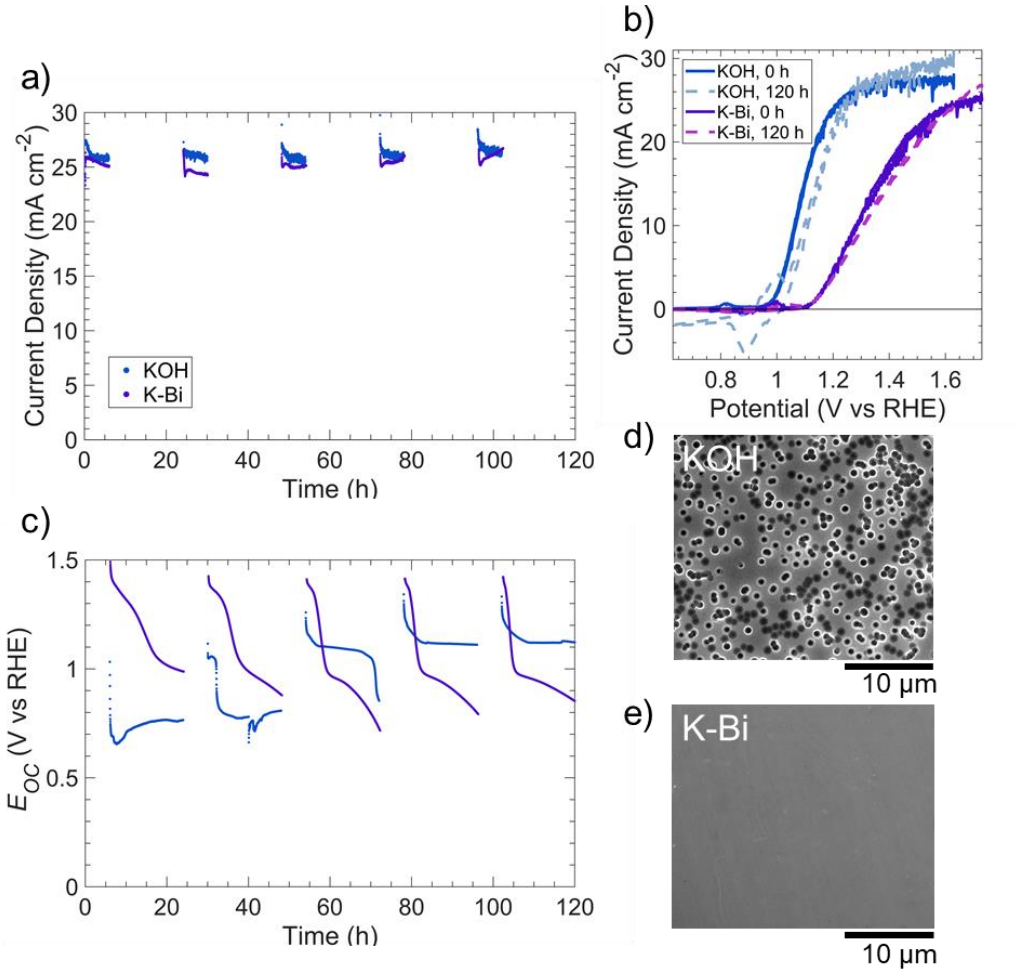

Figure 3.22. Comparison of the performance of np^+-Si(100)/Ni (5 nm) photoelectrodes and of the etching behavior at strongly alkaline pH (1 M KOH(aq)) vs near-neutral pH (0.5 M K-Bi(aq)) for electrodes subjected to cycling between simulated day and night conditions. (a) Chronoamperometric stability in 1 M KOH(aq) (blue) at 1.63 V vs RHE and 0.5 M K-Bi(aq) (purple) at 1.73 V vs RHE. (b) Cyclic voltammetry before (solid line) and after 120 h of testing (dashed line). The voltammogram scan rate was 40 mV s^{-1}. For (a-b), photoelectrodes were under 100 mW cm^{-2} of illumination provided by an ELH-type W-halogen lamp for 6 h intervals, followed by collection of (c) open-circuit potentials of the photoelectrodes for 18 h intervals in the dark. (d-e) Scanning electron micrographs of photoelectrodes after stability tests in (d) 1 M KOH(aq) and (e) 0.5 M K-Bi(aq).

3.4 Discussion

3.4.1 Proposed Mechanism for Catalytic Passivation of Si using Ni-based Films

Si passivation in alkaline media is achieved by poising the surface potential of the Si electrode sufficiently positive of E_{PP} to oxidize any exposed Si. Previous work demonstrated this passivation effect using $[Fe(CN)_6]^{3-}$ as a strong oxidant,[17] whereas this work demonstrates that a Ni-based (or other) coating is sufficient to produce this effect in O_2-saturated alkaline solution. Multiple Ni species (e.g. Ni, NiO, $Ni(OH)_2$, and NiO(OH)) are capable of passivating Si; while the specific Ni species present influences the surface potential of the Si/Ni anode, the potential remains sufficiently positive to maintain Si passivation regardless of the Ni species (Fig. 3.3 and 3.11). The formation of passive oxides on the Si surface at open circuit in O_2-saturated KOH with Ni-based (or other) coatings allows the underlying Si to be protected even if the $Ni(O_x)$ film does not conformally cover the surface. For instance, 3 μm diameter μNi regions led to the passivation of regions of exposed Si that were microns away from the Ni islands (Fig. 3.9).

A combination of a Ni-based thin film and O_2 in solution was required to facilitate Si passivation. Without the $Ni(O_x)$ thin film, the E_{oc} of Si electrodes was ~ -0.1 V vs RHE and thus below the anodic threshold for Si oxidation of E_{PP} = 0.17 V vs RHE (Fig. 3.1). At this potential, the observed inverted pyramid etch pits indicate rapid etching of Si(100) (Fig. 3.3d and 3.6). Without O_2 in the electrolyte, a $Ni(O_x)$ film can initially define the surface potential of the electrode, likely due to the NiO, $Ni(OH)_2$, and NiO(OH) species on the surface, but within a few hours the E_{oc} declined to < E_{PP} and continued decreasing toward the open-circuit potential of Si (Fig. 3.3b). This decline indicates that the surface potential of the electrode is ultimately defined by Si dissolution. Conversely, Si(100)

passivation in the presence of both O_2 and a $Ni(O_x)$ thin film is evident as shown by circular etch pits caused by isotropic SiO_2 etching (Fig. 3.3c) and evidence of SiO_2 at pinholes via XPS after testing (Fig. 3.15).

The surface potential of the Si electrode at open circuit will equilibrate with the solution redox potential only if the solution couple can react at the Si surface. In the case of the O_2/OH^- (E^0 = 1.23 V vs RHE) redox couple, bare Si does not provide a low-energy pathway between the redox species. Thus, for a p^+-Si electrode, the surface potential does not equilibrate with an O_2-saturated 1 M KOH solution at open circuit. However, when the surface potential is controlled by a catalyst on the surface (p^+-Si/$Ni(O_x)$), the potential responds to the presence of the O_2 in the KOH(aq) solution.

The surface potential of p^+-Si/$Ni(O_x)$ electrodes is controlled by three factors: the redox couples within the NiO_x film; interactions with solution redox couples; and dissolution of the bare Si. The K_{sp} of $Ni(OH)_2$ is ~ 10^{-15}, so in strongly alkaline electrolytes only trace amounts of $Ni(aq)^{2+}$ are present and solution Ni redox couples are not important.[39] For a p^+-Si/$Ni(O_x)$ electrode under illumination or under anodic conditions, the Ni surface became more oxidized (Fig. 3.17). However, without O_2 in the electrolyte, the Ni species on the surface of Si/$Ni(O_x)$ electrode did not prevent the E_{oc} from decreasing to a value close to that of a bare Si electrode, below E_{PP} (Fig. 3.3). Thus, for a p^+-Si/$Ni(O_x)$ electrode, the Ni solid-state redox couples alone did not dominate the electrode potential relative to Si dissolution. For p^+-Si/$Ni(O_x)$ in an O_2-rich solution, the interactions between the $Ni(O_x)$ on the surface of the electrode and the solution O_2/OH^- couple define the surface potential of the Si electrode, likely involving the oxidation and reduction of Ni species on the electrode surface.

When O_2 is not present in the solution, few or no solution redox species are present. The solution potential is therefore largely undefined and cannot buffer the electrode potential despite the presence of a Ni(O_x) catalytic layer. Rather, the surface potential of the electrode is largely defined by Si oxidative dissolution, and as a result, the E_{oc} of the electrode rapidly decreases to negative of E_{PP}.

The above observations suggest a correlation between the catalytic activity of the overlayer and Si passivation (Fig. 3.10c and 3.13). This expectation is supported by the passivation of Si that was observed for p^+-Si/Pt films in O_2-saturated solutions (Fig. 3.12a-b). The data are consistent with a model in which Si/Pt and Si/Ni surfaces are in communication with the O_2/OH^- solution couple. However, this simple correlation is not observed for Si covered by Co. The behavior of the Si/Co surfaces is consistent with complete air oxidation of the Co layer resulting in an electrically nonconductive overlayer,[40] that precludes effective redox-catalyzed communication with the dissolved O_2 to maintain the surface potential of the Si positive of E_{PP}.

The Si/TiO_2 surface is also electrically nonconductive, and hence leads to etching of the Si.[41] The Si/TiO_2/Ni interface has a buried Si surface, so changes in solution potential affect the Ni but do not affect the buried Si/TiO_2 junction nor affect the surface potential of the Si.[42]

3.4.2 Assessing and Mitigating SiO_x Dissolution

Although open-circuit Si passivation can extend device lifetimes by hundreds of hours for photoanodes subjected to day/night cycling in KOH solution,[17] the gradual dissolution of SiO_x will ultimately limit the overall device lifetime.[13] Furthermore, the rate

of SiO_x dissolution is influenced by the surface potential of the Si that results from day and night conditions. Given the monotonic increase of the SiO_x dissolution rate for potentials > 0.5 V vs RHE (Fig. 3.2a), the day cycle when the potential is held at 1.63 V vs RHE produces a larger etch rate than the night cycle, which results in a surface potential at the rest potential for the electrode in the dark. For a Si/Ni photoanode, the open-circuit potential shifted from E_{oc} ~ 0.7 V vs RHE (night) to ≥ 1.5 V vs RHE (day) (Fig. 3.22c). Consequently, Si/Ni photoanodes undergoing day/night cycling exhibited more rapid SiO_x etching (Fig. 3.22d) than Si/Ni electrodes held at open circuit (Fig. 3.8), as shown by the 1010±70 nm and 380±40 nm diameter etch pits, respectively.

Several strategies have potential to further inhibit the dissolution rate of SiO_x and extend the lifetime of the oxide-coated photoanodes. In one approach, the photoanode could be held at less positive operating potentials during the day cycles. For instance, an np^+-Si/Ni photoanode in 1 M KOH(aq) (Fig. 3.22b) approaches the light-limited photocurrent density at an applied potential of ~ 1.2 V vs RHE rather than at 1.6 V vs RHE. Consequently, operating at a less positive potential during the day cycles could inhibit the dissolution of the SiO_x (Fig. 3.2a). The oxide grown electrochemically could potentially be post-processed to a denser, more slowly dissolving oxide by thermal treatment, or could potentially be converted chemically to more inert materials such as Si nitrides, oxynitrides, carbides, or oxycarbides.

Operating the photoelectrode at pH 9.5 can also substantially inhibit dissolution of SiO_x (Fig. 3.20), although the lower pH introduces performance limitations due to increases in polarization losses and increased kinetic overpotentials for the OER. Additionally, the oxidized Ni film is partially soluble in K-Bi, and the associated loss of catalyst might

consequently deleteriously reduce the device lifetime.[43] The work herein clearly provides a systematic understanding of the durability of photoelectrodes by identifying the medium-term failure modes and mechanisms and then rationally implementing steps to mitigate the corrosion processes of concern.

3.5 Conclusions

Coating of Si with Ni or NiO_x thin films prevented rapid Si dissolution in O_2 saturated strongly alkaline electrolytes subjected to dark, open-circuit conditions. The combination of a Ni/NiO_x catalyst and O_2 in the electrolyte maintained the Si surface potential at > 0.6 V vs RHE, positive enough to catalyze the growth of SiO_x on the Si surface at a rate faster than its dissolution. The O_2 in the electrolyte plays an important role in driving the kinetics for Si passivation. Without O_2 in the electrolyte the surface potential was defined predominantly by Si dissolution (~ -0.1 V vs RHE).

An np^+-Si/NiO_x photoanode undergoing day/night cycling exhibited stable performance for > 408 h. The catalyzed passivation process reduced the rate of corrosion of exposed Si at pinholes in the NiO_x film. Catalytic passivation of Si was observed with multiple phases of Ni – Ni, NiO, $Ni(OH)_2$, and NiOOH – as well as with Pt. Although Si-based photoanodes are susceptible to eventual failure due to slow SiO_x dissolution and subsequent undercutting of the protective film, this effect can be circumvented by leveraging the thermodynamic stability of SiO_2 in pH 9.5 at the expense of an increased resistance and positive shifts in the onset potential. This work underscores the ability of well-established Si photoanode configurations to withstand rapid corrosion associated with patterns of diurnal insolation. Moreover, the work demonstrates the benefits of a systematic

approach to increase the durability of photoelectrodes by identifying the dominant failure modes of the device and taking rational steps to mitigate such processes.

3.6 References

1. M. X. Tan, P. E. Laibinis, S. T. Nguyen, J. M. Kesselman, C. E. Stanton and N. S. Lewis, in *Progress in Inorganic Chemistry*, 1994, pp. 21-144.
2. D. Bae, B. Seger, P. C. Vesborg, O. Hansen and I. Chorkendorff, *Chem Soc Rev*, 2017, **46**, 1933-1954.
3. S. Hu, M. R. Shaner, J. A. Beardslee, M. Lichterman, B. S. Brunschwig and N. S. Lewis, *Science*, 2014, **344**, 1005-1009.
4. M. J. Kenney, M. Gong, Y. Li, J. Z. Wu, J. Feng, M. Lanza and H. Dai, *Science*, 2013, **342**, 836-840.
5. K. Sun, M. T. McDowell, A. C. Nielander, S. Hu, M. R. Shaner, F. Yang, B. S. Brunschwig and N. S. Lewis, *The Journal of Physical Chemistry Letters*, 2015, **6**, 592-598.
6. K. Sun, F. H. Saadi, M. F. Lichterman, W. G. Hale, H. P. Wang, X. Zhou, N. T. Plymale, S. T. Omelchenko, J. H. He, K. M. Papadantonakis, B. S. Brunschwig and N. S. Lewis, *Proc Natl Acad Sci U S A*, 2015, **112**, 3612-3617.
7. X. Zhou, R. Liu, K. Sun, D. Friedrich, M. T. McDowell, F. Yang, S. T. Omelchenko, F. H. Saadi, A. C. Nielander, S. Yalamanchili, K. M. Papadantonakis, B. S. Brunschwig and N. S. Lewis, *Energy & Environmental Science*, 2015, **8**, 2644-2649.
8. X. Zhou, R. Liu, K. Sun, K. M. Papadantonakis, B. S. Brunschwig and N. S. Lewis, *Energy & Environmental Science*, 2016, **9**, 892-897.
9. P. Buabthong, Z. P. Ifkovits, P. A. Kempler, Y. Chen, P. D. Nunez, B. S. Brunschwig, K. M. Papadantonakis and N. S. Lewis, *Energy & Environmental Science*, 2020, **13**, 4269-4279.
10. D. Bae, S. Shayestehaminzadeh, E. B. Thorsteinsson, T. Pedersen, O. Hansen, B. Seger, P. C. K. Vesborg, S. Ólafsson and I. Chorkendorff, *Sol. Energy Mater. Sol. Cells*, 2016, **144**, 758-765.
11. M. R. Shaner, S. Hu, K. Sun and N. S. Lewis, *Energy & Environmental Science*, 2015, **8**, 203-207.
12. H. G. G. Philipsen and J. J. Kelly, *The Journal of Physical Chemistry B*, 2005, **109**, 17245-17253.
13. K. Sun, Nicole L. Ritzert, J. John, H. Tan, W. G. Hale, J. Jiang, I. Moreno-Hernandez, K. M. Papadantonakis, T. P. Moffat, B. S. Brunschwig and N. S. Lewis, *Sustainable Energy & Fuels*, 2018, **2**, 983-998.
14. K. Oh, C. Mériadec, B. Lassalle-Kaiser, V. Dorcet, B. Fabre, S. Ababou-Girard, L. Joanny, F. Gouttefangeas and G. Loget, *Energy & Environmental Science*, 2018, **11**, 2590-2599.
15. P. M. M. C. Bressers, S. A. S. P. Pagano and J. J. Kelly, *Journal of Electroanalytical Chemistry*, 1995, **391**, 159-168.

16. X. H. Xia and J. J. Kelly, *Electrochimica Acta*, 2000, **45**, 4645-4653.
17. H. J. Fu, I. A. Moreno-Hernandez, P. Buabthong, K. M. Papadantonakis, B. S. Brunschwig and N. S. Lewis, *Energy & Environmental Science*, 2020, **13**, 4132-4141.
18. D. R. Lide, *CRC handbook of chemistry and physics*, CRC press, 2004.
19. S. Hu, N. S. Lewis, J. W. Ager, J. Yang, J. R. McKone and N. C. Strandwitz, *The Journal of Physical Chemistry C*, 2015, **119**, 24201-24228.
20. M. C. Biesinger, B. P. Payne, L. W. M. Lau, A. Gerson and R. S. C. Smart, *Surface and Interface Analysis*, 2009, **41**, 324-332.
21. A. P. Grosvenor, M. C. Biesinger, R. S. C. Smart and N. S. McIntyre, *Surface Science*, 2006, **600**, 1771.
22. P. M. M. C. Bressers, J. J. Kelly, J. G. E. Gardeniers and M. Elwenspoek, *J. Electrochem. Soc.*, 1996, **143**, 1744-1750.
23. O. J. Glembocki, R. E. Stahlbush and M. Tomkiewicz, *Journal of The Electrochemical Society*, 1985, **132**, 145-151.
24. J. W. Faust and E. D. Palik, *Journal of The Electrochemical Society*, 1983, **130**, 1413-1420.
25. W. A. Pliskin and H. S. Lehman, *Journal of The Electrochemical Society*, 1965, **112**, 1013-1019.
26. P. Allongue, V. Costa-Kieling and H. Gerischer, *Journal of The Electrochemical Society*, 1993, **140**, 1018.
27. L.-A. Stern and X. Hu, *Faraday Discussions*, 2014, **176**, 363-379.
28. L. Trotochaud, S. L. Young, J. K. Ranney and S. W. Boettcher, *Journal of the American Chemical Society*, 2014, **136**, 6744-6753.
29. L. F. Huang, M. J. Hutchison, R. J. Santucci, J. R. Scully and J. M. Rondinelli, *The Journal of Physical Chemistry C*, 2017, **121**, 9782-9789.
30. O. Diaz-Morales, D. Ferrus-Suspedra and M. T. M. Koper, *Chemical Science*, 2016, **7**, 2639-2645.
31. M. Hannula, H. Ali-Löytty, K. Lahtonen, E. Sarlin, J. Saari and M. Valden, *Chemistry of materials : a publication of the American Chemical Society*, 2018, **30**, 1199-1208.
32. S. Sui, X. Wang, X. Zhou, Y. Su, S. Riffat and C.-j. Liu, *Journal of Materials Chemistry A*, 2017, **5**, 1808-1825.
33. P. Yin, T. Yao, Y. Wu, L. Zheng, Y. Lin, W. Liu, H. Ju, J. Zhu, X. Hong, Z. Deng, G. Zhou, S. Wei and Y. Li, *Angewandte Chemie International Edition*, 2016, **55**, 10800-10805.
34. H. Abroshan, P. Bothra, S. Back, A. Kulkarni, J. K. Nørskov and S. Siahrostami, *The Journal of Physical Chemistry C*, 2018, **122**, 4783-4791.
35. A. Andersson, W. Estrada, C.-G. Granqvist, A. Gorenstein and F. Decker, *Characterization of electrochromic dc-sputtered nickel-oxide-based films*, SPIE, 1990.
36. D. S. Jensen, S. S. Kanyal, N. Madaan, M. A. Vail, A. E. Dadson, M. H. Engelhard and M. R. Linford, *Surface Science Spectra*, 2013, **20**, 36-42.
37. M. C. Biesinger, B. P. Payne, A. P. Grosvenor, L. W. M. Lau, A. R. Gerson and R. S. C. Smart, *Applied Surface Science*, 2011, **257**, 2717-2730.

38. M. R. Singh, K. Papadantonakis, C. Xiang and N. S. Lewis, *Energy Environ. Sci*, 2015, **8**, 2760-2767.
39. S. V. Mattigod, D. Rai, A. R. Felmy and L. Rao, *Journal of Solution Chemistry*, 1997, **26**, 391-403.
40. L. Smardz, U. Köbler and W. Zinn, *Journal of Applied Physics*, 1992, **71**, 5199-5204.
41. P. Nunez, M. H. Richter, B. D. Piercy, C. W. Roske, M. Cabán-Acevedo, M. D. Losego, S. J. Konezny, D. J. Fermin, S. Hu, B. S. Brunschwig and N. S. Lewis, *The Journal of Physical Chemistry C*, 2019, **123**, 20116-20129.
42. M. H. Richter, W.-H. Cheng, E. J. Crumlin, W. S. Drisdell, H. A. Atwater, D. Schmeißer, N. S. Lewis and B. S. Brunschwig, *Chemistry of Materials*, 2021, **33**, 1265-1275.
43. K. Sun, R. Liu, Y. Chen, E. Verlage, N. S. Lewis and C. Xiang, *Advanced Energy Materials*, 2016, **6,** 1600379.

Chapter 4

NAFION-PEDOT:PSS COMPOSITE MEMBRANES FOR APPLICATIONS IN PHOTOELECTROCHEMICAL DEVICES

4.1 Introduction

Driving unassisted photoelectrochemical (PEC) water splitting at > 10 mA cm^{-2} current density requires two light absorbers electrically connect in series in order to satisfy the required ~ 1.7 V voltage threshold.[1-3] Planar tandem devices have demonstrated efficient unassisted water splitting, however their scalability to larger electrode areas is limited due to solution resistance losses and susceptibility to corrosion.[4, 5] One proposed approach to scalable device design involves micro- and nano-structured arrays of semiconductor materials embedded in a flexible, ion-exchange membrane scaffold.[6, 7] For instance, Si microwire arrays have been shown to efficiently capture light and evolve hydrogen in acidic electrolyte while embedded in the proton exchange membrane Nafion.[8, 9] The μm-scale spacing between microwires minimizes lateral electrolyte-based resistive losses, while high aspect ratio wires enable strategic placement of catalysts to minimize parasitic absorption.[10, 11] Microwire arrays coated with a protective layer have also demonstrated excellent stability in corrosive electrolyte;[12] corrosion at pinholes on the protection layer is self-limiting because they do not propagate to adjacent wires.[13, 14] Two membrane-embedded micro- or nanowire arrays can be laminated together to form a tandem, evolving H_2 on one side of the device and O_2 on the other. The membrane scaffold allows for ion conduction between each side and prevents product gas crossover.[15] However, the scaffold is also electrically insulating, necessitating an electrically conductive interlayer that connects each wire array in series without disrupting ion conduction. The intermediary layer must possess both electron and ion conductivity while

also maintaining the desirable characteristics of the membrane scaffold. For instance, this layer must be optically transparent to pass light to the bottom array, chemically stable in acidic (or alkaline) electrolyte, and able to maintain adhesion to both the wire backsides and the membrane scaffold.

Poly(3,4-ethylenedioxythiophene) polystyrene sulfonate (PEDOT:PSS) is a conductive polymer mixture that has been widely used in the energy conversion and storage field as a hole transport layer.[16] For PEC application, PEDOT:PSS has been used as an electrical interconnect to p-Si and n^+-Si wires.[17, 18] The sulfonate groups within the PSS enhances the dispersibility of the electrically conductive PEDOT in water, and additionally can uptake and conduct H^+ ions across a solution casted film.[19] While a PEDOT:PSS interlayer between two Nafion-embedded Si wire arrays has been demonstrated,[8] the resulting PEDOT:PSS film blocked light from reaching the bottom array due to absorption by polaron and bipolaron states.[20] In most thin film application, PEDOT:PSS has been processed to be ~ 100 nm in order to achieve 90% transparency.[16] However, rough features of membrane-embedded wire backsides preclude conformal PEDOT:PSS processing at this thickness. Furthermore, differing mechanical properties between Nafion and PEDOT:PSS such as the extent of swelling in electrolyte requires further characterization.[21, 22]

Inheriting the desirable properties of both Nafion and PEDOT:PSS can be achieved via a composite of the polymers. A composite can be fabricated with ease because Nafion and PEDOT:PSS together is solution dispersible since both PSS and Nafion possess sulfonate groups. The work herein characterizes Nafion-PEDOT:PSS composites for applications as an interlayer used with membrane-embedded wire array PEC devices.

Nafion-PEDOT:PSS have been previously explored for PEC applications,[23] however the structure-property relationships of Nafion-PEDOT:PSS were not well characterized and the percolation threshold of PEDOT (~ 10% by weight) precluded the use of highly dilute (< 1 wt%) PEDOT:PSS. In contrast, this work demonstrates that the addition of dimethyl sulfoxide (DMSO) as a co-solvent changes the size of PEDOT domains dispersed in Nafion/PSS, thereby increasing conductivity by orders of magnitude by reducing the percolation threshold to ~ 0.5 wt% PEDOT:PSS. Furthermore, low resistance contact to Si was achieved using the DMSO-treated, Nafion-PEDOT:PSS composite on CH_3-terminated p^+-Si.

4.2 Materials and Methods

4.2.1 Chemicals and Materials

Chemicals were used as received unless otherwise stated, including Clevios PH 1000 PEDOT:PSS (Heraeus), Nafion D-521 (Alfa Aesar, 5 wt% in water and isopropanol), Nafion 115 (Chemours), *N*,*N*-dimethylformamide (DMF, Sigma-Aldrich, ACS grade), dimethyl sulfoxide (DMSO, Sigma-Aldrich, ACS grade), and sulfuric acid (H_2SO_4, Macron Fine Chemicals, AR grade). Boron-doped, (111)-oriented p-Si (0.1-1.0 Ω cm resistivity) and phosphorous doped, (111)-oriented n-Si (0.1-1.0 Ω cm resistivity) were purchased from Addison Engineering, Inc. The Si cleaning and etching materials include hydrochloric acid (HCl, EMD Millipore Co., 36.5-38%), hydrogen peroxide (H_2O_2, EMD Millipore Co., 30%), and buffered oxide etchant (BOE, 6:1 ammonium fluoride to hydrofluoric acid, Transene Company, Inc.). Materials used for photolithography include photoresist (Shipley 1813), MCC primer 80/20 (Microchem Corp.), and MF-319 developer (Microchem Corp.). Phosphorous pentachloride (PCl_5, ≥99.998% metal basis, Alfa Aesar),

chlorobenzene (anhydrous, ≥99.8% Sigma-Aldrich), tetrahydrofuran (THF, anhydrous, inhibitor-free, ≥99.9% Sigma-Aldrich), and methylmagnesium chloride (CH_3MgCl, Sigma-Aldrich) were used for methyl functionalization on Si. Ag paint (Ted Pella, Inc.), gallium-indium eutectic (Alfa Aesar, 99.99%), and epoxy (Gorilla) were used during electrode preparation. Deionized water (resistivity ρ > 18.2 MΩ cm) was obtained from a Barnstead Millipore purification system.

4.2.2 Nafion-PEDOT:PSS Composite and Si Preparation

Nafion-PEDOT:PSS composites were prepared by mixing dispersions of Nafion (5 vol% in water/IPA) and PEDOT:PSS (1.2 vol% in water) at set ratios. For instance, a 2:1 ratio by volume of Nafion to PEDOT:PSS yielded a 11.4 wt% PEDOT:PSS film. Unless otherwise stated, 10 vol% DMSO was added as a co-solvent to the Nafion-PEDOT:PSS dispersion. Additional water was then added until the polymer to volume ratio was ~ 24 g/L. The resulting mixture was mixed with a vortex mixer for 5 min and then sonicated for an additional 10 min. The composite dispersion was cast onto a substrate using a spin coater at 350 rpm for 1 min. The composite was then cured on a hot plate at 150 ˚C for 5 min to access the glass transition temperature of Nafion.[24] The resulting film was ~ 1 μm thick as measured using a profilometer (Bruker DektakXT Stylus profilometer).

Silicon microwires were fabricated using deep reactive ion etching (RIE) as described in a previous report.[10] Briefly, >120 nm thick Al_2O_3 masks with 3 μm diameter and 7 μm pitch circular islands were patterned using standard photolithography procedures followed by E-Beam evaporation of Al_2O_3. Si etching was performed using a SF_6/O_2 plasma (Oxford DRIE 100 ICP-RIE system) at -130 ˚C. The Al_2O_3 was removed using a

RCA2 clean, consisting of 6:1:1 H_2O:HCl:H_2O_2 at 75 ˚C for 15 min. Prior to infilling the wire arrays with Nafion, a Nafion dispersion in DMF was prepared by adding 1.2 mL of DMF to 3.0 mL of the as received Nafion, followed by heating at 140 ˚C to evaporate the water/IPA mixture until the solution volume reached ~ 1.2 mL. The resulting Nafion dispersion was cast onto the microwire array using a spin coater at 1000 rpm for 1 min, followed by heating at 150 ˚C for ~ 20 min. The Nafion-embedded wire array was removed from the Si surface using a razor blade, producing a freestanding structure. Nafion-embedded Si wire arrays were affixed upside down to a sample chuck using Cu tape so that the backside was facing upwards. The surface was examined via scanning electron microscopy (SEM) using a Phenom Pro electron microscope (Phenom World).

Fabrication of CH_3-terminated Si surfaces was described in a previous report.[25] Briefly, p-Si(111) was cleaved into ~ 1 cm^2 pieces and was RCA2 cleaned (6:1:1 H_2O:HCl:H_2O_2) at 75 ˚C, followed by submerging in BOE for 30 s then in Ar-purged 11 M NH_4F(aq) for 9 min to produce a H-terminated surface. The Si was dried with N_2, transferred into a N_2-purged flushbox, and chlorinated at 80 ˚C in a saturated solution of PCl_5 in anhydrous chlorobenzene for 45 min. Afterwards, the Si was rinsed sequentially in chlorobenzene followed by anhydrous THF. Cl-terminated Si was methylated at 50 ˚C in 3.0 M CH_3MgCl in THF for 24 h, followed by rising in THF.

Either n- or p-Si/polymer electrodes were prepared by scratching the backside with In-Ga eutectic to form a low resistance contact and affixed to a Cu substrate using Ag-paint. The sides of the electrodes were sealed with epoxy and left to dry. For Si wafers without a CH_3-terminated surface, H-termination was introduced by submerging the

surface in BOE for 30 s. The corresponding polymer dispersion was drop casted onto the surface and the sample was cured in a vacuum oven at 150 ˚C.

4.2.3 Characterization

The optical transmittance of Nafion-PEDOT:PSS films were determined using UV-vis spectroscopy with an integrating sphere (Agilent Cary 5000). Prior to measuring, 1 µm thick films were cast and heated on a transparent quartz substrate.

Transverse ion conductivity was measured using a DC, four-electrode setup.[8, 26] Prior to measurement, membranes were hydrated by submerging in 0.6 M H_2O_2(aq) at 80 ˚C for 2 h, followed by 1.0 M H_2SO_4(aq) overnight. A hydrated membrane was then sealed with gaskets between two compartments of an acrylic cell, leaving 8 mm^2 of the membrane area exposed to each compartment. The cell was then filled with 2.0 M H_2SO_4(aq). Two Pt mesh electrodes were placed in opposite compartments and two Ag/AgCl reference electrodes were each positioned so that the distance between the frit and the membrane surface was ~ 2 mm on each side. A potential sweep from -50 mV to 50 mV was performed at 25 mV s^{-1} at room temperature (20 ˚C) using an MPG-2 potentiostat. The cell resistance (R_{cell}) was extracted from the slope of the resulting linear potential-current measurement. Similarly, the electrolyte resistance ($R_{electrolyte}$) was measured with the same setup without the membrane separating the two compartments. The membrane resistance ($R_{membrane}$) was then calculated with $R_{membrane} = R_{cell} - R_{electrolyte}$ and the ion conductivity (σ_i) was calculated with $\sigma_i = LR_{membrane}^{-1}A^{-1}$, where L is the thickness of the membrane and A is the exposed membrane area.

Lateral conductivity was determined using a four-point probe method. A borosilicate glass substrate was patterned with ~ 100 nm Au using E-beam evaporation through a shadow mask. The resulting pattern showed four 1 mm x 16 mm Au strips spaced 1 mm apart. Kapton polyimide tape was applied on either ends so that 6 mm of each Au strip was exposed. The composite was cast onto the surface, heated, and the tape was removed. Four micromanipulators were used to make contact with one exposed end of each Au strip. The micromanipulators were connected to an MPG-2 potentiostat (Bio-Logic Science Instruments) and the potential was swept from -50 mV to 50 mV at 25 mV s^{-1} in order to find the current-voltage characteristics. Lateral conductivity (σ_L) was found via the equation

$$\sigma_L = \frac{I}{4.53Vt}$$

where I is current, V is voltage, and t is composite film thickness as measured by profilometry.

Atomic force microscopy (AFM) was performed using a Dimension Icon AFM (Bruker). Prior to measuring, composites were cast onto an Au-coated glass substrate. In order to measure current maps, both PeakForce Tunneling AFM (PF-TUNA) and DataCube were performed using a PtIr-coated probe (PFTUNA) with a 25 nm nominal tip radius. During the scan, the PeakForce setpoint was 16 nN, the scan rate was 0.501 Hz, and the PeakForce amplitude was set to 150 nm. The current map was measured at 0.5 V applied potential. DataCube was performed with a 200 ms hold segment corresponding to a potential sweep from -500 mV to 500 mV.

X-ray photoelectron spectroscopy (XPS) was performed using a Kratos Axis Ultra system using a monochromatic Al Kα source to irradiate polymer samples with 1486.7 eV

X-rays at 450 W. The analysis chamber was held at a base pressure of 1 x 10^{-9} Torr. High-resolution spectra were acquired at a resolution of 25 meV with a pass energy of 10 eV. The C 1s and F 1s peak positions were analyzed using CasaXPS computer software. A relative sensitivity factor of 4.34 was used to estimate the F/C ratios. Ultraviolet photoelectron spectroscopy (UPS) data was collected immediately after film deposition prior to the XPS spectra with a 21.2 eV He (I) excitation and a pass energy of 5 eV.

Si(111)/polymer current-voltage characterization and Mott-Schottky analysis were conducted using a SP-200 potentiostat (Bio-Logic Science Instruments). The Cu substrate was used as a back contact while a small Hg drop was used as a top contact on the polymer surface. Current-voltage measurements were taken by cycling between -1.0 and 1.0 V at a scan rate of 0.1 V s^{-1}. Contact resistance between semiconductor and polymer was estimated from the slope of the line, given that bulk resistance and contact resistance to Hg were both found to be negligible. Impedance measurements were obtained over a 3 - 3 x 10^6 Hz range with an applied voltage from 0 to 0.8 V in 0.1 V intervals. The data was fitted to a simple parallel RC circuit with series resistance. The barrier height (Φ_b) was obtained using the Mott-Schottky equation:

$$C^{-2} = \frac{2}{q\varepsilon\varepsilon_0 N_D A^2}\left(V + V_{bi} - \frac{k_B T}{q}\right)$$

$$\Phi_b = V_{bi} - \frac{k_B T}{q}\ln\left(\frac{N_D}{N_C}\right)$$

where C is capacitance, q is electron charge, ε is Si dielectric constant, ε_0 is permittivity of vacuum, N_D is the dopant density, A is electrode area, V is applied voltage, V_{bi} is built-in voltage of the Si/polymer junction, k_B is Boltzmann's constant, T is absolute temperature, and N_C is effectivity density of states in the Si conduction band.

4.3 Results and Discussion

4.3.1 Surface Roughness of Nafion-embedded Si Microwire Backside

The thickness of the composite interlayer is a key parameter that affects multiple aspects of device integration, notably optical transmission, charge transport, and mechanical adhesion. For instance, in order to adhere and form an intimate contact to the backsides of two membrane-embedded, micro-structured semiconductor arrays, the composite interlayer must match or preferably exceed the feature size of each backside of the embedded arrays. Figure 4.1 depicts the surface roughness of an embedded Si microwire array backside, with the atomic force microscope (AFM) image having an average surface roughness (R_a) of 180 nm. In order to accommodate this surface roughness

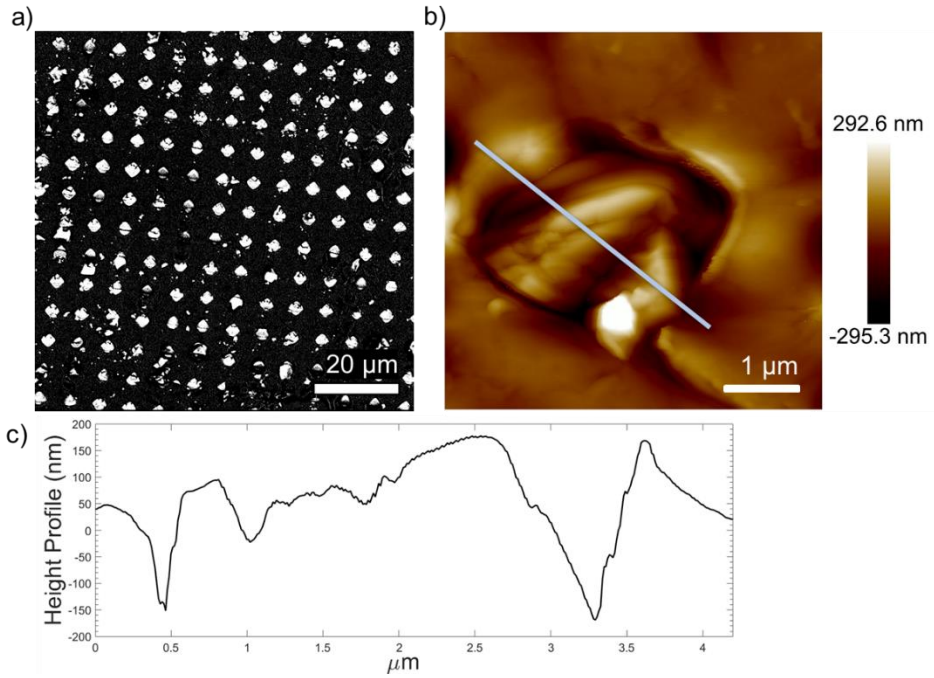

Figure 4.1. Backside of Si microwire arrays embedded in Nafion membrane. (a) Scanning electron micrograph and (b) atomic force microscope (AFM) image of the backside, depicting individual wires protruding from the surface. (c) Height profile of a protruding wire taken as a cross-section of the AFM image (light blue line).

for both sides of the composite interlayer, a 1 µm thickness therefore represents a reasonable standard used for all subsequent bulk property characterization, unless otherwise stated.

4.3.2 Optical Transmittance of Nafion-PEDOT:PSS Composite Films

Fig. 4.2 depicts the UV-visible transmittance of 1 µm thick PEDOT:PSS and Nafion-PEDOT:PSS composites. Transmittance was integrated either across the entire spectrum measured (280-1300 nm) or across the wavelengths Si would absorb in an ideal tandem device in which the Si bottom cell absorbs 50% of the power from higher wavelength solar radiation. PEDOT:PSS films exhibited 42% and 35% integrated transmittance, respectively, due to PEDOT:PSS absorbing more strongly in the higher wavelength ranges relevant to Si as a bottom cell. This observation underscores the need

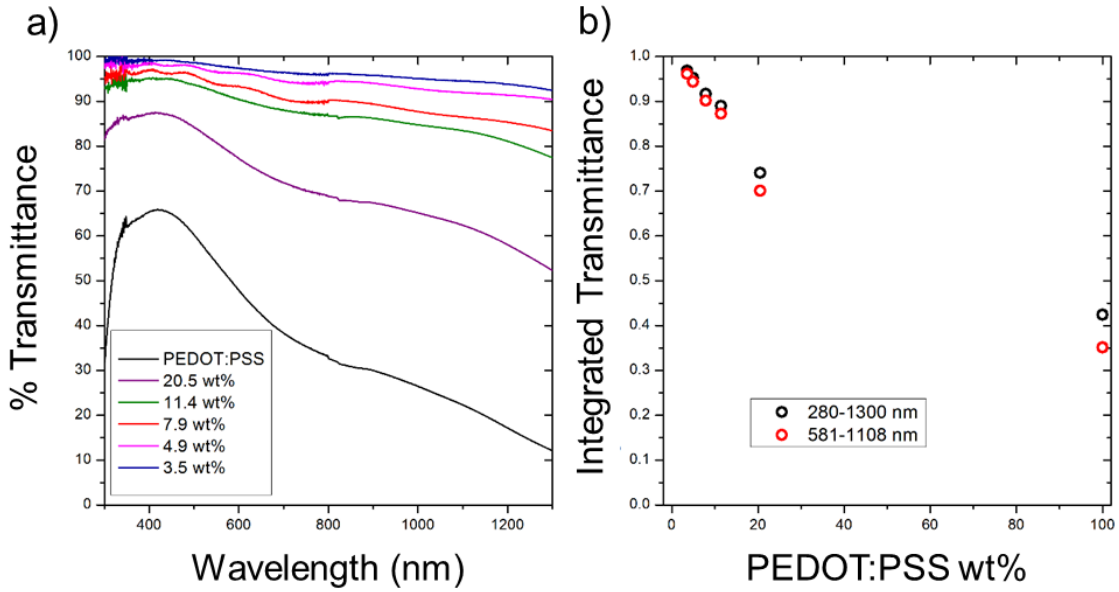

Figure 4.2. Transmittance of Nafion-PEDOT:PSS composites. (a) UV-visible spectrum of 1 µm thick composite films consisting of 100 wt% (black), 20.5 wt% (purple), 11.4 wt% (green), 7.9 wt% (red), 4.9 wt% (pink), and 3.5 wt% (blue) PEDOT:PSS. (b) Integrated, normalized transmittance across the entire scan (black) and at wavelengths relevant those absorbed by Si as a bottom cell light absorber in a tandem (red).

to dilute PEDOT:PSS in a composite structure in order to mitigate parasitic absorption in an integrated PEC cell. Composites that were predominantly Nafion (> 88 wt%) were generally much more transmissive with less disparity in transmittance across different wavelength ranges. For instance, composites with 11.4 wt% PEDOT:PSS exhibited an integrated transmittance of 89% and 87% for the wavelength ranges 280-1300 nm and 581-1108 nm, respectively.

4.3.3 Ion Conductivity of Nafion-PEDOT:PSS Composite Films

Fig. 4.3 shows that Nafion-PEDOT:PSS composites with 0 wt% (Nafion 115), 3.5 wt%, and 11.4 wt% PEDOT:PSS have a transverse ion conductivity (σ_i) of 66±5, 26, and 23 mS cm^{-1}, respectively, in 2.0 M H_2SO_4(aq). The value obtained for Nafion 115 was consistent with similar measurements of Nafion.[27] The lower conductivity found in the composite membranes likely originates from interactions of the sulfonate groups found in Nafion with the introduced PEDOT and PSS; the subsequent disruption of channels could

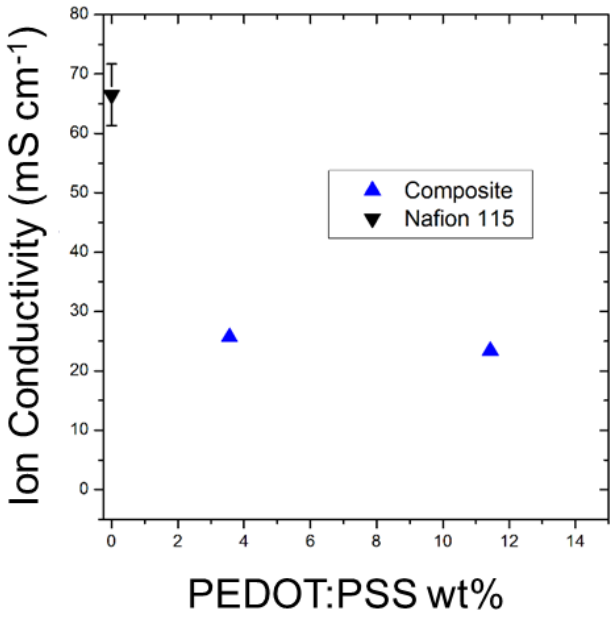

Figure 4.3. Ion conductivity, σ_i, of Nafion 115 (black) and Nafion-PEDOT:PSS (blue) composites in 2.0 M H_2SO_4(aq).

impair proton conduction. Despite the compromise in conductivity, both of the composites tested lead to a negligible voltage drop ~ 4 μV associated with ion conduction assuming a 1 μm thick film operating at 10 mA cm^{-2}.

4.3.4 Electrical Conductivity and Associated Morphology of Composite Films

Fig. 4.4 shows the effect of adding dimethyl sulfoxide (DMSO) as a co-solvent on the lateral, in-plane conductivity (σ_L) of Nafion-PEDOT:PSS composites. Polar solvents such as DMSO have widely been used to enhance the conductivity of PEDOT:PSS films by a factor of ~ 10^3.[19] 10 vol% of DMSO was added to the dispersion prior to casting the Nafion-PEDOT:PSS film. A > 10^4 times enhancement was generally observed and the extent of enhancement was greater with increasing PEDOT concentration. For instance, the lateral conductivity for 3.6 wt% PEDOT (11.4 wt% PEDOT:PSS) composites increased substantially from 7±2 x 10^{-3} S cm^{-1} to 155±14 S cm^{-1}. Fitting the DMSO treated Nafion-PEDOT:PSS composites to a curve using percolation theory produces the relationship $\sigma_L \propto (p - 0.00156)^{0.918}$, where p is the PEDOT wt%.[28] The percolation threshold $p_c = 0.00156$ suggests that a > 0.156 wt% PEDOT concentration is needed to conduct laterally via a percolated network of conductive PEDOT domains within the Nafion-PEDOT:PSS composite. The critical exponent $t = 0.918$ deviates from the expected value of $t = 2$, which could be due to contributions from tunneling or from the complex morphology of the PEDOT domains.[29] In the application of using the composite to electrically connect two microstructure arrays for a PEC device, lateral conductivity is a relevant parameter if the two microstructure arrays do not vertically align. A 0.3 wt% PEDOT composite with a measured lateral conductivity of 1.4 S cm^{-1} would correspond to a negligible voltage drop

of ~ 7 µV despite having a PEDOT concentration close to the percolation threshold. This estimate assumes a 10 mA cm^{-2} current density with charge carriers conducting up to 10 µm laterally, a reasonable upper-bound given that microwire pitch rarely exceeds this distance.[6, 10]

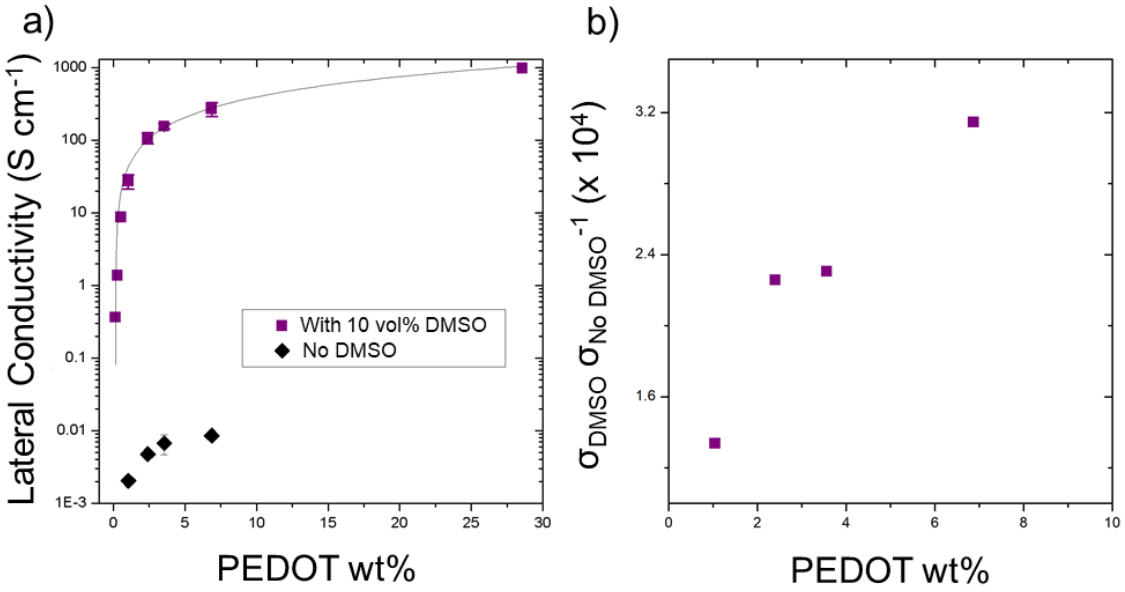

Figure 4.4. (a) Lateral conductivity, σ_L, of Nafion-PEDOT:PSS composites with (purple) and without (black) 10 vol% DMSO (purple) added before polymer curing. DMSO treated composites were fitted to a curve using percolation theory. The x-axis represents PEDOT wt% without PSS wt%; 28.6 wt% PEDOT represents a PEDOT:PSS film without Nafion. The PEDOT to PSS ratio was fixed at 1:2.5 by weight for all samples. (b) Ratio of lateral conductivities of composites with and without DMSO treatment.

Since Nafion-based membrane composites operate in acidic electrolyte during PEC water splitting, the subsequent solution uptake and polymer swelling could affect the electrical conductivity of the membrane film. Fig. 4.5 shows this effect of polymer swelling on the lateral conductivity of the membrane composites. 1.0 M H_2SO_4(aq) was introduced onto the cured membrane surface and the membrane was allowed to visibly swell for 10 min before removing excess electrolyte and taking the conductivity measurement. The

lateral conductivity of the swelled Nafion-PEDOT:PSS composites with 3.5 - 20.5 wt% PEDOT:PSS were ~ 40 - 60% lower than that of the initially cured membrane with no apparent correlation with the PEDOT:PSS wt%. The membranes were subsequently dried in a 75 ˚C oven for 10 min and the resulting lateral conductivity measured was partially restored to ~ 80 % of the initially cured membrane conductivity. For comparison, 100 wt% PEDOT:PSS films exhibited a 15% decrease in conductivity after swelling and was mostly unchanged after drying. These results suggest that Nafion, rather than PSS, predominantly uptakes the H_2SO_4 solution within the composite. The decreased lateral conductivity after swelling is likely due to the swelled Nafion increasing the distance between some conductive PEDOT domains, however the overall extent of percolation appeared mostly intact because the lateral conductivity did not exponentially decrease with lower PEDOT:PSS wt%. Despite the overall decrease in lateral conductivity due to swelling, the order of magnitude of the conductivity is preserved and therefore is sufficient for applications in PEC devices.

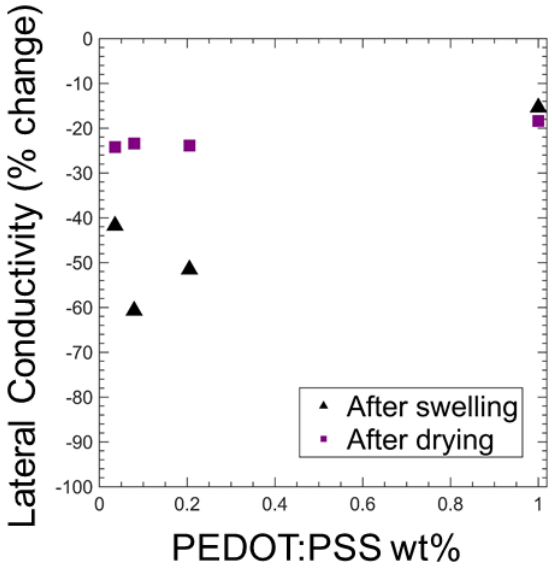

Figure 4.5. The % change of lateral conductivity after swelling Nafion-PEDOT:PSS with 1.0 M H_2SO_4(aq) (black) and after subsequent drying (purple). Both sets of values were calculated relative to the initial lateral conductivity as deposited.

PeakForce tunneling atomic force microscopy (PF-TUNA) was used to examine the influence of DMSO treatment on the morphology of conductive PEDOT domains and additionally was used to estimate the transverse, through-plane conductivity (σ_T) of composite films. A Pt/Ir-coated tip with 16 nN of force and 0.5 V of potential was applied to all samples to ensure consistency between samples. Fig. 4.6 compares the height and current maps taken concurrently at the same area, showing that current was not directly correlated with topography.

Fig. 4.7a shows that the current distribution found in a 11.4 PEDOT:PSS wt% composite without DMSO treatment was localized in circular, μm-scale clusters, suggesting that the electrically conductive, hydrophobic PEDOT phase separated from the insulating hydrophilic Nafion and PSS phases. Fig. 4.7b shows that DMSO treatment prior to film curing leads to a uniform distribution of nm-scale PEDOT domains and an overall increase in current collected. Similar to the effects of polar solvents on PEDOT:PSS films,[19, 30] one explanation for the observed changes in morphology of the Nafion-PEDOT:PSS composites is that DMSO screens Coulomb interactions between PEDOT and the sulfonate groups found in Nafion and PSS. Fig. 4.7c shows that a DMSO-treated, 3.5 wt% film has a sparse distribution of nm-scale PEDOT domains when compared to Fig. 4.7b, suggesting that PEDOT remains homogeneously dispersed in the composite and that the extent of percolation decreased at lower concentrations.

The current at each pixel of the current maps were organized into a histogram (Fig. 4.7d), showing that DMSO treated samples had distributions over a wider range of current than the sample without DMSO treatment. For the 11.4 wt% film without DMSO, 99% of the total current measured was below 43 nA, while 99% of the current for 11.4 and 3.5

wt% DMSO-treated films were below 528 and 67 nA, respectively (Fig. 4.7e). Despite the 3.5 wt% DMSO-treated film having a wider range of current compared to the 11.4 wt% film without DMSO, the latter exhibits an overall higher transverse conductivity due to current distributed across more pixels on the current map. Fig. 4.7f shows that the transverse conductivity estimated over the area of the current maps were 0.2, 1.2±0.6, and 0.03±0.02 S cm^{-1} for 11.4 wt% (no DMSO), 11.4 wt% (DMSO-treated), and 3.5 wt% (DMSO-treated) films, respectively. The estimated transverse conductivity may not accurately reflect the true σ_T of the films due to convolution of contact resistance between the tip and film, which suggests that the obtained numbers could be underestimates. Furthermore, conductivity could be further underestimated due to the current sensitivity set to 100 nA V^{-1}, consequently limiting the maximum current measured at a pixel to ~ 500-600 nA. The lower bound estimate of σ_T for a DMSO-treated 3.5 wt% film nonetheless would result in a negligible voltage drop of ~ 40 µV through a 1 µm thick film at 10 mA cm^{-2}. Resistance drops associated with the bulk ion and electron transport in Nafion-PEDOT:PSS composites therefore are overall negligibly small for current densities relevant to PEC water splitting, even when using a thick (≥ 1 µm) film with dilute (~ 1 wt%) PEDOT content.

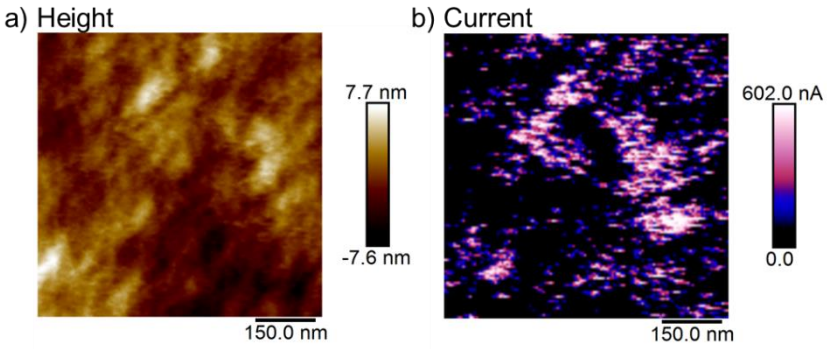

Figure 4.6. (a) Height and (b) current map taken concurrently on the same 700 x 700 nm area of a Nafion-PEDOT:PSS composite with 11.4 wt% PEDOT:PSS and 10 vol% DMSO treatment.

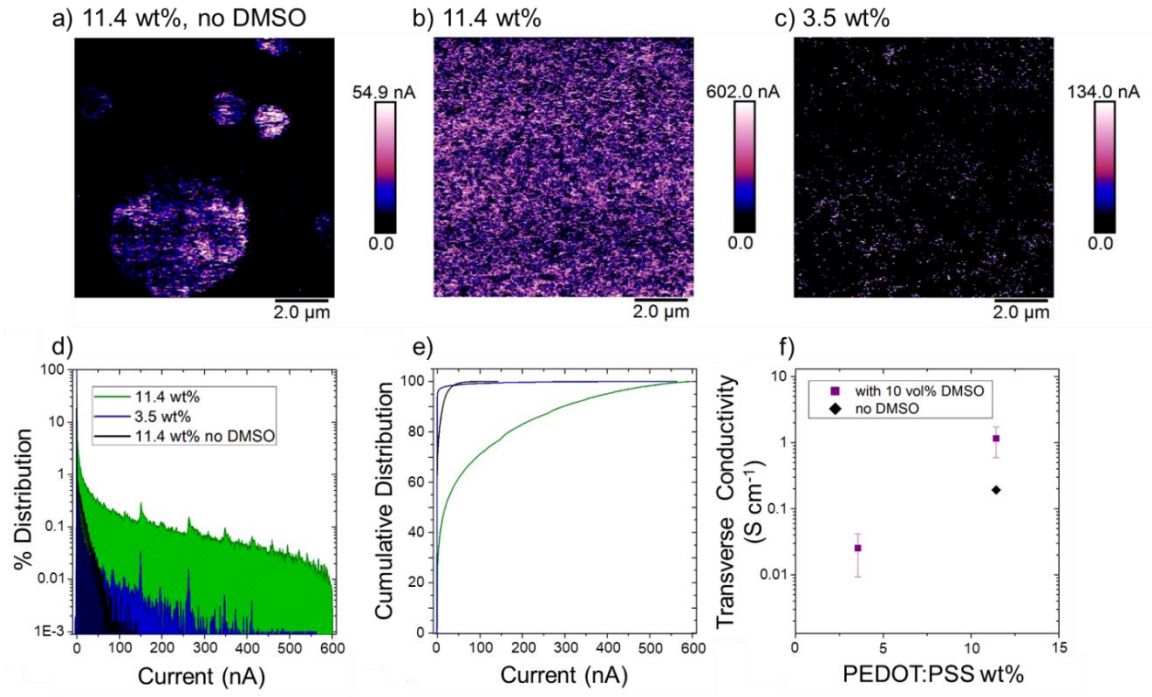

Figure 4.7. Morphology and transverse conductivity of Nafion-PEDOT:PSS composites obtained using PeakForce TUNA. Current maps of Nafion-PEDOT:PSS composites with PEDOT:PSS concentrations of (a) 11.4 wt% with no DMSO treatment, (b) 11.4 wt% with 10 vol% DMSO added, and (c) 3.5 wt% with 10 vol% DMSO added. (d) Distribution and (e) cumulative distribution of currents corresponding to the data in (a-c) for PEDOT:PSS concentrations of 11.4 wt% (green), 3.5 wt% (blue), and 11.4 wt% with no DMSO treatment (black). (f) Estimated transverse conductivity of composites with (purple) and without (black) 10 vol% DMSO treatment.

4.3.5 Surface and Adhesion Properties of Nafion-PEDOT:PSS Composite Films

X-ray photoelectron spectroscopy (XPS) was used to analyze the surface composition of DMSO-treated, Nafion-PEDOT:PSS and PEDOT:PSS films. Fig. 4.8 shows the presence of carbon in the CF_2 configuration at ~ 291 eV binding energy for the as deposited 11.4 wt% and 95 wt% PEDOT:PSS composites.[31] Since PEDOT:PSS films do not contain fluorine atoms, the CF_2 is associated with the fluorinated backbone of Nafion. After removing the film surface layer via sputtering, the underlying surface for the 11.4 wt% film saw a decrease in the CF_2 peak relative to the C-C peak at ~ 285 eV,

indicating that Nafion was enriched at the surface. The CF_2 peak in the 95 wt% film after sputtering could not be resolved, suggesting that Nafion vertically phase separates within the composite at low Nafion concentrations. As expected, no CF_2 peak was detected before or after sputtering the 100 wt% PEDOT:PSS film. Comparing the ratio of C 1s and F 1s peaks (Fig. 4.8d) leads to a similar conclusion of Nafion surface enrichment, although the exact F/C atomic ratio may be convoluted with surface contaminants or surface roughness.[32]

Fig. 4.9 shows a possible consequence of an electrically insulating Nafion surface layer at a nanoscale electrical interface using DataCube PFTUNA. The AFM tip was held for 200 ms at each pixel of the scanned area on a 11.4 wt% composite. A potential sweep from -500 mV to 500 mV was applied linearly throughout this hold segment and current was measured throughout each hold segment for every pixel to produce a three-dimensional current map. The map corresponding to 108 ms (40 mV applied voltage) shows that few pixels passed appreciable current when compared to that of the 180 ms (400 mV applied voltage) map. Current-voltage characteristics at each pixel show that only some pixels showed linear behavior while others produced non-ohmic or noisy behavior. One possible explanation is that despite the AFM tip applying 16 nN of force (~ 8 x 10^3 kPa) on the sample surface, intimate contact between the tip and conductive PEDOT domains was likely not achieved at every pixel. Consequently, the observed nanoscale behavior is conducive towards macroscopic contact resistance. The electrically insulating Nafion surface therefore can impede interfacial charge transfer and subsequently interfacial engineering of the semiconductor/composite interface may be required to avoid potential bottlenecks in device performance.

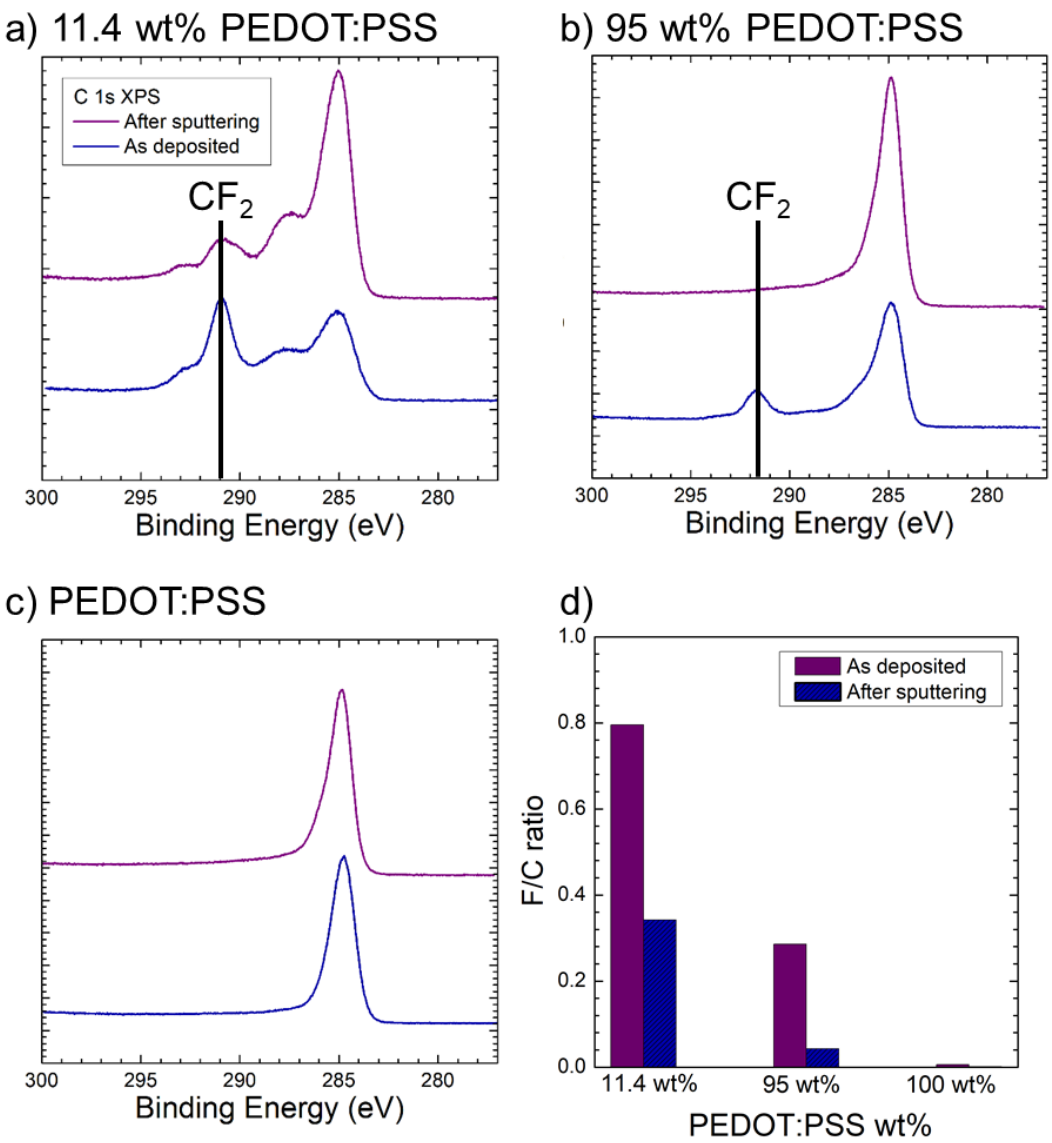

Figure 4.8. XPS data in the C 1s region for Nafion-PEDOT:PSS composites with (a) 11.4 wt%, (b) 95 wt%, and 100 wt% (no Nafion) PEDOT:PSS concentrations as deposited (blue) and after sputtering (blue). The y-axes are in arbitrary units. (d) Approximate F to C atomic ratio found by comparing peak areas of C 1s and F 1s data and dividing by the relative sensitivity factor of 4.34 for as deposited (purple) and after sputtering (blue) films.

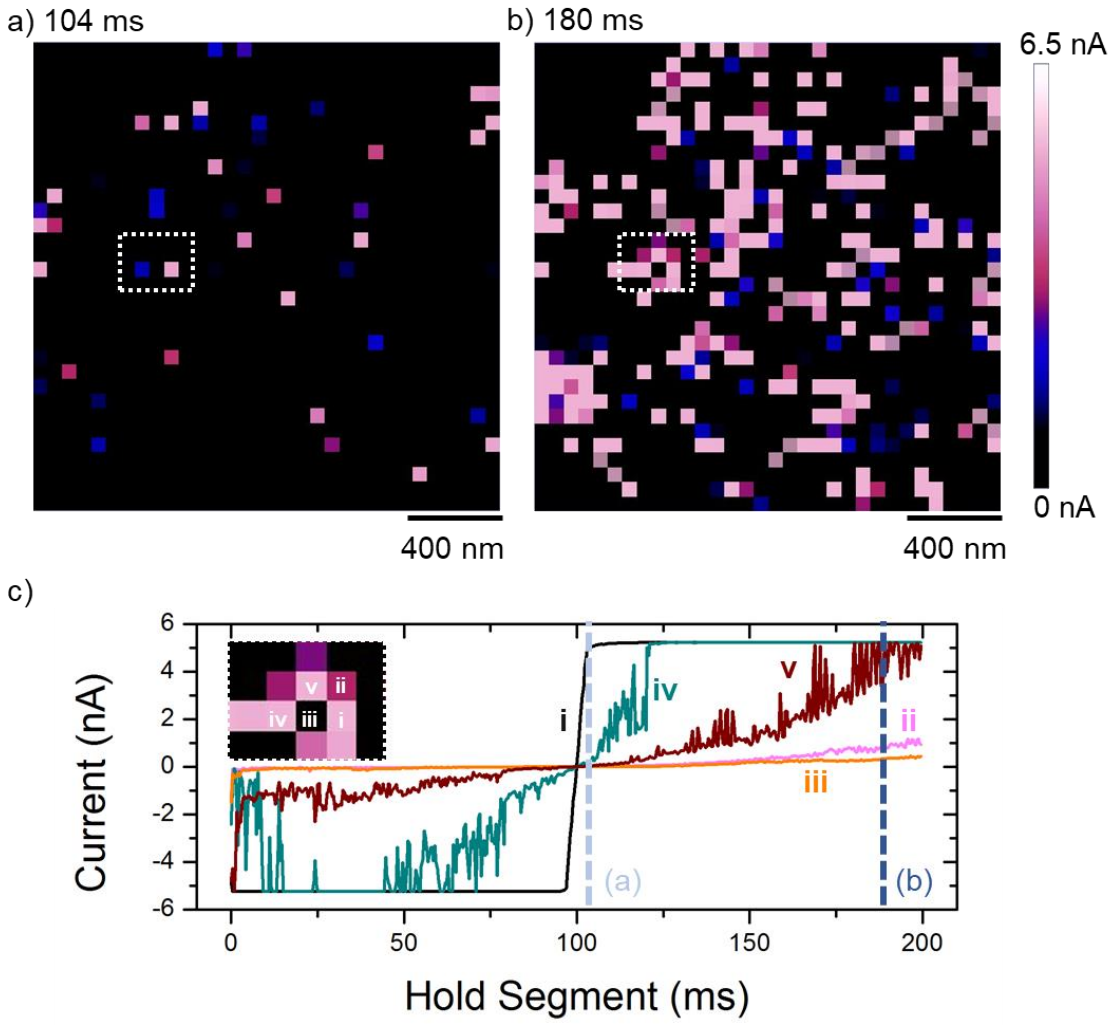

Figure 4.9. Nanoscale electrical behavior of Nafion-PEDOT:PSS films with 11.4 wt% PEDOT:PSS using DataCube PF-TUNA. (a-b) Current maps at (a) 104 ms and (b) 180 ms of the hold segment, which corresponds to the time the AFM tip is held on the film surface. A linear potential sweep from -500 mV to 500 mV was applied throughout the duration of a 200 ms hold segment and each pixel corresponds to the current collected at the given time on the hold segment. (c) Current-voltage characteristics for associated with five pixels as labeled within the inset. The applied voltage was -500, 0, and 500 mV at 0, 100, and 200 ms of the hold segment. The current sensitivity was held at 1 nA V^{-1} and subsequently the current was saturated at 5 nA.

Fig. 4.10 demonstrates the ability of Nafion-PEDOT:PSS composites to adhere to Nafion 115 membranes. DMSO-treated, composite films with 11.4 wt% PEDOT:PSS were drop cast onto a borosilicate glass slide and both the composite and Nafion 115 were then swelled with water. The two films were laminated together by clamping the two films

between glass slides and heating in a 75 ˚C oven to dry the films. The procedure was repeated with a DMSO-treated PEDOT:PSS film laminated onto Nafion 115 as a control. The samples were removed from the glass slide and sonicated in 1.0 M H_2SO_4(aq) for 11 min. The PEDOT:PSS control appeared to delaminate from Nafion 115 entirely; the film instead became partially dispersed in the solution while macroscopic flakes settled at the bottom of the solution. In contrast, the Nafion-PEDOT:PSS remained laminated on the film without any visual indication that the film was partially dispersed in solution. Delamination of the PEDOT:PSS control occurred likely because PEDOT:PSS and Nafion have different swelling characteristics in solution.[21, 22] Additionally, H_2SO_4 screens the interactions between PEDOT and PSS, allowing for excess PSS to wash away and the PEDOT to separate when sonication was introduced.[33] This mechanical instability was not observed in the Nafion-PEDOT:PSS films because the relatively dilute PEDOT (~ 3.6 wt%) was held closely by the Nafion bulk that likely did not wash away in H_2SO_4. Furthermore, the composite remained adhered to Nafion 115 because the Nafion-rich surface layer on the composite helped preserve lamination. In principle, the Nafion-PEDOT:PSS composite should be more mechanically compatible than PEDOT:PSS as an adhesion layer to a Nafion-embedded wire array given that such a PEC device operates in acidic electrolyte. Furthermore, strain introduced by a mechanically flexible form factor may also promote the delamination of PEDOT:PSS in solution.

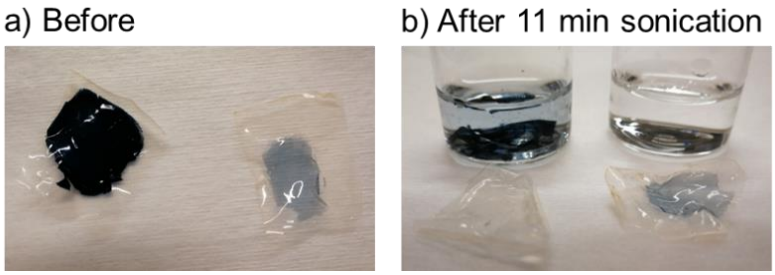

Figure 4.10. Optical images (a) before and (b) after sonication for 11 min in 1.0 M H_2SO_4(aq) for PEDOT:PSS (left) and Nafion-PEDOT:PSS with 11.4 wt% PEDOT:PSS (right) each laminated onto Nafion 115. In (b), the solutions that the films were sonicated in are shown above their respective films.

4.3.6 Interfacial Characteristics of Si/Nafion-PEDOT:PSS

The work function of the composite determines ohmic or rectifying behavior when contacting the film with a semiconductor. Fig. 4.11 shows the work function of the composites and PEDOT:PSS before and after surface sputtering using ultraviolet photoelectron spectroscopy (UPS). The work function decreased after sputtering for each sample, with the 11.4 PEDOT:PSS wt% film decreasing from 5.79±0.02 to 5.27±0.07 eV and the 100 wt% PEDOT:PSS film decreasing from 5.03±0.01 to 4.76±0.02 eV. Consistent with other reports,[34, 35] the excess Nafion or PSS on the surface contributes to an increased work function and subsequently promotes ohmic contact with p-type semiconductors like Si due to favorable energetics for hole injection. Conversely, contact with n-type Si produces a rectifying contact (Fig. 4.12). Mott-Schottky analysis showed that 3.5 wt%, 11.4 wt%, and 100 wt% films produced similar barrier heights of 0.96 V, 0.96 V, and 0.98 V, respectively. Rectifying curves were demonstrated by sweeping the voltage from -1.0 V to 1.0 V and measuring the current density for each film. Lower PEDOT:PSS concentrations corresponded to more resistance, with 3.5 wt%, 11.4 wt%, and 100 wt%

films producing -19 mA cm^{-2}, -38 mA cm^{-2}, and -53 mA cm^{-2} of current density at an applied voltage of -1.0 V.

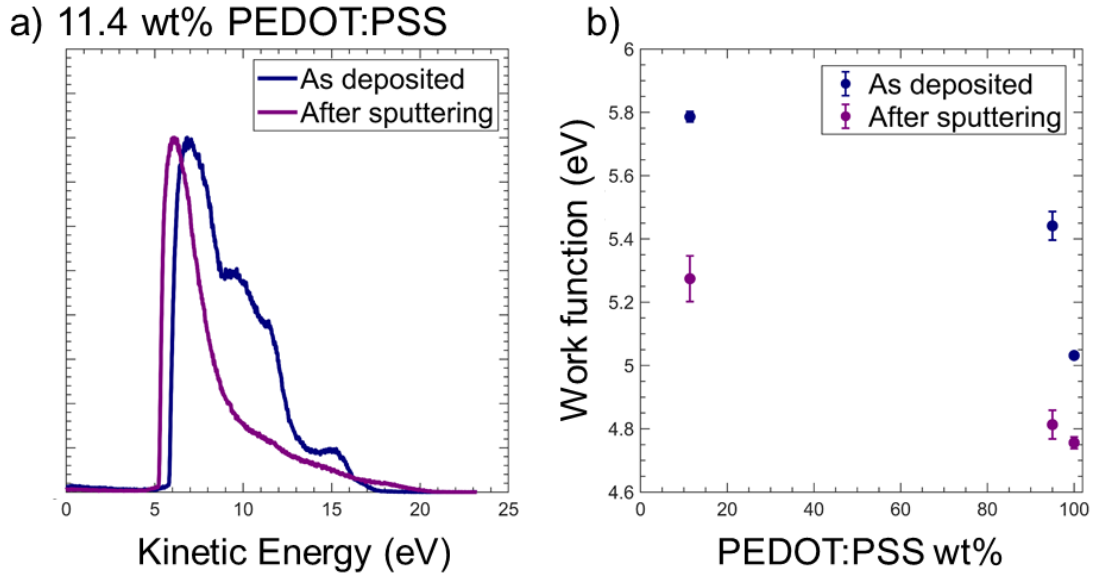

Figure 4.11. (a) Representative UPS data for Nafion-PEDOT:PSS composite with 11.4 wt% PEDOT:PSS as deposited (blue) and after sputtering (purple). The y-axis is in arbitrary units. (b) Work function of composite films and PEDOT:PSS.

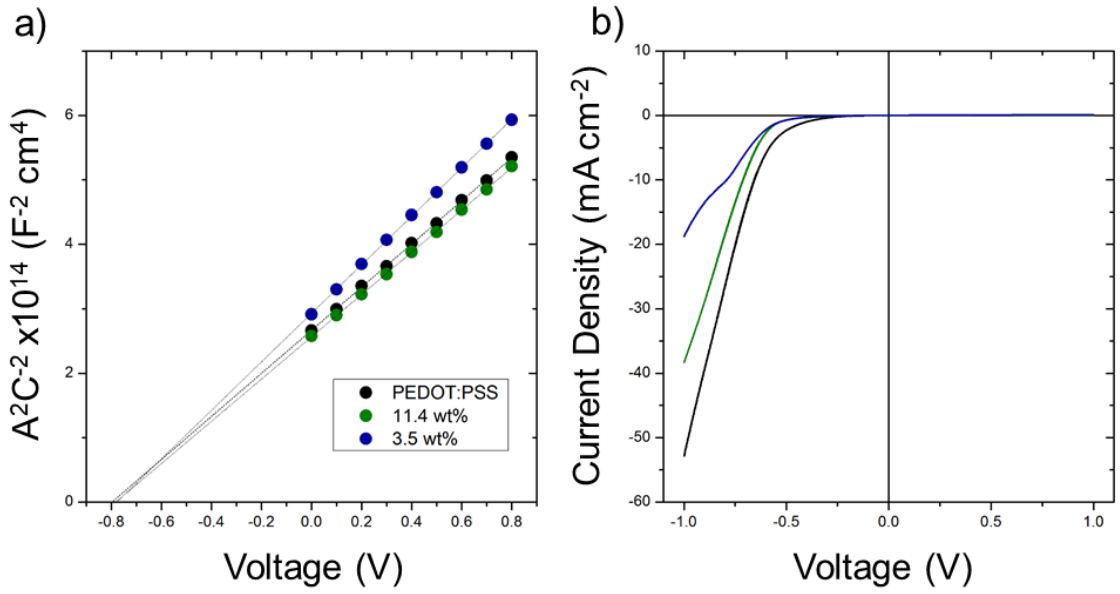

Figure 4.12. (a) Mott-Schottky plot and (b) current-voltage characteristics of Nafion-PEDOT:PSS films with 100 wt% (black), 11.4 wt% (green), and 3.5 wt% (blue) PEDOT:PSS concentration in contact with n-Si. Samples were measured in air using a Hg top contact.

Fig. 4.13 shows the current-voltage characteristics of p-Si contacted with 11.4 PEDOT:PSS wt% composites. Prior to contacting the composite, a p-Si sample was submerged in buffered oxide etch (BOE) in order to remove its native oxide and produce a H-terminated surface. The resulting contact with the composite film produced a non-linear, resistive contact that can be attributed to Si making contact with an insulating Nafion surface layer and to the subsequent oxidation of the Si surface when in contact with acidic sulfonate groups. The combined insulator thickness of Nafion and SiO_x lead to a lower tunneling probability and subsequently could contribute to the estimated ~ 9.3 Ω-cm^2 contact resistance.[36] A previous report showed that CH_3-termination of the Si surface can suppress SiO_x formation and lower the contact resistance between p-Si and PEDOT:PSS films.[37] Contacting the composite with and without DMSO treatment to CH_3-terminated p-Si produced ohmic contacts with 1.3 Ω-cm^2 and 7.6 Ω-cm^2 contact resistances, respectively. This observed magnitude of enhancement with DMSO treatment was consistent with the enhancement found at the microscale with PF-TUNA (Fig. 4.7). For comparison, the CH_3-terminated p-Si/PEDOT:PSS electrode had a 0.8 Ω-cm^2 contact, indicating that the Nafion layer of the DMSO treated composite sample increased contact resistance by only 0.5 Ω-cm^2 assuming negligible bulk resistance drops. Without the added thickness of a SiO_x layer, the Nafion surface layer of the composite was therefore thin enough to tunnel without significant losses.

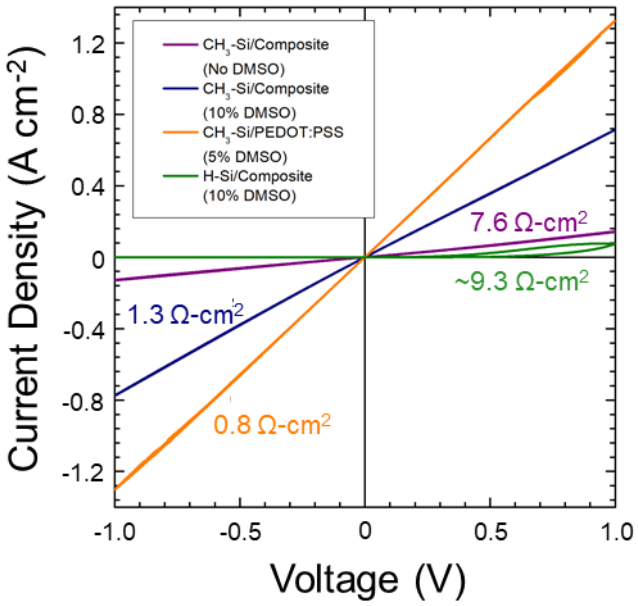

Figure 4.13. Current-voltage characteristics and estimated contact resistances of the following p-Si(111)/polymer electrodes: CH_3-terminated p-Si in contact with a 11.4 PEDOT:PSS wt% composite without (purple) and with (blue) DMSO treatment, CH_3-terminated p-Si in contact with PEDOT:PSS with DMSO treatment (yellow), and H-terminated p-Si in contact with 11.4 wt% composite with DMSO treatment (green). Samples were measured in air using a Hg top contact.

In addition to CH_3-termination on the Si surface to reduce contact resistance incurred by the Nafion-rich layer, potential strategies exist to further lower the interfacial resistance via modification of the composite itself. For instance, deposition of nanostructured conductive materials on either the Nafion-PEDOT:PSS surface or dispersed in the composite bulk could in principle lower contact resistance to p-Si. High aspect ratio Ag nanowires are a potential candidate and have been shown to be dispersed with PEDOT:PSS.[38] For a Nafion-PEDOT:PSS-Ag nanowire composite, the embedded Ag nanowires in principle should not vertically phase separate from Nafion at the surface due to the Ag being a high aspect ratio transition metal. Further work is required to investigate the effects such metal nanowires or others on composite adhesion, parasitic absorption, and chemical stability in acidic electrolyte.

4.3.7 Outlook for Nafion-PEDOT:PSS Integration in Tandem Devices

Although an electrically conductive composite membrane has been shown to be a viable candidate for an integrated PEC device in acidic electrolytes, to date there has not been a demonstration of an equivalently functioning membrane for direct use in alkaline electrolytes.[8, 15] In order to leverage the advantages associated with operation at high pH, such as the availability of stable and active earth-abundant catalysts, the electrically conductive interlayer used should possess positively charged functional groups to facilitate OH^- conduction. Using PEDOT as the electrically conductive component could be challenging because it relies on negatively charged polymers like PSS to act as the dopant and dispersant. Investigation of the morphology and subsequent effect on bulk conductivity upon pairing an anion exchange ionomer with an electrically conductive component like PEDOT is therefore required. Alternatively, a PEDOT-based composites can be laminated between a cation and anion exchange membrane, producing a bipolar membrane operating in both acidic and alkaline electrolytes.[39] For instance, a composite consisting of graphene oxide, PEDOT, and phosphomolybdic acid (PMA) was shown to maintain electrical conductivity while exhibiting low overpotentials for water dissociation due to the graphene oxide in the film.[40]

The Nafion-PEDOT:PSS composite serves to form an ohmic contact with p-type semiconductors due to its high work function (Fig. 4.11), however a low resistance contact must also be made to n-type semiconductors. Thiophene functionalization of n-Si microwires was previously shown to lower the contact resistance and exhibit ohmic behavior to PEDOT:PSS when compared to CH_3-terminated n-Si.[41] Both CH_3- and thiophene-terminated surfaces have been demonstrated on individual Si microwires,[42] and

to date have not been shown on the backsides of Nafion-embedded wire arrays. The contact resistance of such surfaces to Nafion-PEDOT:PSS and their associated stability in acidic electrolyte must also be elucidated for the efforts toward a fully integrated PEC assembly.

4.4 Conclusions

One proposed integrated solar water splitting device involves two ion-exchange membrane-embedded, semiconducting micro- or nanowire arrays electrically connected in series as a tandem. This electrically conductive interlayer must be optically transparent, ion permeable, and adhere to each membrane-embedded array. A composite Nafion-PEDOT:PSS film possesses excellent adhesion and charge transport properties while being more transparent than PEDOT:PSS alone. Understanding the phase-separation behavior between conductive (PEDOT) and non-conductive (Nafion/PSS) domains elucidates structure-property relationships of the Nafion-PEDOT:PSS film. A percolated network of conductive PEDOT domains held by a Nafion/PSS bulk enables electron conduction while maintaining the mechanical stability and proton conducting properties of Nafion. The addition of DMSO reduces these domain sizes from μm- to nm-scale, leading to an estimated percolation threshold of ~ 0.5 wt% PEDOT:PSS and subsequently producing a $>10^4$ fold increase in lateral conductivity. The presence of an insulating, Nafion-rich surface layer on the composite introduces additional interfacial resistance when in contact with p-Si. CH_3-termination on the Si surface mitigates this concern by suppressing native oxide formation and subsequently forms a low resistance contact to Nafion-PEDOT:PSS composites.

4.5 References

1. N. S. Lewis, *Science*, 2016, **351**, aad1920.
2. S. Haussener, C. Xiang, J. M. Spurgeon, S. Ardo, N. S. Lewis and A. Z. Weber, *Energy & Environmental Science*, 2012, **5**, 9922-9935.
3. S. Hu, C. Xiang, S. Haussener, A. D. Berger and N. S. Lewis, *Energy & Environmental Science*, 2013, **6**, 2984-2993.
4. E. Verlage, S. Hu, R. Liu, R. J. R. Jones, K. Sun, C. Xiang, N. S. Lewis and H. A. Atwater, *Energy & Environmental Science*, 2015, **8**, 3166-3172.
5. W.-H. Cheng, M. H. Richter, M. M. May, J. Ohlmann, D. Lackner, F. Dimroth, T. Hannappel, H. A. Atwater and H.-J. Lewerenz, *ACS Energy Letters*, 2018, **3**, 1795-1800.
6. E. L. Warren, H. A. Atwater and N. S. Lewis, *The Journal of Physical Chemistry C*, 2013, **118**, 747-759.
7. J. M. Spurgeon, S. W. Boettcher, M. D. Kelzenberg, B. S. Brunschwig, H. A. Atwater and N. S. Lewis, *Adv Mater*, 2010, **22**, 3277-3281.
8. J. M. Spurgeon, M. G. Walter, J. Zhou, P. A. Kohl and N. S. Lewis, *Energy & Environmental Science*, 2011, **4**, 1772-1780.
9. S. Ardo, S. H. Park, E. L. Warren and N. S. Lewis, *Energy & Environmental Science*, 2015, **8**, 1484-1492.
10. P. A. Kempler, M. A. Gonzalez, K. M. Papadantonakis and N. S. Lewis, *ACS Energy Letters*, 2018, **3**, 612-617.
11. M. R. Shaner, J. R. McKone, H. B. Gray and N. S. Lewis, *Energy & Environmental Science*, 2015, **8**, 2977-2984.
12. M. R. Shaner, S. Hu, K. Sun and N. S. Lewis, *Energy & Environmental Science*, 2015, **8**, 203-207.
13. X. Shen, M. Yao, K. Sun, T. Zhao, Y. He, C.-Y. Chi, C. Zhou, P. D. Dapkus, N. S. Lewis and S. Hu, *ACS Energy Letters*, 2021, **6**, 193-200.
14. K. M. Kennedy, P. A. Kempler, M. Cabán-Acevedo, K. M. Papadantonakis and N. S. Lewis, *Nano Letters*, 2021, **21**, 1056-1061.
15. S. Chabi, K. M. Papadantonakis, N. S. Lewis and M. S. Freund, *Energy & Environmental Science*, 2017, **10**, 1320-1338.
16. K. Sun, S. Zhang, P. Li, Y. Xia, X. Zhang, D. Du, F. H. Isikgor and J. Ouyang, *Journal of Materials Science: Materials in Electronics*, 2015, **26**, 4438-4462.
17. I. Yahyaie, K. McEleney, M. G. Walter, D. R. Oliver, D. J. Thomson, M. S. Freund and N. S. Lewis, *The Journal of Physical Chemistry C*, 2011, **115**, 24945-24950.
18. J. P. Bruce, S. Asgari, S. Ardo, N. S. Lewis, D. R. Oliver and M. S. Freund, *The Journal of Physical Chemistry C*, 2014, **118**, 27742-27748.
19. H. Shi, C. Liu, Q. Jiang and J. Xu, *Advanced Electronic Materials*, 2015, **1**, 1500017.
20. I. Zozoulenko, A. Singh, S. K. Singh, V. Gueskine, X. Crispin and M. Berggren, *ACS Applied Polymer Materials*, 2019, **1**, 83-94.
21. M. Modarresi, A. Mehandzhiyski, M. Fahlman, K. Tybrandt and I. Zozoulenko, *Macromolecules*, 2020, **53**, 6267-6278.
22. W. P. Kalisvaart, H. Fritzsche and W. Mérida, *Langmuir*, 2015, **31**, 5416-5422.

23. S. L. McFarlane, B. A. Day, K. McEleney, M. S. Freund and N. S. Lewis, *Energy & Environmental Science*, 2011, **4**.
24. H.-Y. Jung and J. W. Kim, *International Journal of Hydrogen Energy*, 2012, **37**, 12580-12585.
25. M. Cabán-Acevedo, K. M. Papadantonakis, B. S. Brunschwig and N. S. Lewis, *The Journal of Physical Chemistry C*, 2020, **124**, 16338-16349.
26. S. Slade, S. A. Campbell, T. R. Ralph and F. C. Walsh, *Journal of The Electrochemical Society*, 2002, **149**, A1556.
27. L. Liu, W. Chen and Y. Li, *Journal of Membrane Science*, 2016, **504**, 1-9.
28. M. Loos, in *Carbon Nanotube Reinforced Composites*, ed. M. Loos, William Andrew Publishing, Oxford, 2015, DOI: https://doi.org/10.1016/B978-1-4557-3195-4.00005-9, pp. 125-170.
29. R. M. Mutiso and K. Winey, *Polymer Science: A Comprehensive Reference, 10 Volume Set*, 2012, **7**, 327-344.
30. J. Y. Kim, J. H. Jung, D. E. Lee and J. Joo, *Synthetic Metals*, 2002, **126**, 311-316.
31. C. Chen, G. Levitin, D. W. Hess and T. F. Fuller, *Journal of Power Sources*, 2007, **169**, 288-295.
32. A. M. Ferraria, J. D. Lopes da Silva and A. M. Botelho do Rego, *Polymer*, 2003, **44**, 7241-7249.
33. D. Xu, H. Shen, W. Wang, J. Xie, T. Zhang, H. Yuan, Y. Li, X. Chen, Y. He and Y. Zhang, *ChemPhysChem*, 2019, **20**, 374-382.
34. H. J. Snaith, H. Kenrick, M. Chiesa and R. H. Friend, *Polymer*, 2005, **46**, 2573-2578.
35. S. H. Kim, J. Kim, S. Nam, H. S. Lee, S. W. Lee and J. Jang, *ACS Appl Mater Interfaces*, 2017, **9**, 12637-12646.
36. L. B. Freeman and W. E. Dahlke, *Solid-State Electronics*, 1970, **13**, 1483-1503.
37. M. G. Walter, X. Liu, L. E. O'Leary, B. S. Brunschwig and N. S. Lewis, *The Journal of Physical Chemistry C*, 2013, **117**, 14485-14492.
38. S. Kim, S. Y. Kim, J. Kim and J. H. Kim, *Journal of Materials Chemistry C*, 2014, **2**, 5636-5643.
39. S. Chabi, A. G. Wright, S. Holdcroft and M. S. Freund, *ACS Appl Mater Interfaces*, 2017, **9**, 26749-26755.
40. M. B. McDonald, M. S. Freund and P. T. Hammond, *ChemSusChem*, 2017, **10**, 4599-4609.
41. J. P. Bruce, D. R. Oliver, N. S. Lewis and M. S. Freund, *ACS Applied Materials & Interfaces*, 2015, **7**, 27160-27166.
42. I. Yahyaie, S. Ardo, D. R. Oliver, D. J. Thomson, M. S. Freund and N. S. Lewis, *Energy & Environmental Science*, 2012, **5**.